# Characterization of secondary mantle convection from geophysical data and models

by

Bimal Pandit

B.S., Tri-Chandra Multiple Campus, Tribhuvan University, 2017

A THESIS

submitted in partial fulfillment of the requirements for the degree

MASTER OF SCIENCE

Department of Geology
College of Arts and Sciences

KANSAS STATE UNIVERSITY
Manhattan, Kansas

2020

Approved by:

Major Professor
Dr. Claudia Adam

# Abstract

Small-scale convection or secondary convection has been studied using the geophysical data and models such as seismic tomography models and geoid anomalies. We used three seismic tomography models, SEMUCB-WM1, SAVANI and S40RTS to infer the lithosphere/asthenosphere boundary, and the destabilization of the lithosphere, induced by secondary mantle convection. Former studies, based on numerical and experimental models report that secondary convection would occur as sub-lithospheric longitudinal rolls, induced by the shear associated with the lithospheric plate motion, or as helices, formed when sinking cold plumes, falling from the base of the lithosphere are sheared away by the large-scale flow. Our study shows that the secondary convection under the Pacific plate occurs in the form of 3D plumes and helices. The lithospheric drips observed in the tomography models first appear as small wavelength anomalies beneath a 30-40 M.y. old and 75-90 km thick lithosphere. They are observed as longer elongated patterns beneath 105 M.y. old and 138 km thick lithosphere. Most of the lithospheric anomalies are associated with negative geoid anomalies of order and degrees 8-40. No clear correlation between lithospheric destabilization and volcanism is observed.

# Table of Contents

# List of Figures

# List of Tables

# Acknowledgements

First and foremost, I would like to express my sincere gratitude to my advisor Dr. Claudia Adam for her continuous support and guidance throughout my master's study and research. I am more than happy and feel lucky to get her as my advisor. Her immense knowledge, patience and motivations are the key factors for my successful completion of the master's degree.

Also, I would like to extend my sincere gratitude towards my committee members: Dr. Pamela Kempton and Dr. Valérie Vidal for their valuable insights and comments.

Finally, I would like to remember and thank my father, mother and brother for all their continuous supports, encouragements and unconditional love. Also, I would like to give thanks to my relatives and my friends for their generous support all these days.

# Chapter 1 - Introduction

Mantle convection occurs at different scales. Large scale convection occurs at the scale of lithospheric plates. Small scale convection, or secondary convection, occurs at a smaller scale, generally as sub-lithospheric longitudinal rolls or in the form of 3D plumes and helices, induced by the shear associated with the lithospheric plate motion. Most of the heat out of the Earth's mantle is transported by the large scale convection, but secondary convection is required in order to account for the observed heat dissipation near the surface. Secondary convection not only provides the complete picture on heat transfer from the mantle to the surface, but also defines the coupling between mantle and lithosphere. The first insights into secondary convection came from geoid and gravity data in the Pacific and Indian oceans. Since then, there have been several studies trying to assess the phenomenology of small-scale convection, mainly through numerical or experimental studies. However, applying the results of such studies, mainly the experimental ones, to what is actually happening in the Earth's mantle is not straightforward. Geophysical data are the best tool for describing the characteristics/morphology of secondary convection, and therefore helping to constrain the origin and dynamics of this convective pattern. In this study, we use the latest datasets and models, such as seismic tomography models and geoid to provide a more accurate characterization of secondary convection rolls. In the second chapter, we provide background information on the secondary convections. The third chapter describe the data used in this study, and the methods implemented to process these data. The results are presented in chapter four and discussed and interpreted in chapter five.

# Chapter 2 - Background

## 2.1 Structure of the Earth and Plate Tectonic Theory

The surface of the Earth is covered by several tectonic plates that constantly move relatively to one another through a process called “plate tectonics”. The tectonic plates are created at Mid Oceanic Ridges (MOR). They then move away from the MOR and eventually subduct into the mantle along subduction zones. From a geodynamic point of view, the structure of the Earth can be approximated by several concentric layers: the crust, the lithosphere, the asthenosphere, the mantle and the core. The definitions of these layers depend on the properties we are looking at. For example, the asthenosphere will not be the same for a geodynamicist as for a petrologist. In the following, we consider these definitions from the geodynamical point of view. In this context, the main parameters necessary for distinguishing between these layers is their rheology. The crust is the outermost layer of the Earth. It is rigid and very thin compared to other inner layers. The crust’s thickness ranges from about 5-6 km beneath the oceans to several tens of kilometers beneath the continents. The lithosphere is the rigid and relatively cool outer layer of the earth, which moves along the surface of earth via the process called plate tectonics. The thickness of the lithosphere is about 100 km for the oceanic plates, while the thickness of the continental lithosphere varies from 100 to 300 km (Turcotte and Schubert, 2002). Beneath the lithosphere lies a less rigid layer called the asthenosphere, characterized by slower seismic velocities, generally considered as a low viscosity layer in geodynamic models. In contrast to the lithosphere, the asthenosphere is sufficiently weak that it can deform through solid-state creep processes and can flow like a fluid over the period of geologic time (Turcotte and Schubert, 2002). As the coupling between mantle dynamics and plate tectonics occurs in the asthenosphere, this layer plays a major role in plate tectonics. However, the characteristics of the asthenosphere like its thickness, viscosity, and the flow pattern occurring within it are still debated. The mantle, which is divided into two layers (upper mantle and lower mantle), extends to a depth of about 2900km, i.e. to the core-mantle boundary. Overlain by the mantle, at the center of the Earth lies

the core, composed mainly of iron and nickel. The density of the core is about twice that of mantle. The core is made of two distinct layers- (i) the outer liquid core with thickness about 2200km and (ii) the inner solid core with thickness about 1250 km.

Plate tectonics is a consequence of thermal convection occurring in the mantle. It is induced by radiogenic decay and the cooling of the Earth (Turcotte and Schubert, 2002). The decay of isotopes of uranium ($^{235}U$ and $^{238}U$), thorium ($^{232}Th$) and potassium ($^{40}K$) are believed to be the main sources of radiogenic heat production in the mantle and the crust of the Earth (Turcotte and Schubert, 2002). The radioactive decay of these elements accounts for about 80% of the surface heat flow, while the remaining 20% of the surface heat flow comes from the secular cooling of the Earth (Turcotte and Schubert, 2002). This thermally driven convection taking place in the mantle of the Earth is called mantle convection; it accounts for a number of different geodynamic processes.

## 2.2 Thermal Convection in a Fluid

French physicist, Henry Bénard (1901), describes the onset of thermal convection in a fluid layer heated from below. In his laboratory experiments he observed the formation of different patterns of hexagonal convection cells (Figure 1) on the surface of the fluid layer. These cells are also called Bénard Cells.

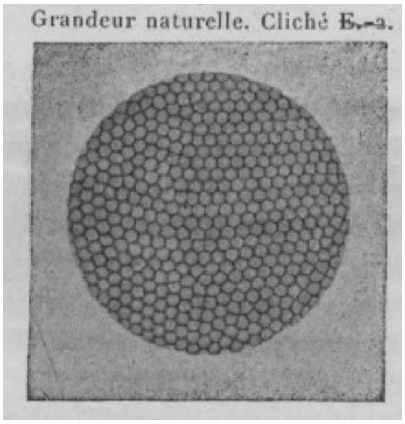


Figure 1: Hexagonal cellular patterns observed by Bénard (1901)

Bénard (1901) observed that the hot fluid rises from the middle of each cell to the surface and then cools by spreading at the surface. Adjoining cells then come in contact with each other at the narrow margins, where the cooled fluid sinks back into the layer. The theory explaining what Bénard (1901) observed in his experiments was derived later by Rayleigh (1916). This type of convection in fluids is also called Rayleigh-Bénard convection.

In order to illustrate the mechanism of Rayleigh-Bénard convection, let's consider Figure 2, where a horizontal fluid layer placed in a gravitational field is heated from below and cooled from above. Under these conditions, a thin thermal boundary layer of cold fluid forms at the top of the horizontal layer. Because the cold fluid near the upper boundary is denser than the hotter fluid below it, the cold fluid sinks as a descending plume (represented by blue down-going arrows) and is replaced by the less dense, hotter fluid rising from beneath (represented by red up-going arrows). The negative buoyancy of the descending plume drives the convection flow in the system (Barletta, 2019). In Figure 2, the upper boundary layer is analogous to the lithosphere, the cool descending plumes are analogous to the lithospheric plate being subducting into the mantle, and the upwellings are analogs of the mantle upwelling occurring along plumes or mid-oceanic ridges.

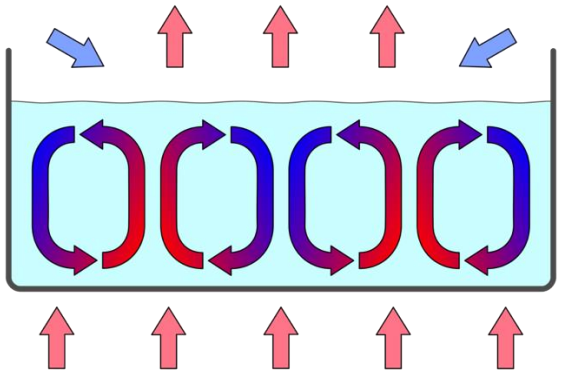

Figure 2 : Illustration of convection cells that develop in a horizontal fluid layer heated from below and cooled from above (https://en.wikipedia.org/wiki/File:ConvectionCell.svg)

The onset of convection in the fluid depends on the value of the Rayleigh number (Ra). Physically, the Rayleigh number corresponds to the ratio between the buoyancy forces, which are inducting

motion, to the diffusive processes (diffusion of heat and viscosity), which tend to slow down the motion and stabilize the fluid. For a horizontal fluid layer heated from the bottom and cooled from above, Ra is described by equation (1).

$$\mathrm{Ra} = \frac{g\beta}{\nu\alpha}\theta x^3 \qquad \text{(equation 1)}$$

Where,

x represents the thickness of the fluid layer (m)

$g$ represents the acceleration due to gravity ($ms^{-2}$)

β represents the thermal expansion coefficient of a fluid ($K^{-1}$)

ν represents the kinematic viscosity ($m^2/s$)

α represents the thermal diffusivity ($m^2/s$)

θ represents the superadiabatic temperature gradients across the fluid layer (K)

The above equation can be solved from linear stability analysis to obtain a minimum value of Ra for any horizontal fluid layer heated from below and cooled from above (as illustrated in Figure 3). The obtained minimum value of Ra is called the critical Rayleigh number, denoted as $\mathrm{Ra}_{cr}$.

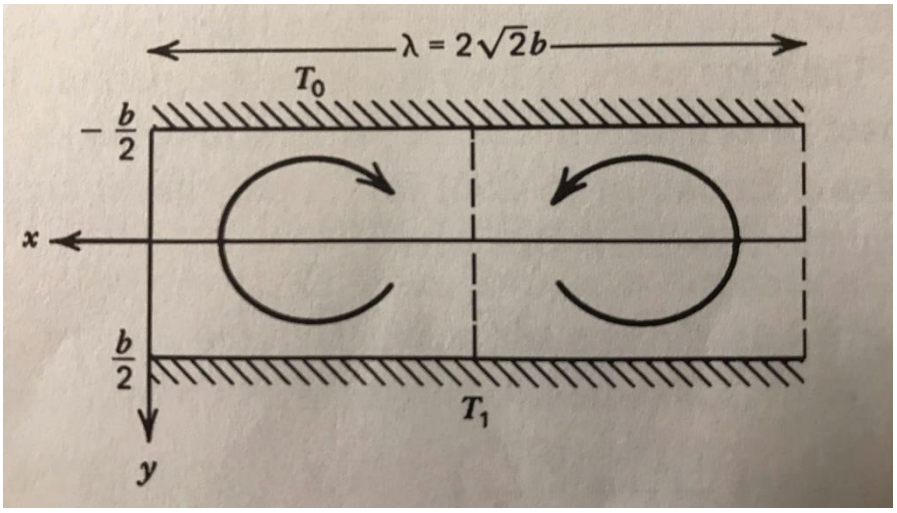


Figure 3 : Illustration of two-dimensional cellular convection in a fluid layer heated from below and cooled from above (Turcotte and Schubert, 2002). In this figure, 'b' represents the thickness of the horizontal fluid layer, 'λ' represents the value of wavelength of disturbance corresponding to the smallest value of the critical Rayleigh number, T1 represents the temperature of the lower boundary, while $T_0$ represents the temperature of upper boundary

The value of the $Ra_{cr}$ of the fluid is dependent upon the properties and the geometry of the convecting fluid, and the other different physical parameters reported in equation (1). Heat will be transferred by conduction if the $Ra < Ra_{cr}$ and by convection for $Ra > Ra_{cr}$.

## 2.3 Whole Mantle Convection vs Layered Mantle Convection

Mantle convection occurs at different scales. At the largest scale, the convection occurs at the scale of the lithospheric plates, as illustrated in Figure 4. In Figure 4, the mantle is upwelling under a mid ocean ridge, where the lithospheric plates are created. Some plates are diving into the mantle along subduction zones. The mantle flow associated with the phenomenon is represented by the red arrows.

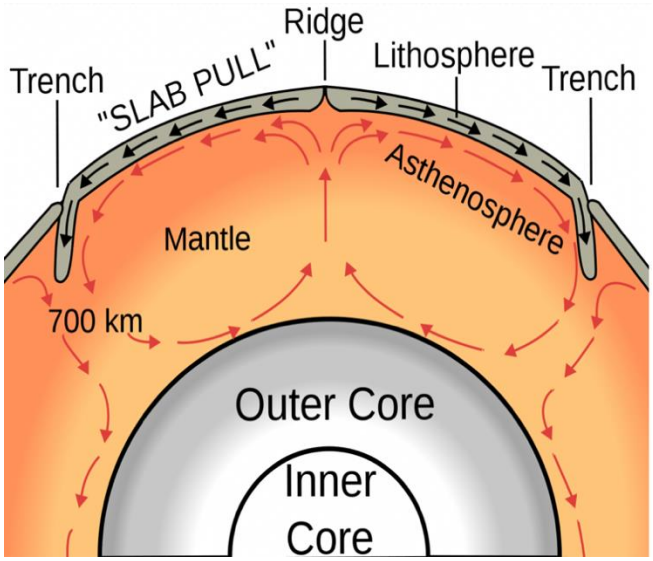


Figure 4 : Illustration of model of large-scale mantle convection occurring at the scale of lithospheric plate(https://upload.wikimedia.org/wikipedia/commons/thumb/2/27/Oceanic_spreading.svg/520px-Oceanic_spreading.svg.png)

Although, it is agreed that the mantle is convecting beneath the lithospheric plate, debate exists regarding whether the mantle convects as a whole (Schubert et al., 2001; Barry et al., 2017) or separately in the upper and lower mantle (Wen and Anderson, 1997; Hofmeister and Criss, 2005). Whole mantle convection would occur across the entire mantle. In this model,

significant amounts of the lithospheric plates get subducted beneath 660 km and is complemented by mantle upwelling under mid-oceanic ridges, as is shown in Figure 4. Recently, Barry et al. (2017) developed 3D spherical numerical models of mantle convection and proposed that convection occurs in cells isolated by subducting slabs but encompassing both upper and lower mantle. Based on the geochemical data, these authors suggest that the geochemical composition of the mantle should have been influenced by whole mantle convection at least since 550 Ma, or potentially since the start of plate tectonics itself. On the other hand, several authors have argued against this whole mantle convection model from geodynamical models (Wen and Anderson, 1997). In contrast to whole mantle convection, they propose a layered mantle convection model. In this model, the upper convective system associated with plate tectonics is restricted to the upper 660 km of the mantle (Figure 5) and another separate convective system occurs from 660 km up to the core-mantle boundary.

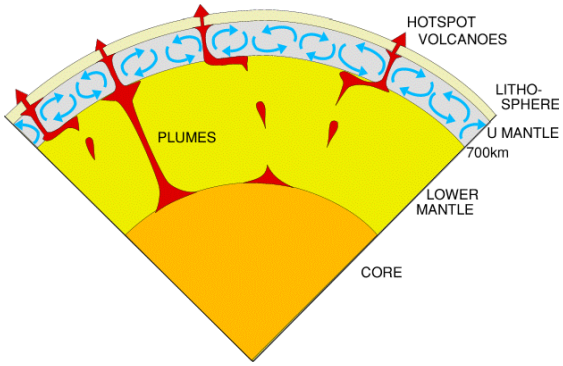


Figure 5 : Illustration of layered mantle convection model

(http://www.medellin.unal.edu.co/rrodriguez/PlateTectonics/plate_tectonics.htm)

Many geodynamical phenomena are still under discussion. For example, upwelling under mid-oceanic ridges is still debated, since some authors argue that the upwellings under the MOR is an active phenomenon (Morgan, 1971) while others argue that it is a passive phenomenon (Spiegelman and McKenzie, 1987; Key et al., 2013). The driving mechanisms for plate tectonics are also still under discussion. For some authors, the main driving force of plate tectonics is the basal drag (induced by the mantle convection) (Ziegler, 1993), while for others it is the slab pull (Weatherly and Katz, 2010). Some studies suggest a mix between these end-members (Conrad and Behn, 2010).

## 2.4 Secondary Mantle Convection Theory

Initially, the theory of mantle convection was developed to understand the thermal history of the Earth and to account for the driving mechanism of Alfred Wegener's theory of continental drift (Schubert et al., 2001). Besides this large-scale mantle convection, different authors have proposed that smaller-scale convection should occur beneath the lithospheric plates. This small-scale convection is also known as secondary convection. Some of the most significant numerical and laboratory experiments characterizing secondary convection have been conducted by Richter (1973) and Richter and Parsons (1975). Richter (1973) analytically and numerically solved the conservation equations to study the interaction of R-B convection with the large-scale flow. Richter and Parsons (1975) conducted laboratory experiments to study the interaction of small-scale convection with the large scale-flow in a fluid. These studies suggest the presence of rolls (either transversal or longitudinal) beneath the moving lithospheric plate. Thus, these rolls are generally called Richter rolls (Yuein and Fleitout, 1985; Korenaga and Jordan, 2003; Vidal, 2004).

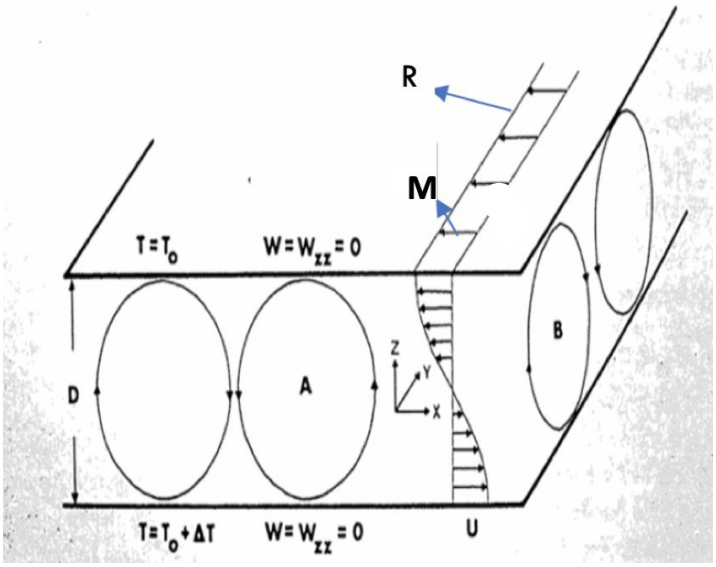


Figure 6 : Two types of convective rolls that can exist under lithospheric plates of the Earth. (Richter, 1973). 'A' denotes the transversal roll; 'B' denotes the longitudinal rolls; the arrows, indicated by 'M', denote the direction of plate motion; while 'R' represents the ridge. 'D' represents the thickness of the horizontal layer, 'T' represents the temperature, '$T_o$' being the temperature at the upper boundary while the '$\Delta T$ ' is the difference of temperature between upper boundary and lower boundary. 'U' denotes the plate velocity

According to Richter (1973), transverse rolls (denoted by 'A' in Figure 6) develop near the ridge, with axes perpendicular to the direction of the lithospheric plate motion. After a while,

transverse rolls disappear and longitudinal rolls (denoted by 'B' in Figure 6), with axes parallel to the direction of the lithospheric plate motion, develop. Furthermore, Richter (1973) modeled the change in the flow pattern regime as a function of time. This is illustrated in Figure 7.

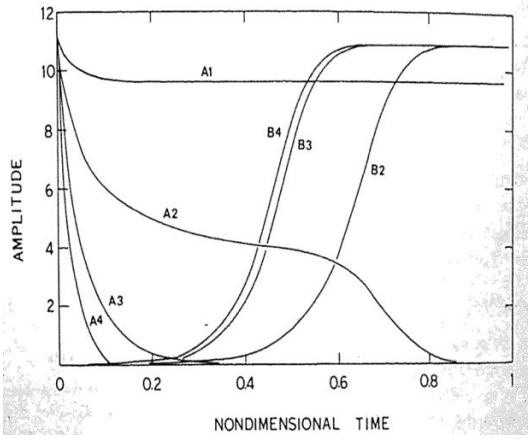


Figure 7 : Evolution of transversal rolls as a function of non-dimensional time and the amplitude of the rolls beneath the moving lithospheric plates (Richter, 1973). Richter (1973) displays the amplitude of the secondary convection rolls as a function of the non-dimensional time. Different curves from A1-A4 and B2-B4 represent the different models obtained with different model parameters like distance, velocity, temperature and time and by solving different analytical equations. The A1-A4 curves represent the amplitude of transverse rolls while the B1-B4 curves represent amplitude of the longitudinal rolls

As we can observe from his model, transverse rolls develop first, when the plate is relatively young. Gradually, as the plate moves away from the ridge, the amplitude of the transverse rolls decreases, and they eventually disappear. We then observe the development of longitudinal rolls, with axes parallel to the plate motion. The amplitude of longitudinal rolls increases with time and they become stabilized after certain time, as shown by curves B2, B3 and B4. The decay time of transverse rolls is estimated to be inversely proportional to the plate velocity (Richter, 1973). His results suggest that the faster the plate velocity, the faster the decay of transverse rolls, and the development of longitudinal rolls. According to Richter (1973), for plate velocities in excess of 2 $cmyr^{-1}$ the decay time is less than 200 M.y. One of Richter's (1973) conclusion is that, if Rayleigh-Bénard convection exists under the present lithospheric plates, it is most probably in the form of longitudinal rolls as depicted in Figure 8.

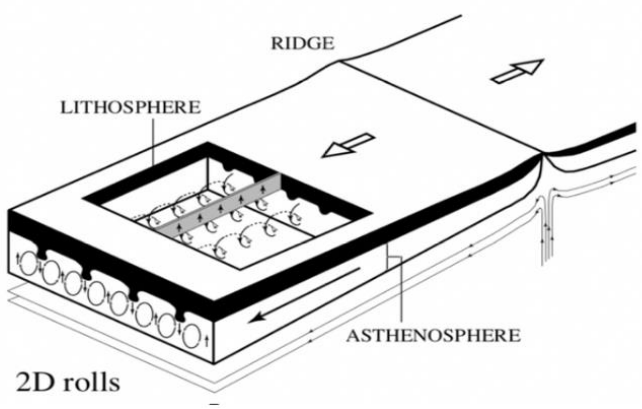


Figure 8 : Sketch of longitudinal rolls under a moving lithospheric plate as proposed by Richter (1973). Figure taken from Vidal (2004)

According to Howard (1966), when the local Rayleigh number of the fluid ($\mathrm{Ra}$) exceeds a critical value ($\mathrm{Ra}_{cr}$), dripping convective instabilities develop under a cold thermal boundary layer. The interaction between the shear flow and the dripping convective instabilities that develop under a cold thermal boundary layer has been studied experimentally by Vidal (2004) in a tank made of plexiglass walls, heated from one vertical wall and cooled from all the other sides as shown in Figure 9.

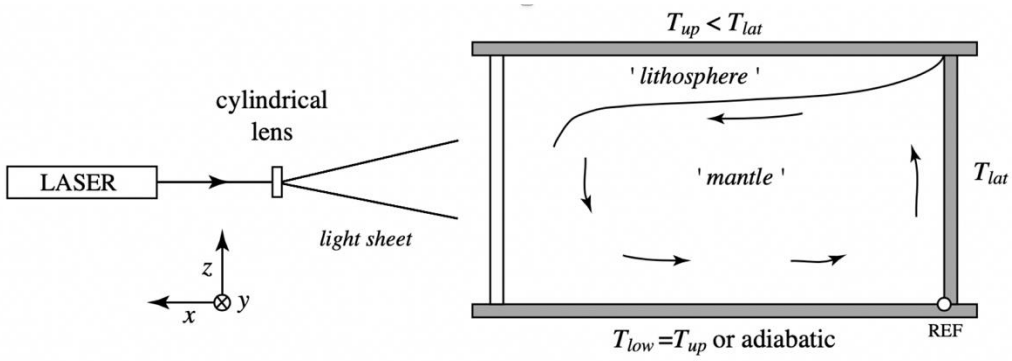


Figure 9 : Experimental setup to study interaction of two scales of convection in a horizontal fluid layer heated from one side and cooled from above (Vidal, 2004). '$T_{low}$' represents the temperature at the lower boundary, '$T_{up}$' represents temperature at the upper boundary, while '$T_{lat}$' represents temperature at the hot side wall

The upper cold boundary in the experiment is analogous to the lithospheric plate, the hot side is analogous to the ridge while the convecting fluid is analogous to the mantle. In the experiment, small-scale instabilities develop below the upper thermal boundary at a certain distance from the hot wall. Small-scale instabilities are formed as a result of gravitational instabilities created by the maximum temperature gradient between the shearing layer and the upper cold boundary layer. The distance at which instabilities first develop is called the critical distance, $d_c$ (Vidal,2004). After this critical distance, the fluids exceed the critical Rayleigh number and thus start convecting in the form of downwelling plumes (Figure 10). The organization of downwelling plumes in between the cold upper boundary layer and the large-scale convection core depends on the interaction between the shear velocity of the convecting fluids and the instability velocity. In this context, the shear velocity refers to the velocity of the shear layer beneath the upper boundary layer, whereas the instability velocity is the vertical component of the velocity field associated with the instabilities. Vidal (2004) observed that if $V_{instability}/V_{shear} < 0.1$, the shear is high enough to counteract the falling instability velocity and stabilize the flow, the convection pattern organizes itself in the form of 2D stationary longitudinal rolls with axis aligned with the shear flow (Figure 8). However, if $V_{instability}/V_{shear} > 0.1$, i.e. when the shear velocity is not strong enough to counteract the falling instabilities velocity, the level of organization decreases. In these conditions, 3D time-dependent structures are observed in the form of plumes sinking from the cold plate and driven away by the large-scale flow. Thus, Vidal (2004) demonstrates experimentally the presence of small-scale convection beneath the lithospheric plate. The two scales of convection observed in her experiment are as reported in Figure 10.

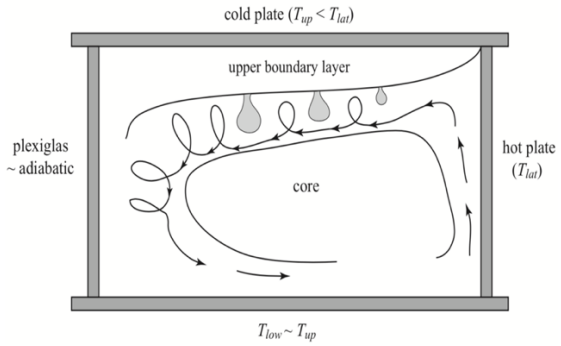


Figure 10 : Illustration of interaction of two scales of convection as observed in a laboratory experiment by Vidal (2004). '$T_{low}$' represents the temperature at lower boundary, '$T_{up}$' represents temperature at upper boundary, while '$T_{lat}$' represents temperature at upper boundary, while '$T_{lat}$' represents temperature at hot side wall

The pattern of the lithospheric instabilities varies with the parameters of the experiments conducted by Vidal (2004). For some parameters ranges, Vidal (2004) also recovers the Richter rolls described previously. Vidal (2004) shows that small-scale convection organizes mainly into two different morphologies, when sheared by the large-scale flow. For low Rayleigh number, or a low velocity ratio $V_{instability}/V_{shear}$, sublithospheric instabilities organize into Richter rolls (Figure 8), with axes aligned in the direction of plate motion. For higher Rayleigh numbers, or a high aspect ratio, instabilities take the shape of sinking cold plumes, falling from the base of the lithosphere and sheared away by the large-scale flow (Figure 10).

Korenaga and Jordan (2003) performed a 3D linear stability analysis of longitudinal rolls numerically, by solving the conservation equations. They suggest the existence of Richter rolls beneath fast-moving plates, like the Pacific plate. However, their results differ from Richter and Parsons (1975). Richter and Parsons (1975) suggest the presence of stable longitudinal rolls for Ra >= $1.4\times 10^5$, whereas Korenaga and Jordan (2003) observe that for Ra > $\sim 5\times 10^5$ the rolls will not be stable, and will evolve as time-dependent convection. The two end member models for the small-scale convection are: i) two dimensional stable Richter rolls (Richter, 1973; Richter and Parsons (1975) and ii) three-dimensional time-dependent cold sinking plumes (Vidal, 2004). The Richter rolls would be in the form of stable continuous rolls either parallel or perpendicular to the plate motion direction (Figure 6 and Figure 8), whereas cold sinking plumes would be

unstable and discontinuous, developing at a certain distance from the ridge and driven away by the large-scale mantle flow (Figure 10).

## 2.5 Secondary Mantle Convection in the Ocean Basins

The secondary convection rolls suggested by different authors are observed mainly below the Pacific plate, because it is the most rapid, but they are also observed beneath the North and South Atlantic Ocean and the Indian Ocean plates (French et al., 2013). Based on high-resolution tomography modelling, French et al. (2013) report secondary convection structures that look like quasi-periodic finger-like structures, parallel to the direction of the lithospheric plate motion (Figure 11).

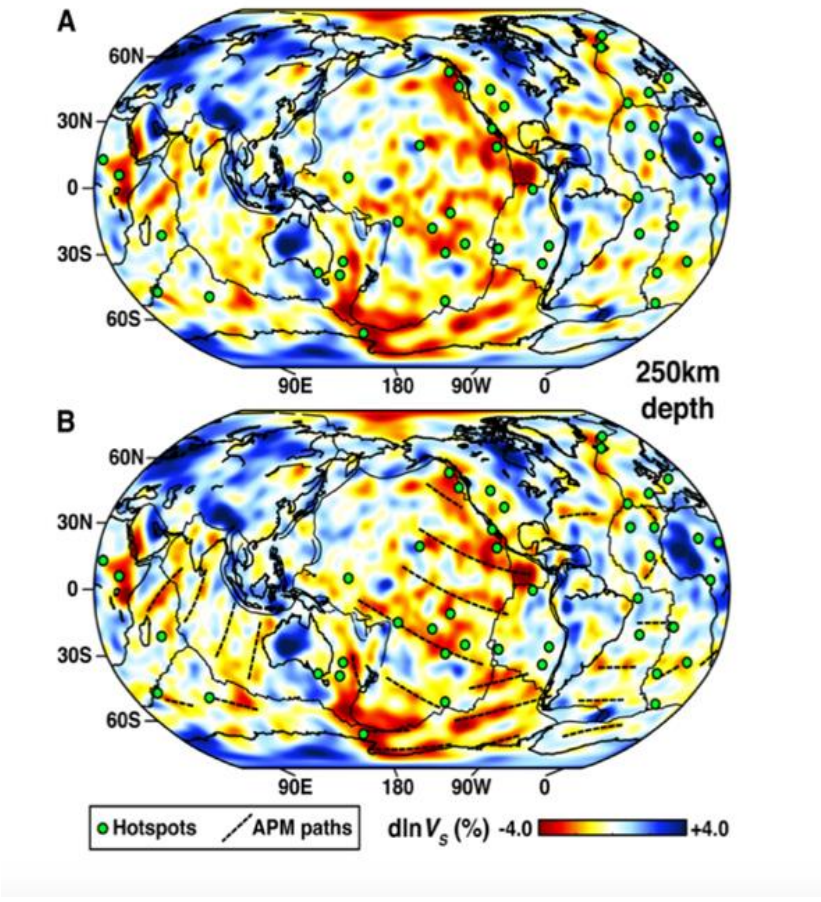


Figure 11 : SEMUCB-WM1 tomography model (French et al., 2013); color maps represent the lateral velocity variations in percentage. The dashed lines are the finger-like structures interpreted as secondary convection rolls, parallel to the plate motion direction

Despite the numerous numerical, analytical and experimental studies, there is no consensus regarding the characteristics of secondary convection, including first-order characteristics such as wavelength, orientation, depth of occurrence, or age of the lithospheric plate below which they occur. For example, French et al. (2013) observe a wavelength of 2000 km for the secondary convection in their tomography models, whereas Vidal (2004) predicts a wavelength of 200 km from her experiments. Jaupart and Parsons (1985) conducted laboratory experiments and studied the influence of viscosity structure on the development of convective instabilities in a viscous fluid cooled from above. They suggested that small-scale convective instabilities develop only at the base of lithosphere older than 70 M.y. On the other hand, Davaille and Jaupart (1994) conducted laboratory experiments in temperature-dependent viscous fluids and suggested that small-scale convective instabilities develop only after the lithosphere reaches an age of 40-65 M.y. Richter (1973) and Richter and Parsons (1975) found that the small-scale convection aligns as rolls oriented either perpendicular or parallel to the ridge. Dumoulin et al. (2001) performed numerical simulations of cooling lithosphere above a convecting mantle and suggested that the rolls are organized only parallel to the ridge.

## 2.6 Motivations to Study Secondary Mantle Convection from Geophysical Data and Models

It is difficult to extrapolate the results of analogical studies, and numerical simulations do not take into account the complexity of the real Earth. Therefore, geophysical data are the best tool for describing the characteristics and morphology of secondary convection, helping to constrain the origin and dynamics of this convective pattern. The present study constrains the characteristics of secondary convection through the analysis of geophysical data and models, such as seismic tomography models and geoid anomalies.

# Chapter 3 - Methods

## 3.1 Rationale

Multiple approaches have been utilized in the study to characterize the secondary mantle convection features. The middle and base of the lithosphere and the middle and base of the asthenosphere have been determined using several seismic tomography models. Geoid anomalies are also studied to constrain the characteristics of secondary convection features. The details of the methods utilized in our study are discussed in the following sections.

## 3.2 Seismic Tomography

Global seismic tomography models provide a snapshot of the 3D structure of the Earth's mantle, in terms of lateral seismic velocity anomalies, the variations being a function of predominantly two factors: composition and temperature. Lateral velocity variations are the departures from the radial reference models, such as PREM (Dzeiwonski and Anderson, 1981). Seismic tomography requires the solution of a large inverse problem with the help of powerful computational facilities and very sophisticated programming in order to obtain a heterogeneous seismic model consistent with the observations. Seismic tomography uses the same principles as the medical computer-aided tomography (CAT). The main difference is that the travel-times of the seismic signals from the earthquake are observed in seismic tomography rather than the attenuation of x-rays or ultrasonic rays as in CAT. For seismic tomography, the energy sources are earthquakes and the receivers are the seismic stations.

The study is mainly based on the SEMUCB -WM1 tomography model developed by French and Romanowicz (2014). This tomography model has a higher resolution when compared to other global tomography models, which enables us to image the mantle and lithosphere structure with more details. The methods developed here are also applied to other tomography models, such as SAVANI, developed by Auer et al. (2014), and S40RTS, developed by Ritsema et al. (2011), for comparison. The methods discussed in the sections below allow us to retrieve some of the

characteristics of the oceanic lithosphere and asthenosphere, the structure of which varies spatially. The study focuses on the oceanic plate situated under the Pacific Ocean. Numerical methods have been developed to automatically select particular points, such as the middle and the base of the lithosphere and asthenosphere.

### 3.2.1 Selecting the middle of the lithosphere and asthenosphere, and the base of the asthenosphere

Tomography models provide lateral seismic velocity variations in percent (dvs%) for each point of the globe, i.e. for each longitude, latitude and depth. To derive the base of the lithosphere, as well as particular points such as the middle of the lithosphere, the middle of the asthenosphere and the base of the asthenosphere, profiles showing the dvs% variation with depth are considered, for each longitude and latitude. Figure 12 shows a bathymetry/topography map (data from Becker et al., 2009) and the location of several points used to illustrate our approach.

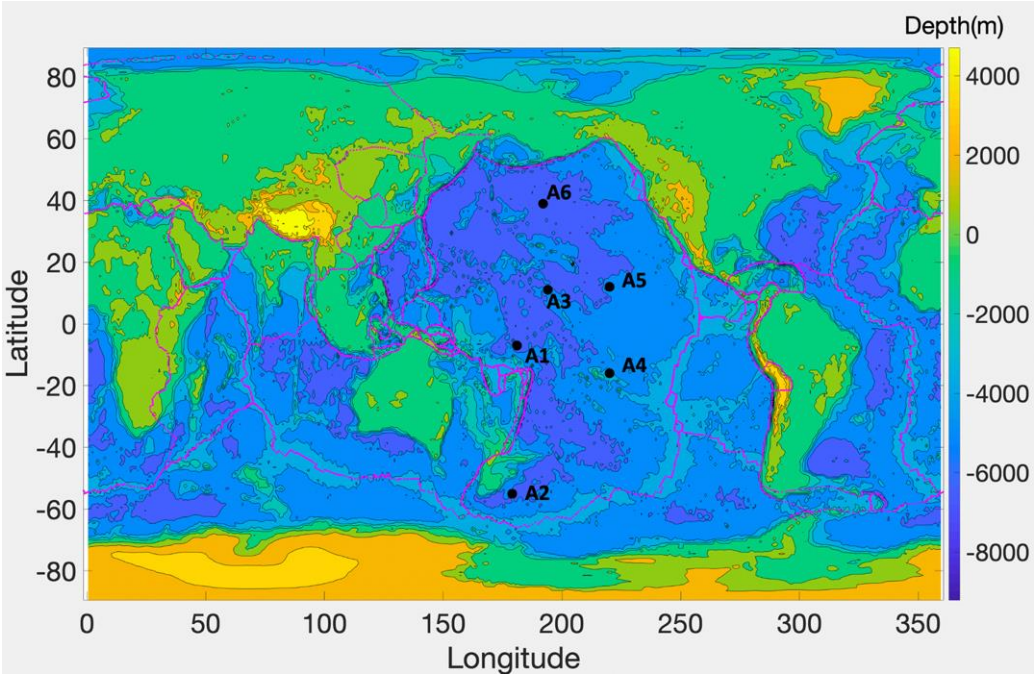


Figure 12 : Bathymetry and topography map (data from Becker et al., 2009). The magenta lines represent plate boundaries (Bird, 2003), such as mid-oceanic ridges and trenches. The black dots show six different locations A1, A2, A3, A4, A5 and A6 corresponding to longitude and latitude (181°E, 7 °S), (179°E, 55°S), (194°E, 11°N), (220°E, 16°S), (220°E, 12°N) and (192°E, 39°N), respectively. At these locations, we investigate the lithosphere and asthenosphere characteristics in the Pacific Ocean in panels (a) through (f), as illustrated in Figure 13

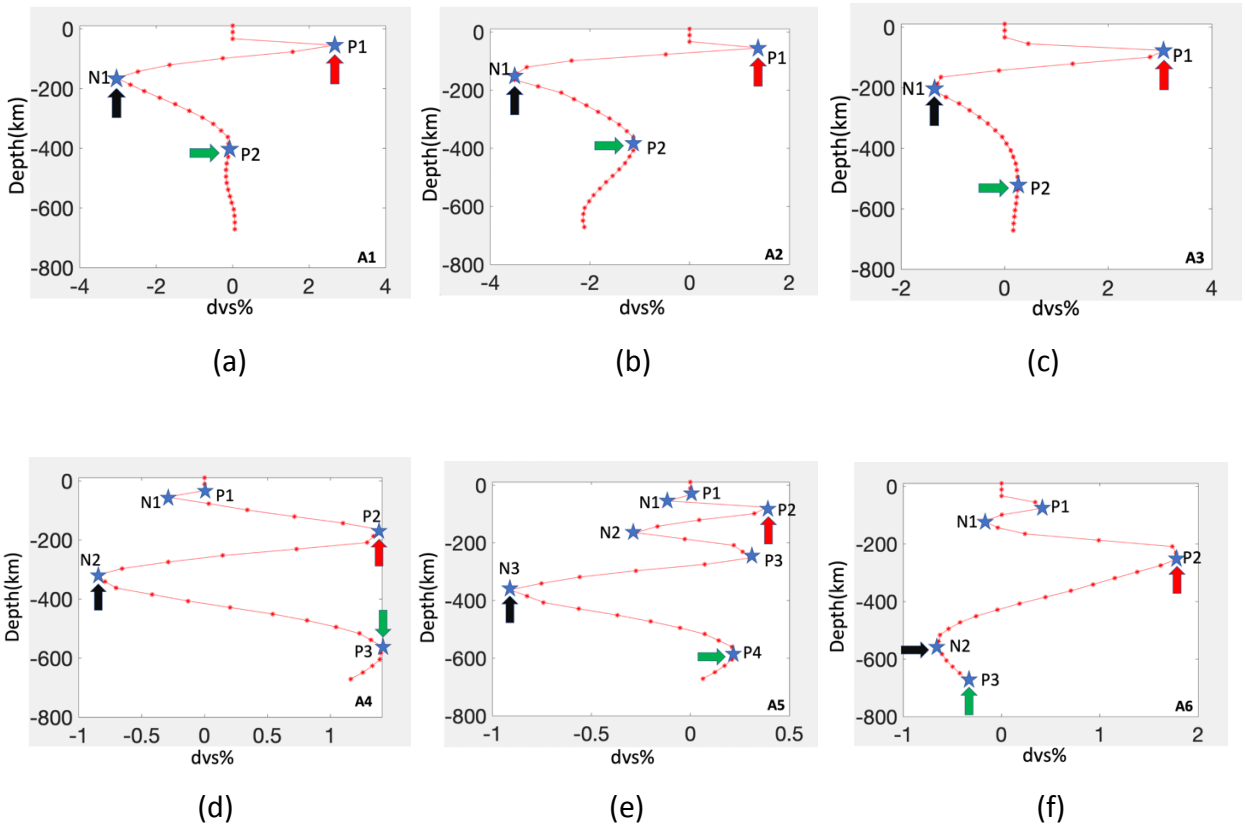


Figure 13 : Seismic velocity anomaly (dvs) provided by the SEMUCB-WM1 tomography model (French and Romanowicz, 2014) as a function of depth for six locations identified in Figure (12). Different points (P1, N1, P2, N2, P3, N3 and P4) represent the maximal and minimal dvs in the lithosphere and asthenosphere, which will be described in the following main text. Red, black and green arrows in panels a, b, c, d, e and f show the middle of the lithosphere, the middle of the asthenosphere and the base of the asthenosphere respectively

The dvs profiles displayed in Figure 13 a, b and c show a “classical behavior”, displaying positive dvs in the shallowest 100 km, the lithosphere, as expected. The seismic velocity is higher in the lithosphere because it is colder and therefore the seismic waves travel faster in the lithosphere. Immediately beneath the lithosphere, the dvs are negative. This is expected in the asthenosphere, defined initially as a channel of low seismic velocities. There are other definitions. For example, from the petrological perspective, the base of the asthenosphere is defined considering the mineralogical phase changes, occurring at depths 410-660 km. In this study, we use the geodynamical definitions, which state that the asthenosphere is a low seismic velocities channel, located at the base of the lithosphere. A Matlab code has been developed to automatically select the depth associated with the maximum dvs in the lithosphere (represented

by red arrows in Figure 13), which will be referred to in the following as the middle of the lithosphere, the depth associated with the minimum dvs in the asthenosphere (represented by black arrows in Figure 13), which will be referred to in the following as the middle of the asthenosphere. For depths greater than the middle of the asthenosphere, we select another point, which corresponds to a slope change (represented by green arrows in Figure 13). We will call this point “base of the asthenosphere”. The points represented by red, black and green arrows (Figure 13) are actually all inflection points, associated with a change of slope in the dvs vs. depth profiles.

However, sometimes the dvs vs. depth pattern is more complex. The profiles (A4, A5 and A6) shown in Figure 13 d, e and f display several minima in the asthenosphere and several maxima in the lithosphere. For example, in Figure 13 d, e and f, P1, P2, P3 and P4 are first, second, third and fourth maxima respectively whereas N1, N2 and N3 are first, second and third minima respectively. One possible reason for several maxima and several minima in these profiles is that tomography models report the complex structure created by several physical phenomena occurring simultaneously but at different scales, including the interactions of plumes with the lithosphere.

In these cases, the middle of the asthenosphere is determined first, by selecting the depth corresponding to the minimum dvs encountered along the profile (black arrows in Figure 13 d, e, f). To determine the middle of the lithosphere, the maximum dvs is selected between depths 0 and the depth corresponding to the middle of the asthenosphere (red arrows in Figure 13 d, e, f). The base of the asthenosphere, corresponding to a change of slope of the dvs vs. depth profile, for depths greater than the middle of the asthenosphere is also selected (green arrows in Figure 13 d, e, f). The base of the asthenosphere cannot always be selected, because a slope change in the dvs vs. depth profile is not always observed for depths greater than the middle of the asthenosphere (Figure 13 f).

### 3.2.2 Determination of the base of the lithosphere

The lithosphere is defined as rigid outer layer of the Earth overlying the weaker and plastic asthenosphere. The base of the lithosphere in theory can be defined by an isotherm (An et al., 2015; Bodine et., 1981; Sleep, 2008). As such, it corresponds to a particular isovalue of the seismic velocity anomaly, dvs. Note that there are other definitions, considering the composition of these geological objects for example. Here we will focus on the geophysical definition and will define the base of the lithosphere by an isovalues of dvs. There is however no clear definition stating by which dvs the lithosphere is defined in tomography models. Moreover, the amplitude of the seismic velocity anomalies, dvs, varies according to the dataset used and to the inversion methods used to obtain the tomography models. In other words, dvs varies according to the different tomography models. In general, the newest models, such as SEMUCB-WM1, provide higher amplitude of dvs when compared to older models, such as S40RTS. Therefore, several values of dvs (dvs=1%, 1.5% and 2%) have been investigated to determine the base of the lithosphere. We have developed an approach to retrieve the depths corresponding to these isovalues (dvs=1%, 1.5% and 2%). We consider the dvs vs. depth profiles displayed in Figure 13, but only between depths 0 and 160 km, and select the depth where the dvs is closest to the considered isovalues like 1%, 1.5% and 2%. Although based on the same data (tomography models), this approach of characterizing the lithosphere and asthenosphere differs from the previous approach, which was about selecting the middle of the lithosphere and asthenosphere, whereas here we are trying to establish the base of the lithosphere. We expect the comparison between these methods to provide more constraints on the characteristics of the lithosphere and asthenosphere.

## 3.3 Study of Geoid Anomalies

The geoid is the hypothetical shape of Earth or the surface with equal gravitational potential. It coincides with mean sea level and is perpendicular to the pull of gravity. It is a reference surface

from which ocean depths and topographic heights are measured. The geoid anomalies observed over the Earth are reported in Figure 14.

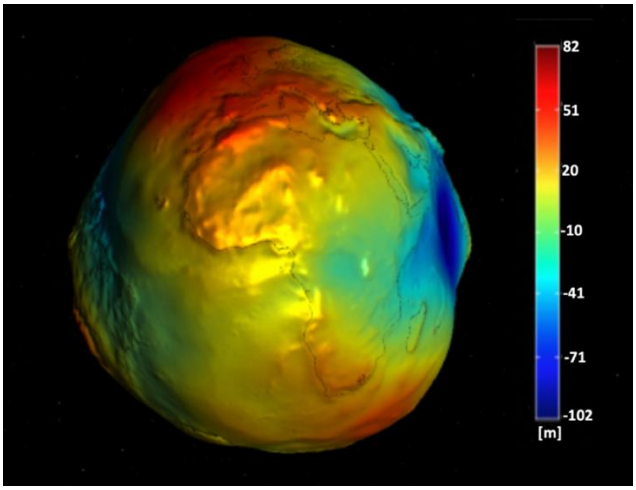


Figure 14 : Geoid anomaly over the Earth. Blue colors represent areas where the geoid is below the hydrostatic ellipsoid, and red areas are above the ellipsoid. The color bar represents the geoid anomaly in meters. (https://gisgeography.com/geoid-mean-sea-level/)

Geoid anomalies are the deviations of the geoid from an idealized hydrostatic ellipsoid. There are two large positive geoid anomalies reported on Earth. They lie beneath Africa and the South Pacific and correlate roughly with the two Large Low Shear Velocity Provinces (LLSVPs) (Condie, 2016). Geoid anomalies are related to the internal structure of Earth and to mantle dynamics (Hager and Richards, 1989).

Haxby and Weissel (1986), for example, report evidence for the early development of convective instability beneath the upper cold thermal boundary layer, from gravity anomalies and residual sea surface heights derived from Seasat altimeter data. They observe subtle lineated patterns of gravity anomalies with wavelengths ranging from 150 km to 500km over the younger portions of the Pacific and Indo-Australian plates. The trend of the lineations is parallel to plate motions. Furthermore, based on their altimeter data, the authors suggest the development of small-scale convection started within 5-10 Ma of the start of plate cooling. Based on their observation of the wavelength of the gravity anomalies, and their correlation with differences in crestal depth of the mid-oceanic ridges, Anderson et al. (1973) proposed that there must be some kind of flow associated with the asthenosphere, which caused the observed wavelength of the gravity

anomalies. Our aim is to constrain the lithosphere destabilization, which is induced by the asthenospheric flow under the oceanic plates, as explained in the introduction. We will filter the EGM2008 geoid (Pavlis et al., 2012) through a spherical filter, which allows us to extract the geoid signature for different ranges of order and degrees.

In this study we have used the geoid provided by Pavlis et al. (2012), EGM2008. In Figure 15, we display the geoid anomalies filtered for several order and degree ranges, to illustrate the output of the method.

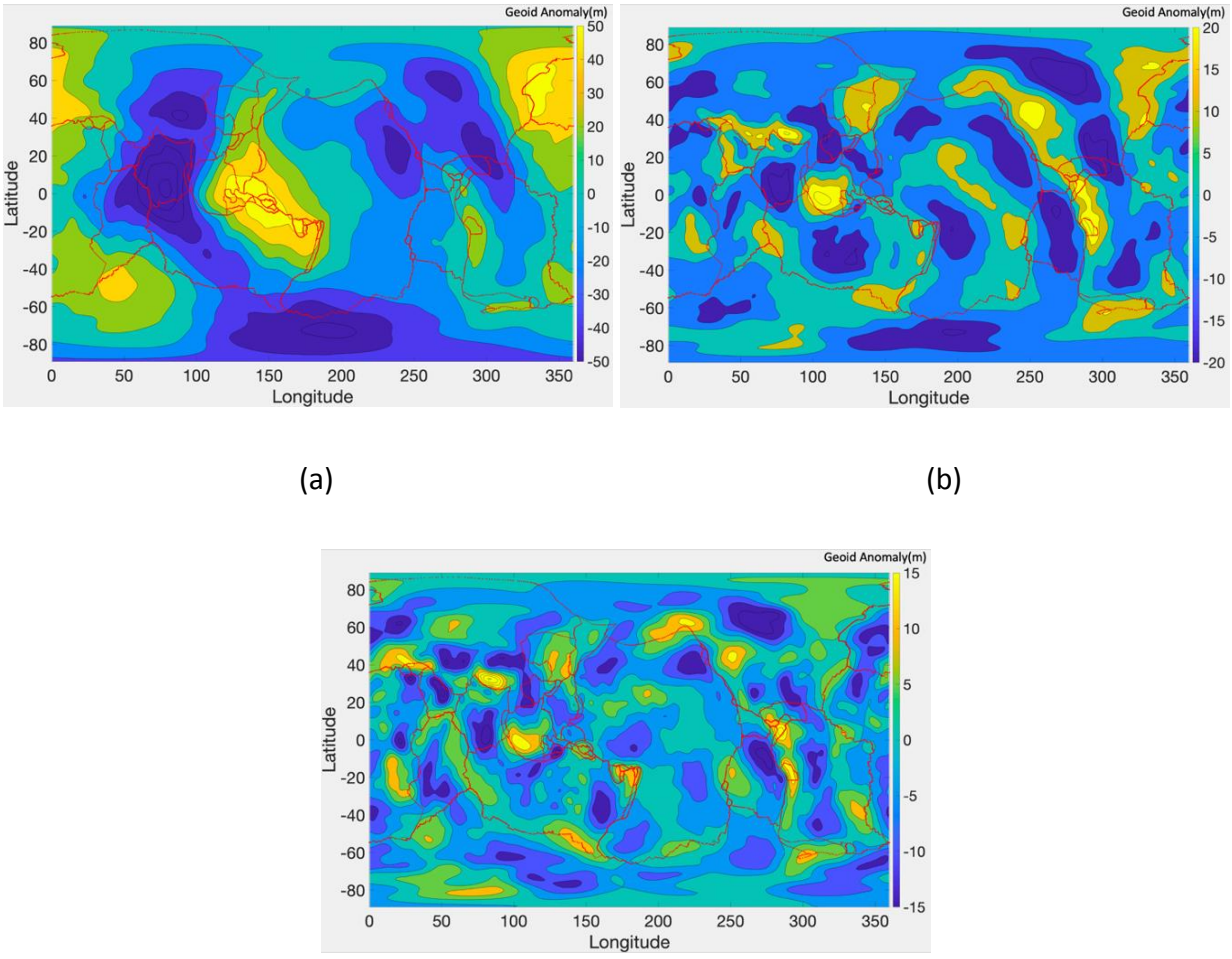


Figure 15 : Observed geoid anomalies (in meters) (EGM2008 model from Pavlis et al., 2012) filtered for (a) l=2-31, (b) l= 6-40, (c) l=8-40. The red lines represent plate boundaries (Bird, 2003), such as mid-oceanic ridges and trenches

Note how the amplitude of the geoid anomalies decreases with increasing order and degree (Figure 15).

# Chapter 4 - Results

The purpose of this study is to characterize secondary mantle convection, and the lithospheric destabilization it induces, using geophysical data and models. In order to characterize the lithospheric destabilization, the middle and base of the lithosphere, and the middle and base of the asthenosphere have been determined from three tomography models: i) SEMUCB-WM1 (French and Romanowicz, 2014), ii) SAVANI (Auer et al., 2014), and iii) S40RTS (Ritsema et al., 2011), using the approach described in section 3, 'Methods'. The EGM2008 geoid (Pavlis et al., 2012) has also been filtered with different orders and degrees in order to investigate the correlation between geoid anomalies and lithospheric destabilization. We also compare the lithospheric instabilities to geophysical data and models, such as plate kinematics, seafloor age, theoretical thickness of the lithosphere, the distance from the mid-oceanic ridges and bathymetric features such as hotspots and oceanic plateaus.

## 4.1 Characteristics of the lithosphere and asthenosphere from the SEMUCB-WM1 tomography model

The map showing the middle of the lithosphere is displayed in Figure 16. It has been obtained by considering the seismic velocity anomalies, dvs, provided by the SEMUCB-WM1 tomography model (French and Romanowicz, 2014), and the approach previously described in section 3, 'Methods'.

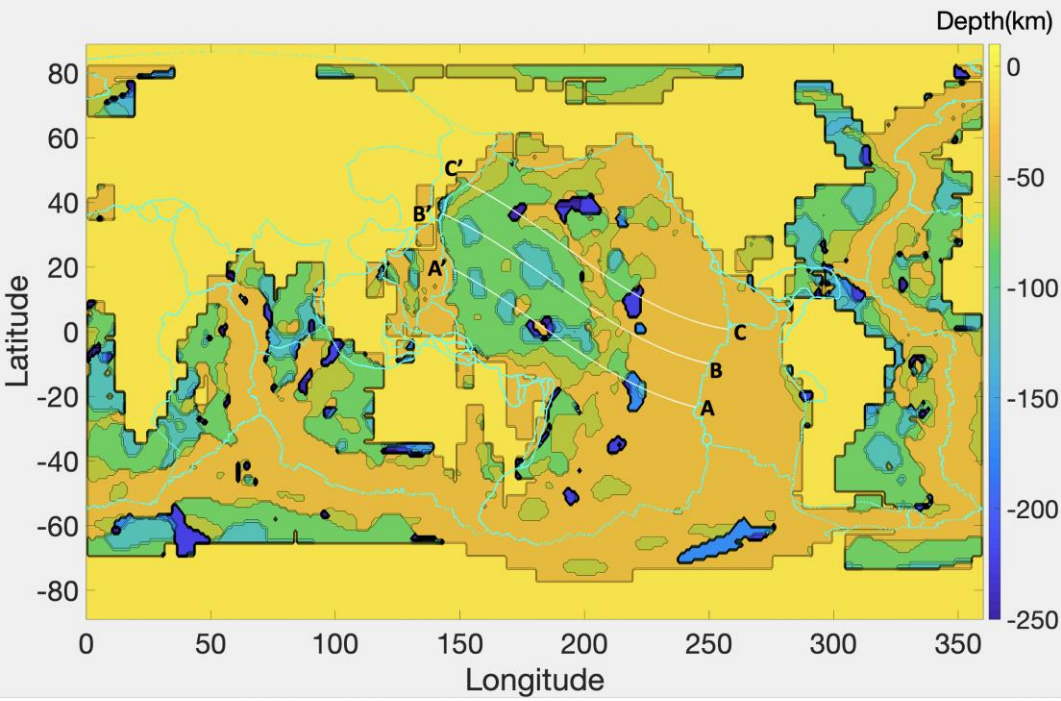


Figure 16 : Map of the middle of the lithosphere based on the SEMUCB-WM1 tomography model (French and Romanowicz, 2014) obtained with approach previously described. The cyan lines represent plate boundaries (Bird, 2003), such as mid-oceanic ridges and trenches. The white lines (AA', BB' and CC') represent the trajectory of present-day plate motion direction (taken from Adam et al., 2015), along which depth cross sections are investigated

The variations in depth to the middle of the lithosphere are displayed in Figure 16. These depths vary from about 35 km near the mid-oceanic ridges to about 100 km far away from the mid-oceanic ridges in the northwestern part of the Pacific plate. Near the mid-oceanic ridges, few lithospheric discontinuities are noticed. This is mainly due to the fact that in this region, the lithosphere is not actually "seen" in tomography models. Some regions are associated with anomalous depths of about 165 km to 250 km. For example, at longitude 221°E and latitude 18°S, there is a 600 km wide and 1100 km long anomaly observed. At longitude 220°E and latitude 10°N there is another 600 km wide and 900 km long anomaly. Other anomalies are noticed at longitude 198°E and latitude 40°N (500 km wide and 1800 km long), longitude 174°E and latitude 37°N (400 km wide and 600 km long). In the middle of the Pacific plate, anomalous depths of about 100 km are observed for example around the longitude 181°E and latitude 20°N (1300 km wide 2500 km long), longitude 191°E and latitude 1°N (600 km wide and 2500 km long), longitude 154°E and latitude 31°N (700 km wide and 900 km long), longitude 157°E and latitude 15°N (600

km wide and 900 km long) and around longitude 169°E and latitude 7°N (700 km wide and 900 km long).

The maps showing the base of the lithosphere obtained with dvs=1%, 1.5% and 2% are displayed in Figure 17 a, b and c respectively. They have been obtained by considering the seismic velocity anomalies, dvs, provided by the SEMUCB-WM1 tomography model (French and Romanowicz, 2014), and the approach previously described in section 3, 'Methods'.

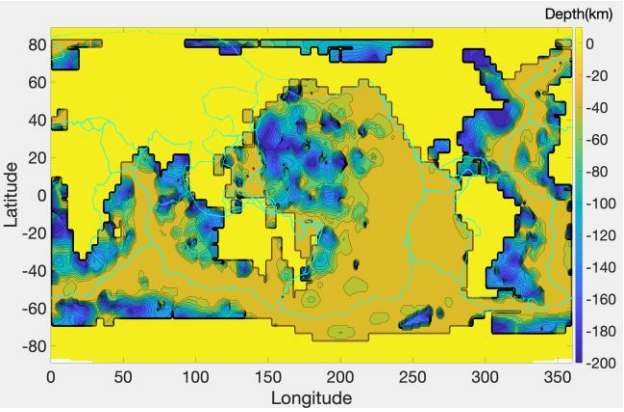


(a)

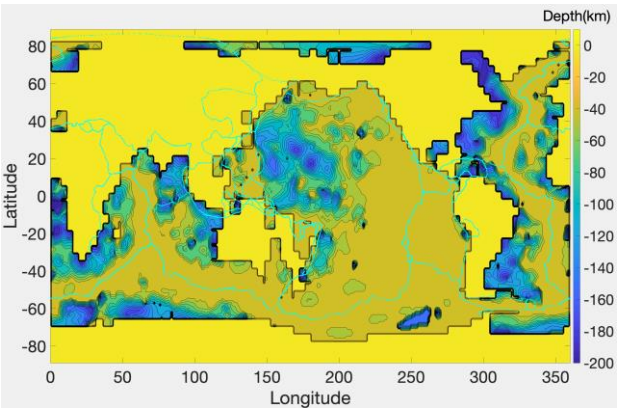


(b)

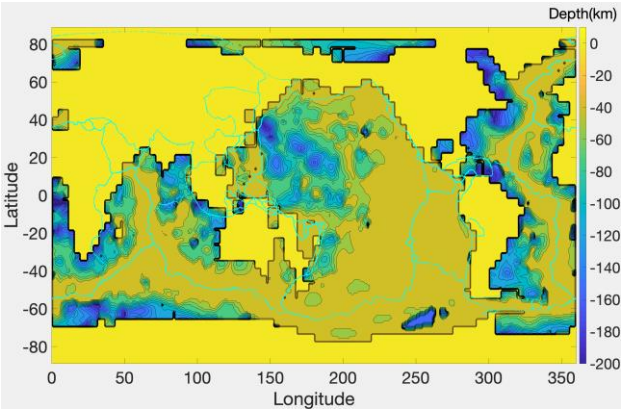


(c)

Figure 17 : Map of the base of the lithosphere based on SEMUCB-WM1 tomography model (French and Romanowicz, 2014) obtained by plotting the depths of the base of the lithosphere determined by different isovalues. a) dvs=1%; b) dvs=1.5%; c) dvs=2%. The cyan lines represent plate boundaries (Bird, 2003), such as mid-oceanic ridges and trenches

The depths to the dvs=1%, 1.5% and 2% isovalues show very similar patterns (Figure 17). Figure 18 shows the map obtained by plotting the depth to the base of the lithosphere determined with dvs=2% minus the depth to the base of the lithosphere determined by dvs=1%.

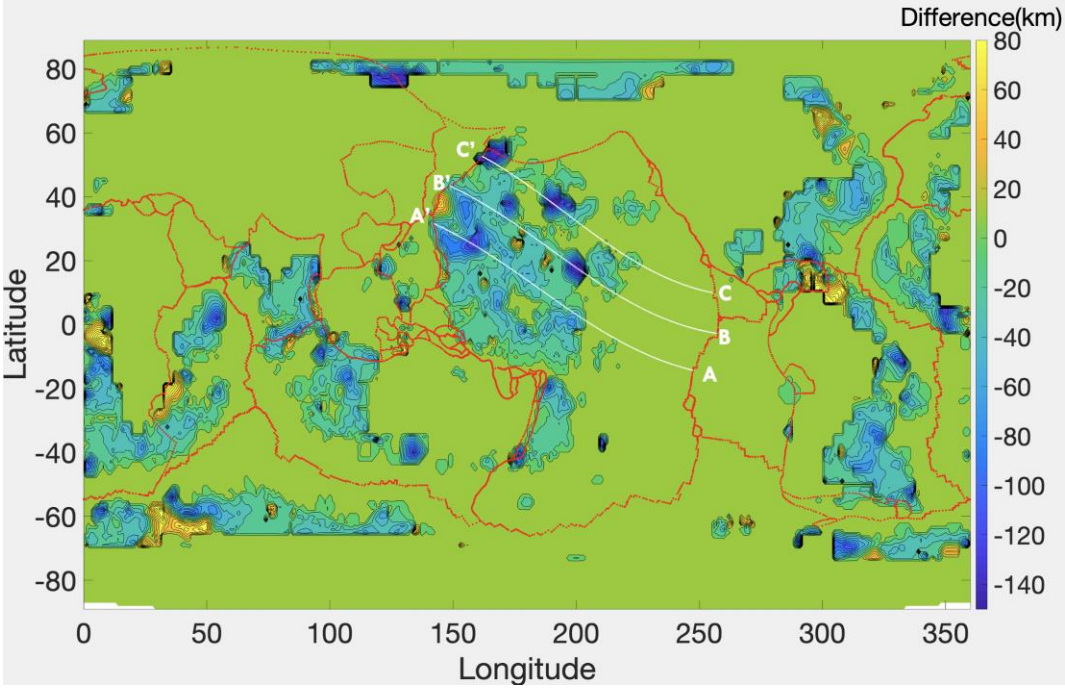


Figure 18 : Map of the difference in the depth to the base of the lithosphere determined with dvs=2% and the depth to the base of the lithosphere determined by dvs=1%, based on the SEMUCB-WM1 tomography model (French and Romanowicz, 2014). The red lines represent plate boundaries (Bird, 2003), such as mid-oceanic ridges and trenches. The white lines (AA', BB' and CC') are trajectories representative of the present-day plate motion (taken from Adam et al., 2015) along which the depth cross sections are investigated

The difference between the two models ranges between +80 and -140 km, but it varies mainly between 0 and 20 km, except in a few regions like around longitude 160°E and latitude 25°N, or at longitude 200°E and latitude 15°N, and around longitude 190°E and latitude 40°N where it is about -140 km.

Figure 19 represents the uncertainty in percentage obtained from the data displayed in Figure 18 by dividing the difference in depths (between the dvs=2% and dvs=1% isosurfaces) by the mean value of the depths determined by the three isovalues dvs=1%, 1.5% and 2%.

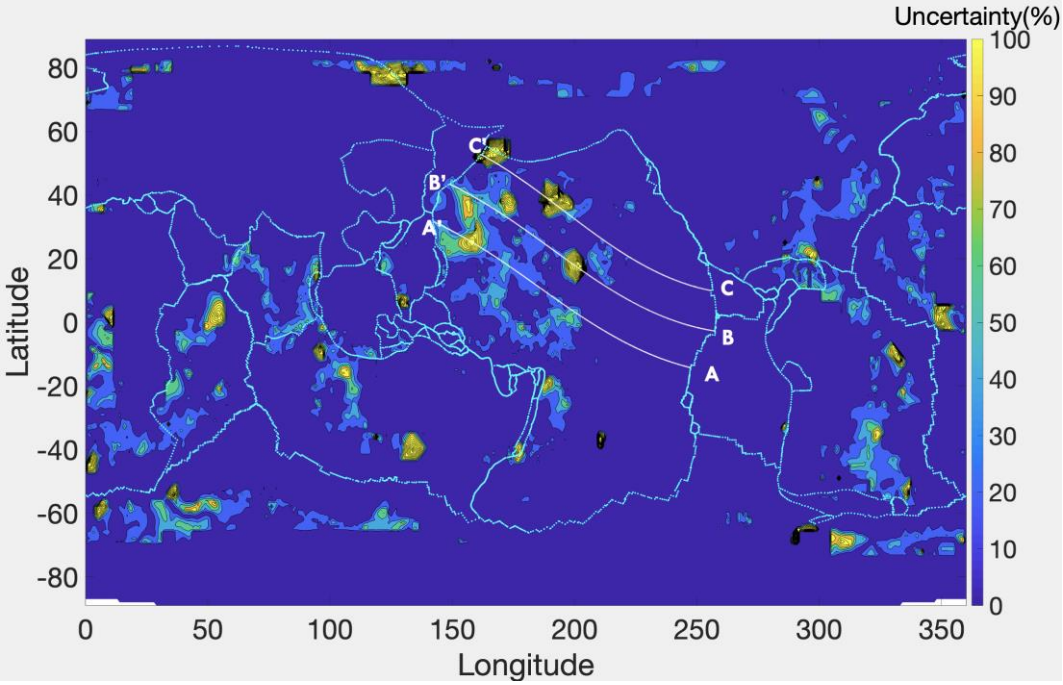


Figure 19 : Map of the uncertainty in percentage obtained from the data displayed in Figure 18, by dividing the difference in the depths (between the dvs=2% and dvs=1% isosurfaces) by the mean value of the depths determined by the three isovalues dvs=1%, 1.5% and 2%. These results have been obtained with the SEMUCB-WM1 tomography model (French and Romanowicz, 2014). The cyan lines represent plate boundaries (Bird, 2003), such as mid-oceanic ridges and trenches. The white lines (AA', BB' and CC') are trajectories representative of the present-day plate motion (taken from Adam et al., 2015) along which the depth cross sections are investigated

The uncertainty represented in Figure 19 varies from 0 to 100%. Most regions are associated with a 0-20% uncertainty. Larger uncertainties, reaching sometimes 100% are found locally, around longitude 160°E and latitude 25°N for example, or at longitude 200°E and latitude 15°N, and around longitude 190°E and latitude 40°N.

The yellow regions in Figure 20 represent areas where the uncertainty in percentage, displayed in Figure 19, is greater than 30%. The blue regions represent areas where the uncertainty is less than or equal to 30%. Most of the Pacific plate is associated with an uncertainty smaller than 30%.

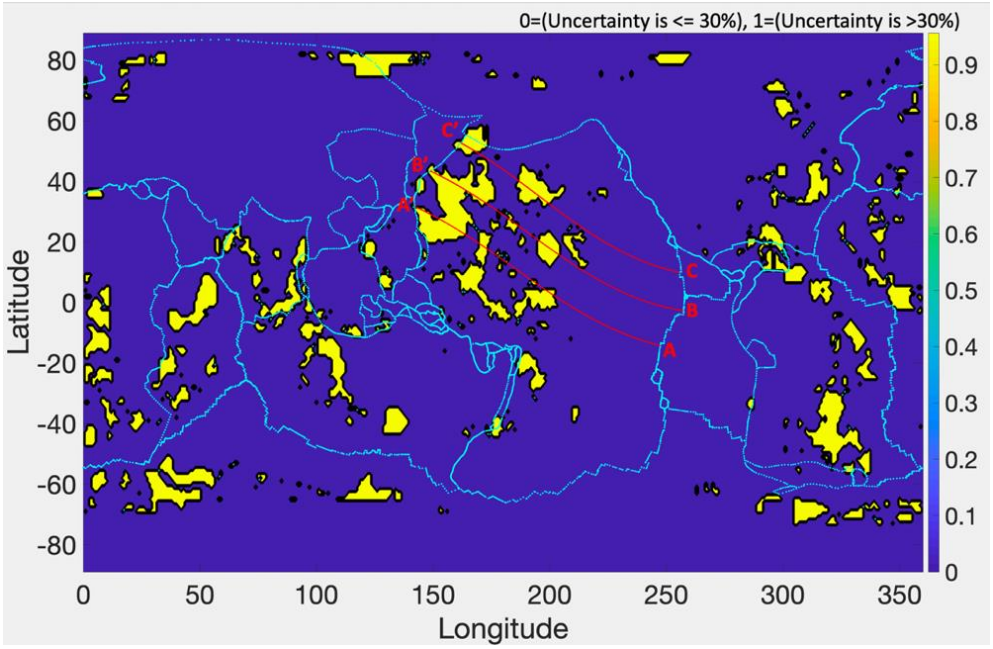


Figure 20 : Map of the regions where the uncertainty in percentage displayed in Figure 19 is greater than 30%, in yellow, and less than or equal to 30%, in blue. These results have been obtained with the SEMUCB-WM1 tomography model (French and Romanowicz, 2014). The cyan lines represent plate boundaries (Bird, 2003), such as mid-oceanic ridges and trenches. The red lines (AA', BB' and CC') are trajectories representative of the present-day plate motion (taken from Adam et al., 2015) along which the depth cross sections are investigated

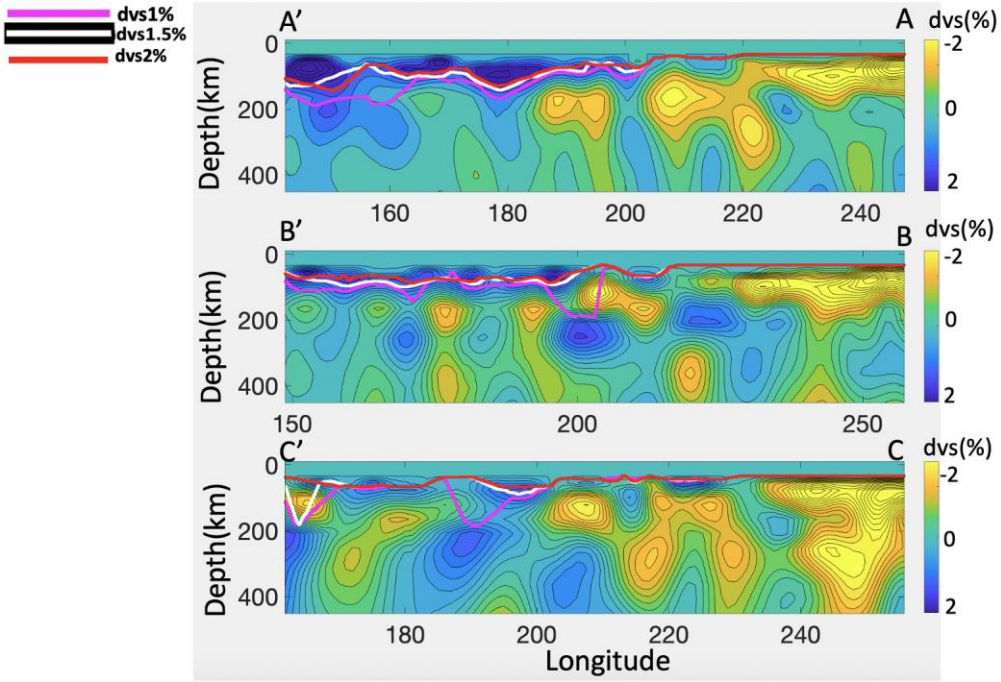


Figure 21: Depth cross section along the trajectories represented in the Figure 18, 19 and 20 for SEMUCB-WM1 tomography model (French and Romanowicz, 2014). The magenta, white and red lines represent the base of lithosphere determined by dvs=1%, 1.5% and 2%, respectively

Figure 21 show depth cross sections along the profiles AA', BB' and CC' represented in Figure 18 19 and 20. We observe that the depths represented by three lines give similar results in most of the regions. Local departures are observed around longitude 160°E in AA' profile, or at longitude 200°E in BB' profile, and around longitude 190°E in CC' profile. Our final determination of the base of the lithosphere uses the depth computed with dvs=1.5% (chosen arbitrarily), when the uncertainty displayed in Figure 19 is smaller than 30% (displayed in blue in Figure 20). For regions where this uncertainty is bigger than 30 % (displayed in yellow in Figure 20), the mean on the depths computed with the three values (dvs=1%, dvs=1.5% and dvs=2%) is imposed. The final map is displayed in Figure 22. It is representative of the base of the lithosphere obtained for SEMUCB-WM1 tomography model (French and Romanowicz, 2014).

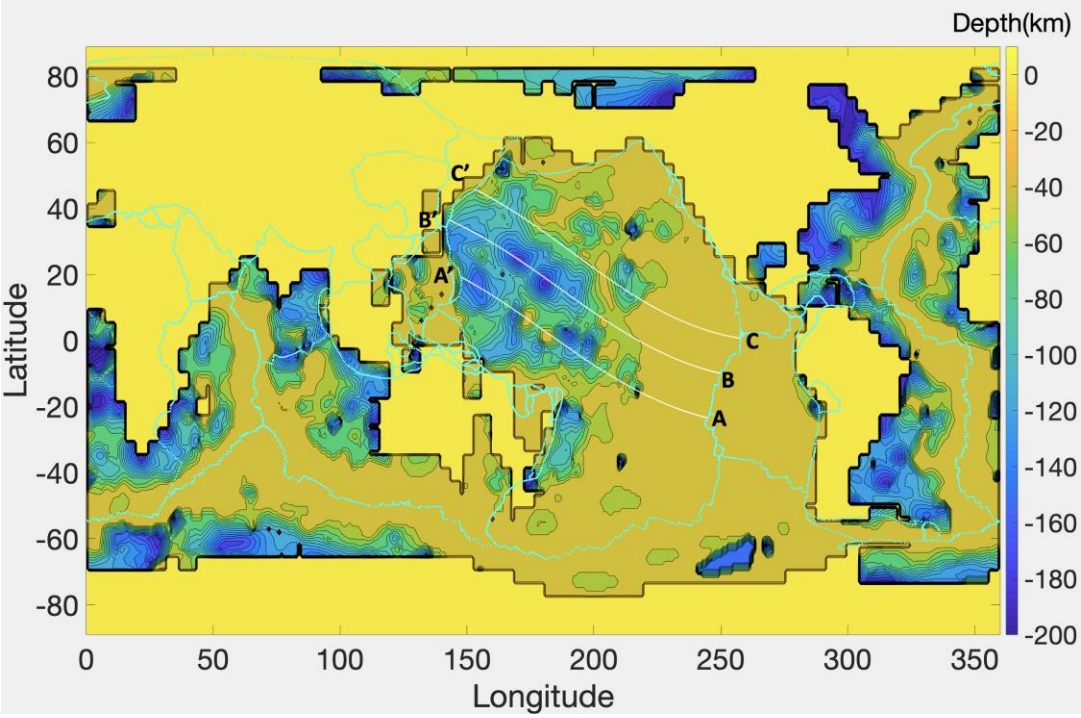


Figure 22 : Map of the base of the lithosphere based on SEMUCB-WM1 tomography model (French and Romanowicz, 2014) obtained by considering the depths to the dvs=1.5% isosurface when the uncertainty (Figure 19) is less than 30% (regions displayed in blue in Figure 20). When the uncertainty is greater than 30%, we impose the mean values of the depths determined by the dvs=2%, dvs=1.5% and dvs=1% isovalues. The cyan lines represent plate boundaries (Bird, 2003), such as mid-oceanic ridges and trenches. The white lines (AA', BB' and CC') represent the trajectory of present-day plate motion direction (taken from Adam et al., 2015) along which depth cross sections are investigated

The depths to the base of the lithosphere vary from about 40 km near the mid-oceanic ridges to about 180 km far away from the mid-oceanic ridges, as observed in Figure 22. Far away from the mid-oceanic ridges, in the northwest part of the Pacific plate, the base of the lithosphere is deeper (about 180 km). The anomalously deep regions seen in Figure 16 are also seen in Figure 22, although the depth of these anomalies varies. When the base of the lithosphere is deeper, the middle of the lithosphere is deeper as well. This can be observed in the depth cross section represented in Figure 24, where the dashed magenta line represents the middle of the lithosphere and the white continuous line represents the base of the lithosphere.

In Figure 22, there are several roundish anomalies, near the mid-oceanic ridges on the Pacific and Antarctic plates. These anomalies are also observed in the middle of the Pacific plate. If these anomalies were connected by a line, we would obtain a band almost parallel to the mid-oceanic ridges. In the northwestern part of the Pacific plate, we observe longer discontinuous anomalous regions.

The map showing the middle of the asthenosphere is displayed in Figure 23. It has been obtained by considering the seismic velocity anomalies, dvs, provided by the SEMUCB-WM1 tomography model (French and Romanowicz, 2014), and the approach previously described in section 3, ‘Methods’.

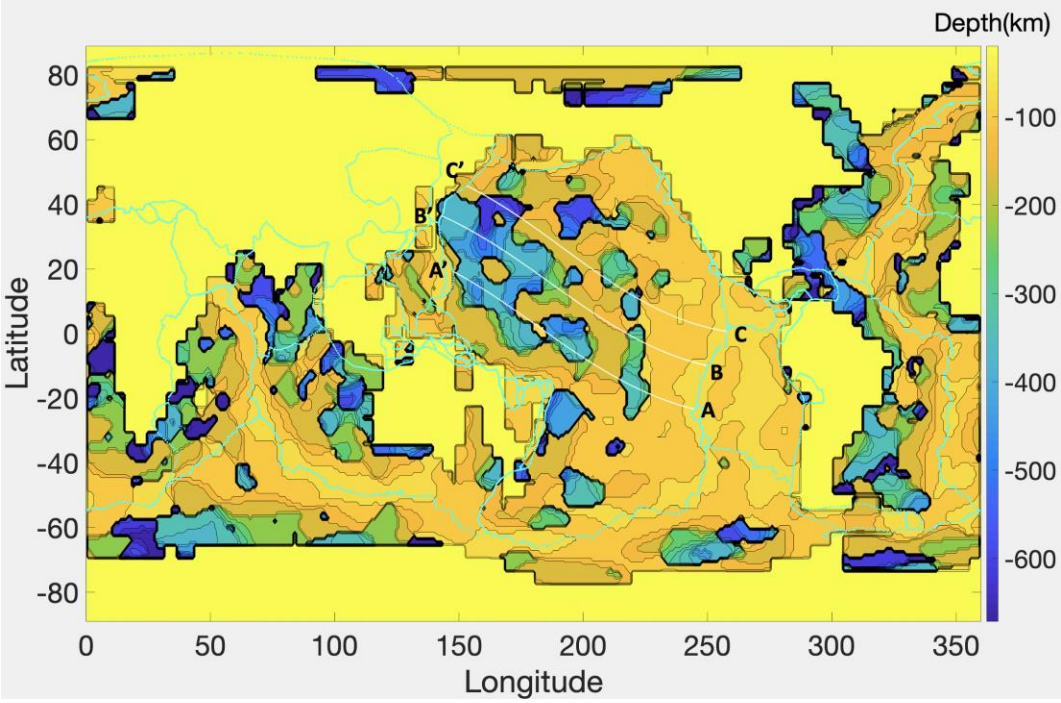


Figure 23 : Map of the middle of the asthenosphere based on SEMUCB-WM1 tomography model (French and Romanowicz, 2014) obtained with approach previously described. The cyan lines represent plate boundaries (Bird, 2003), such as mid-oceanic ridges and trenches. The white lines (AA', BB' and CC') represent the trajectory of present-day plate motion direction (taken from Adam et al., 2015) along which depth cross sections are investigated

In Figure 23, the depth of middle of the asthenosphere varies from about 100 km near the mid-oceanic ridges to about 450 km far from the mid-oceanic ridges. Depth cross section along the trajectories represented in Figure 23 are represented in Figure 24 and show our approximation of the middle of the asthenosphere. In some of the regions, like around longitude 165°E and latitude 39°N, and around longitude 200 °E and latitude 39°N, the depth to the middle of the asthenosphere is very deep, about 650 km. The anomalous patterns observed in the map of the base of the lithosphere (Figure 22) are observed in the map of the middle of the asthenosphere (Figure 23) as well. However, few more anomalies are observed in the map of the middle of the asthenosphere (Figure 23) than are observed in the map of the base of the lithosphere (Figure 22), for example: anomalies around longitude 187°E and latitude 57°S, around longitude 200°E and latitude 50°S and longer anomaly around longitude 220°E and latitude 10°S.

In the Figure 24, the depth cross sections along the trajectories represented in the Figures 16, 22 and 23 is displayed.

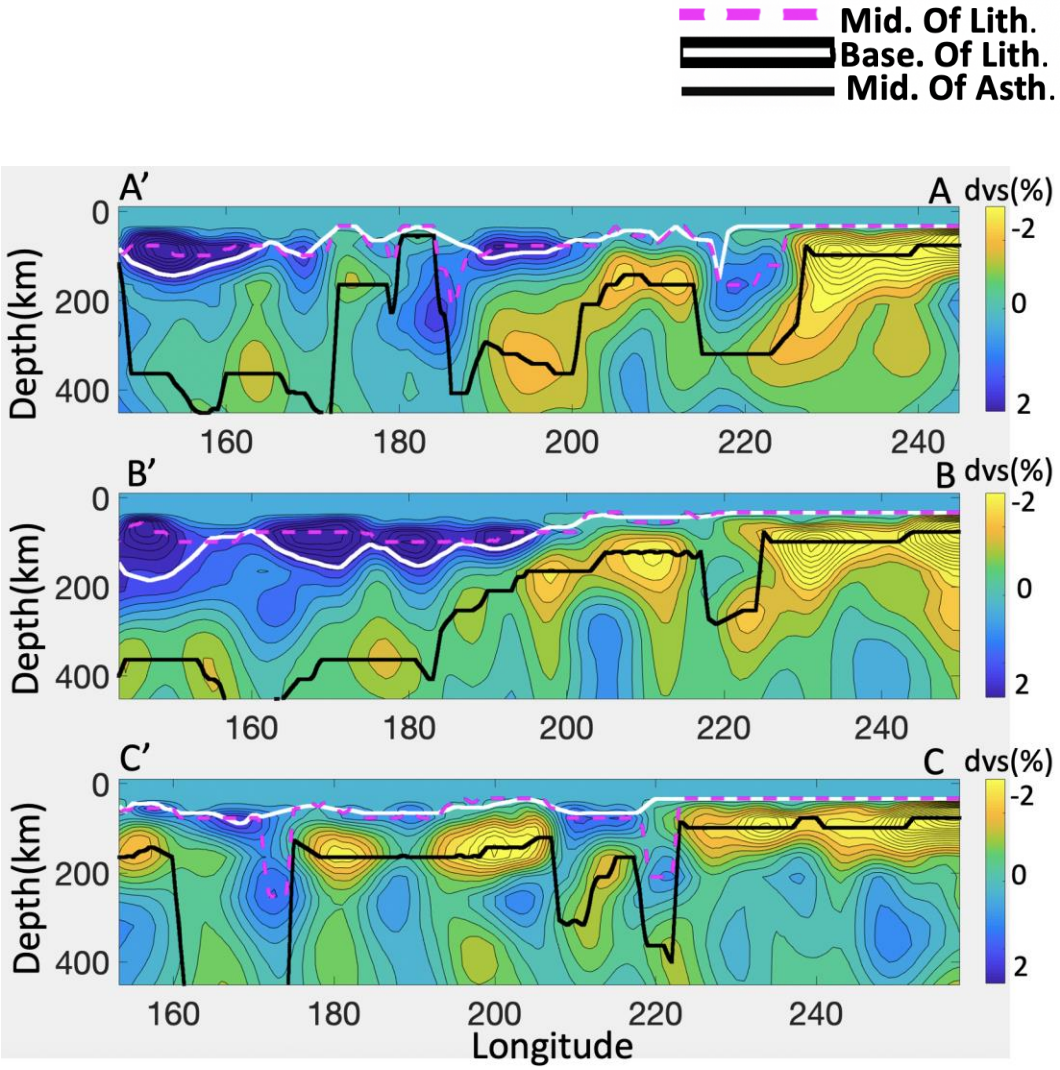


Figure 24 : Depth cross section along the trajectories represented in the Figure 16, 22 and 23 for SEMUCB-WM1 tomography model (French and Romanowicz, 2014). The black line represents the middle of the asthenosphere, the white continuous line represents the base of the lithosphere obtained by tracking the dvs=1.5% and the dashed magenta line represents the middle of the lithosphere

The depth cross sections in the Figure 24, show the dvs from the SEMUCB-WM1 tomography model (French and Romanowicz, 2014), as well as the particular points retrieved by our study. We observe that the base of the lithosphere, represented by the white line, is generally encompassed in between our estimate of the middle of the lithosphere (dashed magenta line in

Figure 24) and our estimate of the middle of the asthenosphere (black line in Figure 24). The base of the lithosphere and the middle of the lithosphere could be determined nearly in all the regions except near the East Pacific Rise. Near the mid-oceanic ridge, the resolution of the tomography model (~400 km laterally) does not allow the characterization of the lithosphere, which is probably relatively thin. The depth of the middle of lithosphere and the base of the lithosphere is automatically set to ad hoc value of 33 km in such case. The tomography models show seismically broad slow regions near the East-Pacific rise (around longitude 240$^{o}$E in profiles AA', BB' and CC' in Figure 24). However, our method allows us to retrieve the middle of the asthenosphere (black line in Figure 24) near the East-Pacific rise. The instability of the lithosphere is often accompanied by the instability of the underlying asthenosphere, as seen along profiles AA', BB' and CC' in Figure 24. Therefore, it is important to study both variations of the middle of the lithosphere and asthenosphere depths, even if our focus in this study is to characterize the destabilization of the lithosphere. The method to automatically determine the depths to the middle of the lithosphere and the middle of the asthenosphere is functioning. The dashed magenta line and black continuous line in Figure 24 correctly follow the maximum in the lithosphere and the minimum in the asthenosphere, respectively.

The map showing the base of the asthenosphere is displayed in Figure 25. It has been obtained by considering the seismic velocity anomalies, dvs, provided by the SEMUCB-WM1 tomography model (French and Romanowicz, 2014), and the approach previously described in section 3, 'Methods'.

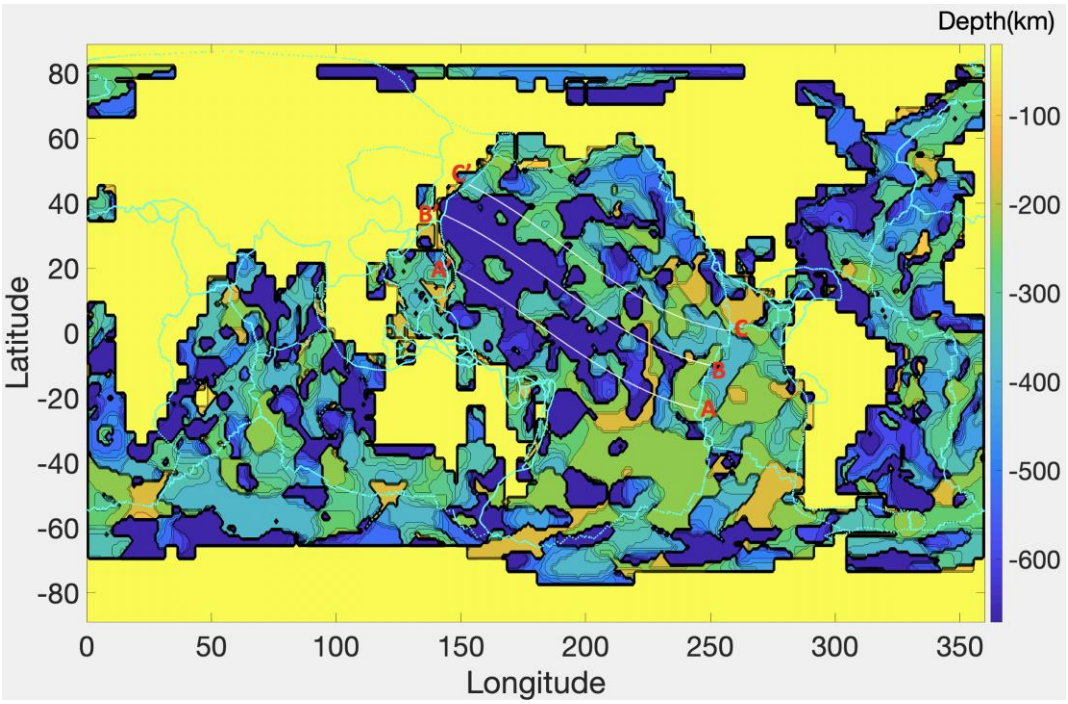


Figure 25 : Map of the base of the asthenosphere based on SEMUCB-WM1 tomography model (French and Romanowicz, 2014) obtained with the approach previously described. The cyan lines represent plate boundaries (Bird, 2003), such as mid-oceanic ridges and trenches. The white lines (AA', BB' and CC') represent the trajectory of present-day plate motion direction (taken from Adam et al., 2015) along which depth cross sections are investigated

In Figure 25, the depth to the base of the asthenosphere varies from about 200 km near the mid-oceanic ridge to more than 650 km far from the mid oceanic ridges. The depth cross section along the trajectories represented in Figure 25 are shown in Figure 26. Although our model does select the inflexion point after the maximal dvs has been reached in the asthenosphere, we do not consider that the red line represented in Figure 26 is actually representative of the base of the asthenosphere. Therefore, our characterization of this particular point is not successful. This can actually be seen by noticing that the depth of the base of the asthenosphere reaches 671 km in some regions.

Depth cross section showing the base of the asthenosphere along the trajectories represented in the Figure 25 are shown in the Figure 26.

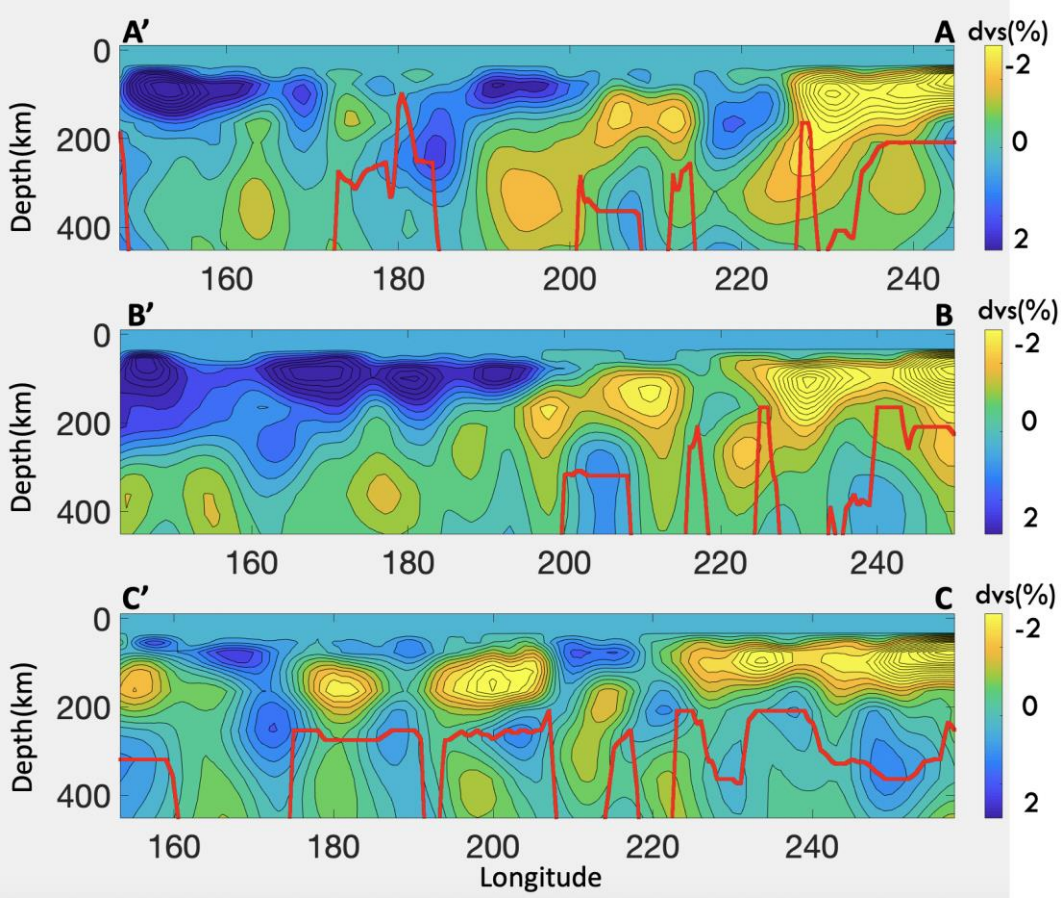


Figure 26 : Depth cross section along the trajectories represented in the Figure 25 for SEMUCB-WM1 tomography model (French and Romanowicz, 2014). The red line represents the base of the asthenosphere

The base of the asthenosphere (represented by red continuous line) could not be characterized well for SEMUCB-WM1 tomography model (French and Romanowicz, 2014). The depths to the base of the asthenosphere are very deep, deeper than 650 km in some regions. Our model correctly selects the inflexion point after the maximal dvs has been reached in the asthenosphere, when this inflexion point is "visible" in the tomography. So, the model correctly does what it was programmed to do. Some regions associated with lithospheric instabilities, like around longitude 175 $^{o}$E in CC' profile, longitude 185 $^{o}$E in AA' and around longitude 220 $^{o}$E in AA' profile are also associated with a deeper base of the asthenosphere. However, we do not think that this particular point is representative of a physical boundary. It will not be considered in the "Discussion" section.

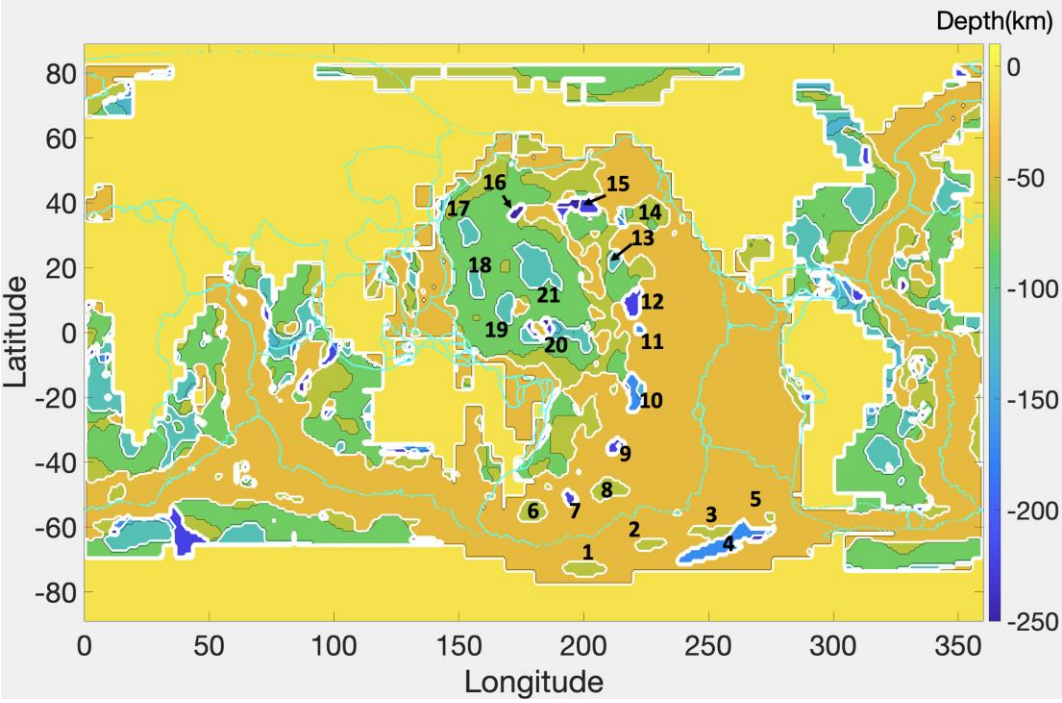


Figure 27 : Map of the middle of the lithosphere based on SEMUCB-WM1 tomography model (French and Romanowicz, 2014) and the contours of the lithospheric instabilities (obtained from the map of the middle of the lithosphere itself), in white. The white contours numbered 1 to 21 are regions with the anomalously deeper depth of the middle of the lithosphere than the surrounding regions. The green lines represent plate boundaries (Bird, 2003), such as mid-oceanic ridges and trenches

In Figure 27, the contours representing the locations of the anomalous lithospheric features obtained from the map of the middle of the lithosphere (Figure 27) are superimposed on the map of the middle of the lithosphere itself (Figure 27). The white contours numbered 1 to 21 are anomalous regions, i.e. regions with depths deeper than the surrounding regions.

These contours of the middle of the lithosphere are superimposed on the depths to base of the lithosphere, and to the middle of the asthenosphere, in Figure 28 and 29 respectively. These contours will also be reported on other figures in the following sections to investigate the correlation between the lithospheric anomalies derived from the SEMUCB-WM1 tomography model and other data and models.

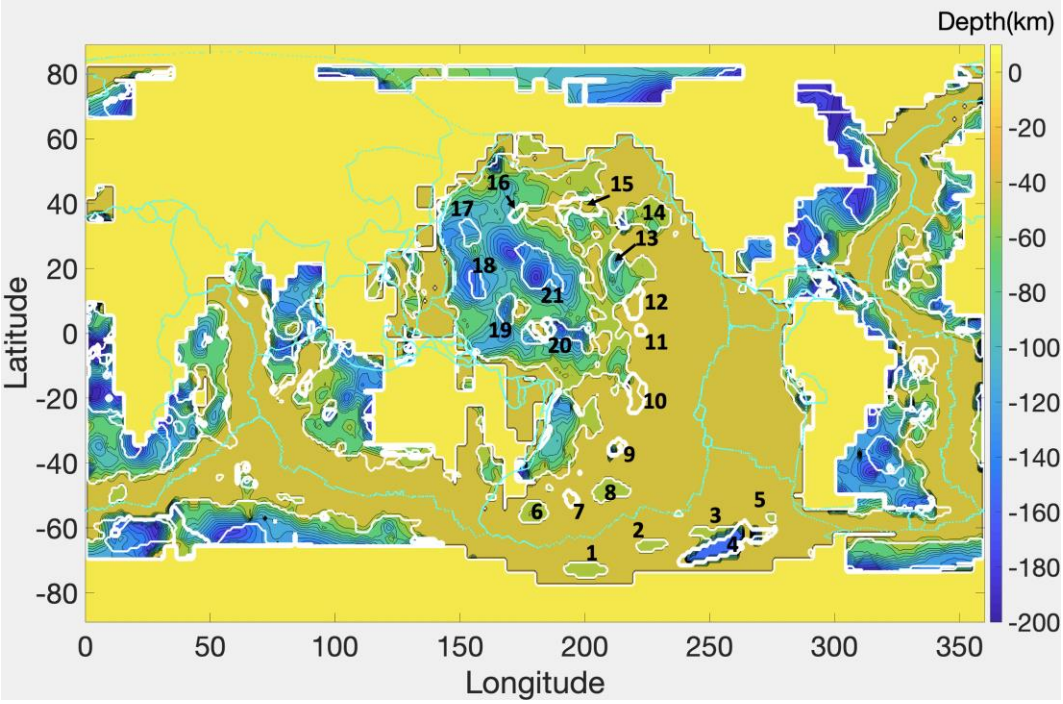


Figure 28 : Map of the base of the lithosphere based on SEMUCB-WM1 tomography model (French and Romanowicz, 2014) and the contours of the lithospheric instabilities (obtained from the map of the middle of the lithosphere based on SEMUCB-WM1 tomography model), in white. The white contours numbered 1 to 21 are regions with the anomalously deeper depth of the middle of the lithosphere than the surrounding regions. The green lines represent plate boundaries (Bird, 2003), such as mid-oceanic ridges and trenches

In Figure 28, we observe that the contours of the middle of the lithosphere correlate with the anomalies observed in the map of the base of the lithosphere.

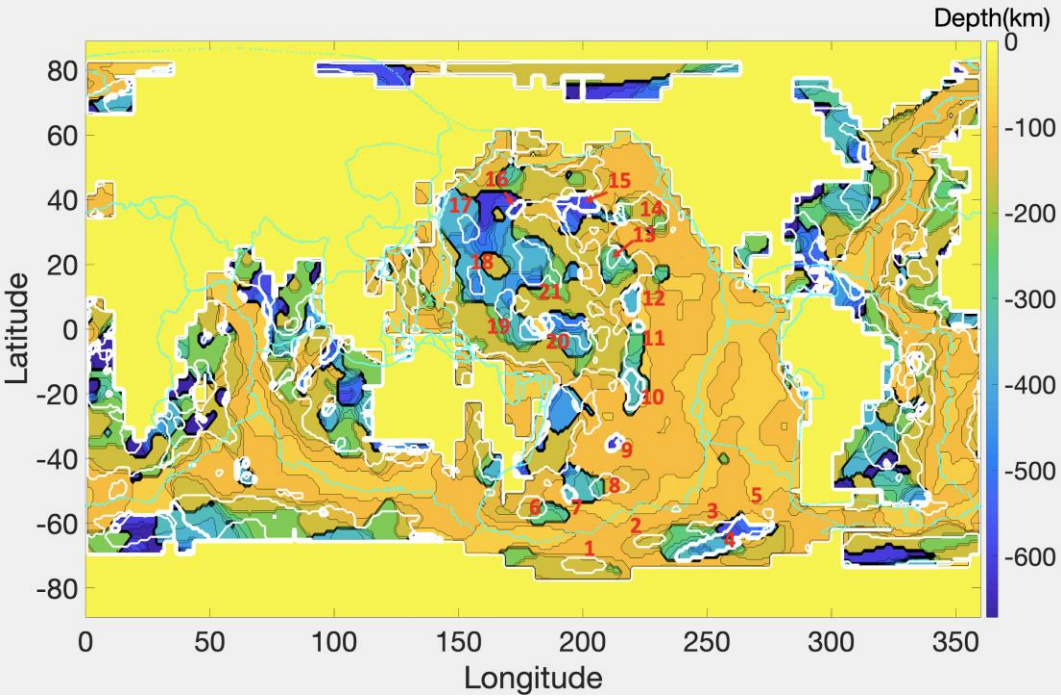


Figure 29 : Map of the middle of the asthenosphere based on SEMUCB-WM1 tomography model (French and Romanowicz, 2014) and the contours of the lithospheric instabilities (obtained from the map of the middle of the lithosphere based on SEMUCB-WM1 tomography model), in white. The white contours numbered 1 to 21 are regions with the anomalously deeper depth of the middle of the lithosphere than the surrounding regions. The green lines represent plate boundaries (Bird, 2003), such as mid-oceanic ridges and trenches

In Figure 29, we observe that the contours of the middle of the lithosphere correlate with the anomalies observed in the map of the middle of the asthenosphere. However, supplementary anomalies are found in the map of the middle of the asthenosphere, like in the regions around longitude 200 $^{o}$E and latitude 50 $^{o}$S, or around longitude 220 $^{o}$E and latitude 10 $^{o}$S, and around longitude 170 $^{o}$E and latitude 47 $^{o}$N.

In summary, we observe a good correlation between the patterns evidenced in the three maps obtained in this study i) map of the middle of the lithosphere's depth (Figure 27) ii) map of the base of the lithosphere (Figure 28) and iii) map of the middle of the asthenosphere's depth (Figure 29). Previously, in Figure 24, we observed that the deepening of the lithosphere was followed by the deepening of the asthenosphere as well. This observation is corroborated by the comparisons made in Figures 27, 28 and 29.

## 4.2 Characteristics of the lithosphere and asthenosphere from other tomography model

The methods described previously have been applied to other tomography models- i) SAVANI (Auer et al., 2014) and ii) S40RTS (Ritsema et al., 2011), to study lithosphere and asthenosphere characteristics. The method used to select the middle of the lithosphere and the asthenosphere has not been significantly modified to implement the other tomography models. The determination of the base of the lithosphere requires an ad hoc hypothesis on the isovalues describing the base. As discussed earlier, the amplitude of dvs varies with the tomography models. As this isovalue is a parameter of our model, we discuss the choice of this parameter for the SAVANI (Auer et al., 2014) and S40RTS (Ritsema et al., 2011) model in Appendix A. Here, we display only the final map for the base of the lithosphere. Similar to SEMUCB-WM1 tomography model (French and Romanowicz, 2014), the base of the asthenosphere could not be determined for SAVANI (Auer et al., 2014) and S40RTS (Ritsema et al., 2011) as well. Therefore, it will not be discussed further.

### 4.2.1 SAVANI

The maps showing the middle of the lithosphere is displayed in Figures 30. It has been obtained by considering the dvs provided by the SAVANI tomography model (Auer et al., 2014), and the approach previously described in section 3, 'Methods'.

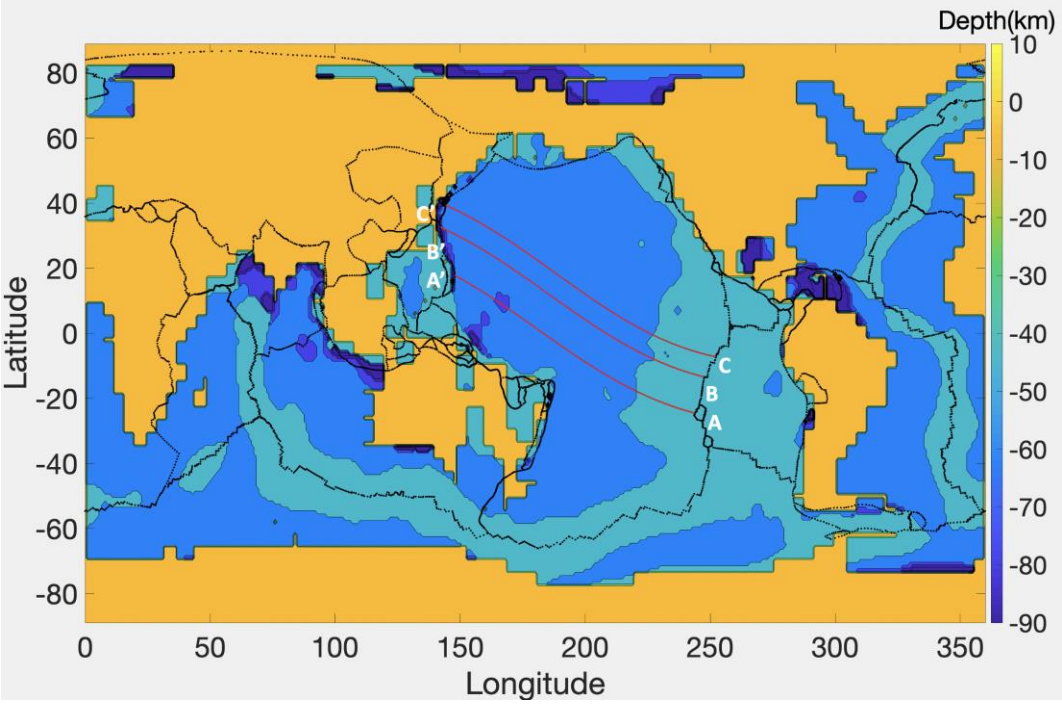


Figure 30 : Map of the middle of the lithosphere based on SAVANI tomography model (Auer et al., 2014) obtained with approach previously described. The black lines represent plate boundaries (Bird, 2003), such as mid-oceanic ridges and trenches. The red lines (AA', BB' and CC') represent the trajectory of present-day plate motion direction (taken from Adam et al., 2015) along which depth cross sections are investigated

There are no clear anomalies evidenced from the map showing the middle of the lithosphere (Figure 30) obtained from the SAVANI tomography model (Auer et al., 2014).

The map showing the base of the lithosphere is displayed in Figures 31. It has been obtained by applying same method as applied for SEMUCB-WM1 tomography model (French and Romanowicz, 2014) (see Appendix A for details).

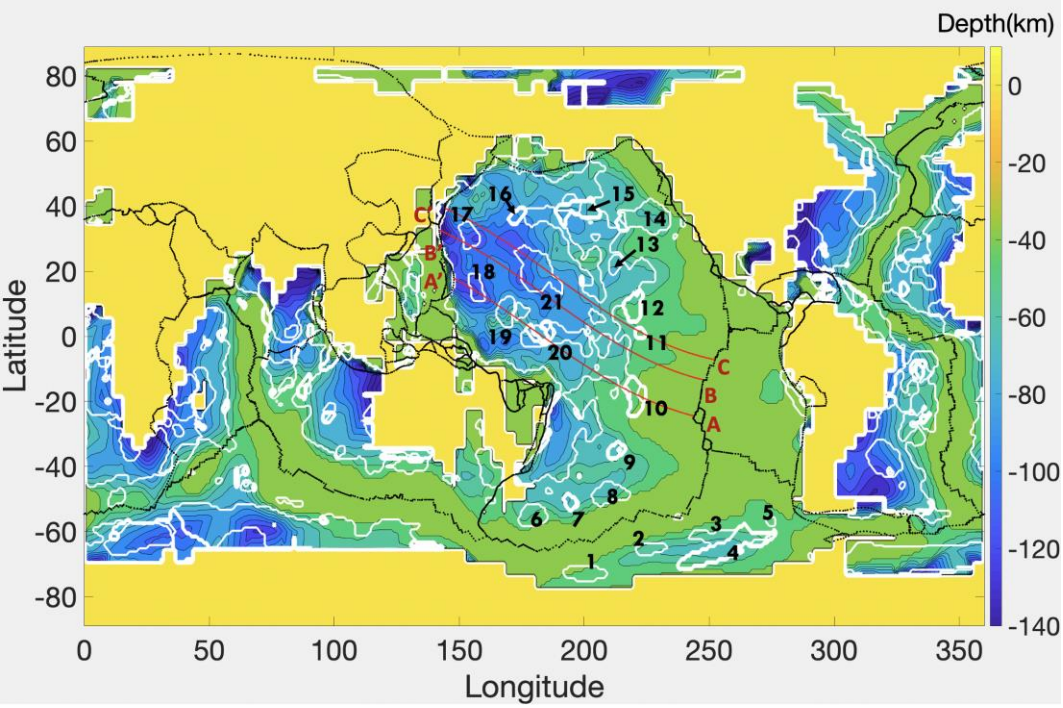


Figure 31 : Map of the base of the lithosphere based on SAVANI tomography model (Auer et al., 2014) and the contours of the lithospheric instabilities (obtained from the map of the middle of the lithosphere from SEMUCB-WM1 tomography model), in white. The white contours numbered 1 to 21 are regions with the anomalously deeper depth of the middle of the lithosphere than the surrounding regions. The black lines represent plate boundaries (Bird, 2003), such as mid-oceanic ridges and trenches. The red lines (AA', BB' and CC') represent the trajectory of present-day plate motion direction (taken from Adam et al., 2015) along which depth cross sections are investigated

There is a fair correlation between the base of the lithosphere derived from the SAVANI model (Figure 31) and the lithospheric anomalies derived from the SEMUCB-WM1 tomography model. The anomalies in the depth to the base of the lithosphere in the older parts of the Pacific plate, in the northwestern regions, or on the Antarctic plate are observed from both tomography models. This correspondence in the location of anomalies using different data sets provides some reassurance that the features observed are not simply artifacts of the different tomography models.

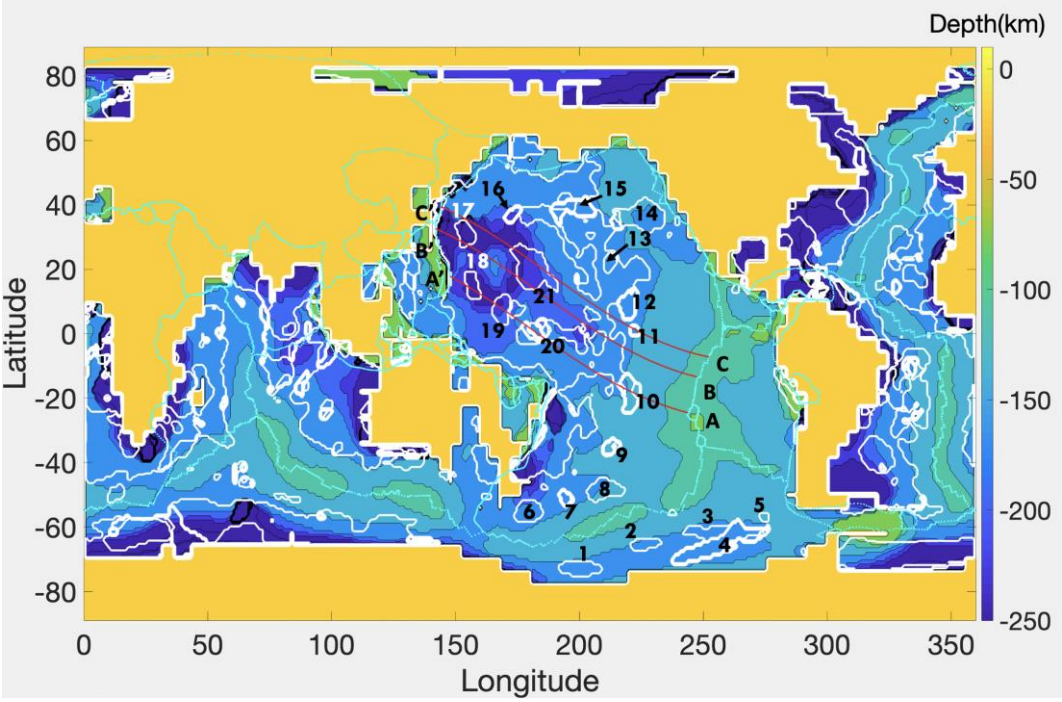


Figure 32 : Map of the middle of the asthenosphere based on SAVANI tomography model (Auer et al., 2014) and the contours of the lithospheric instabilities (obtained from the map of the middle of the lithosphere from SEMUCB-WM1 tomography model), in white. The white contours numbered 1 to 21 are regions with the anomalously deeper depth of the middle of the lithosphere than the surrounding regions. The cyan lines represent plate boundaries (Bird, 2003), such as mid-oceanic ridges and trenches. The red lines (AA', BB' and CC') represent the trajectory of present-day plate motion direction (taken from Adam et al., 2015) along which depth cross sections are investigated

The map showing the middle of the asthenosphere determined from the SAVANI tomography models is displayed in Figures 32. These anomalous regions identified in Figure 32 correlate with the lithospheric anomalies derived from the SEMUCB-WM1 tomography model. Contours 6,7, 8, 14 and 16-21 correlate indeed with the anomalies recovered from the middle of the asthenosphere's depth. Contours 1-4 also correlate with the anomalies apparent on the Antarctic plate.

Depth cross sections of the SAVANI tomography model along the trajectories represented in Figures 30, 31 and 32 are displayed in Figure 33. These depth cross sections show that our model recovers the particular points such as middle of the lithosphere, base of the lithosphere and the middle of the asthenosphere.

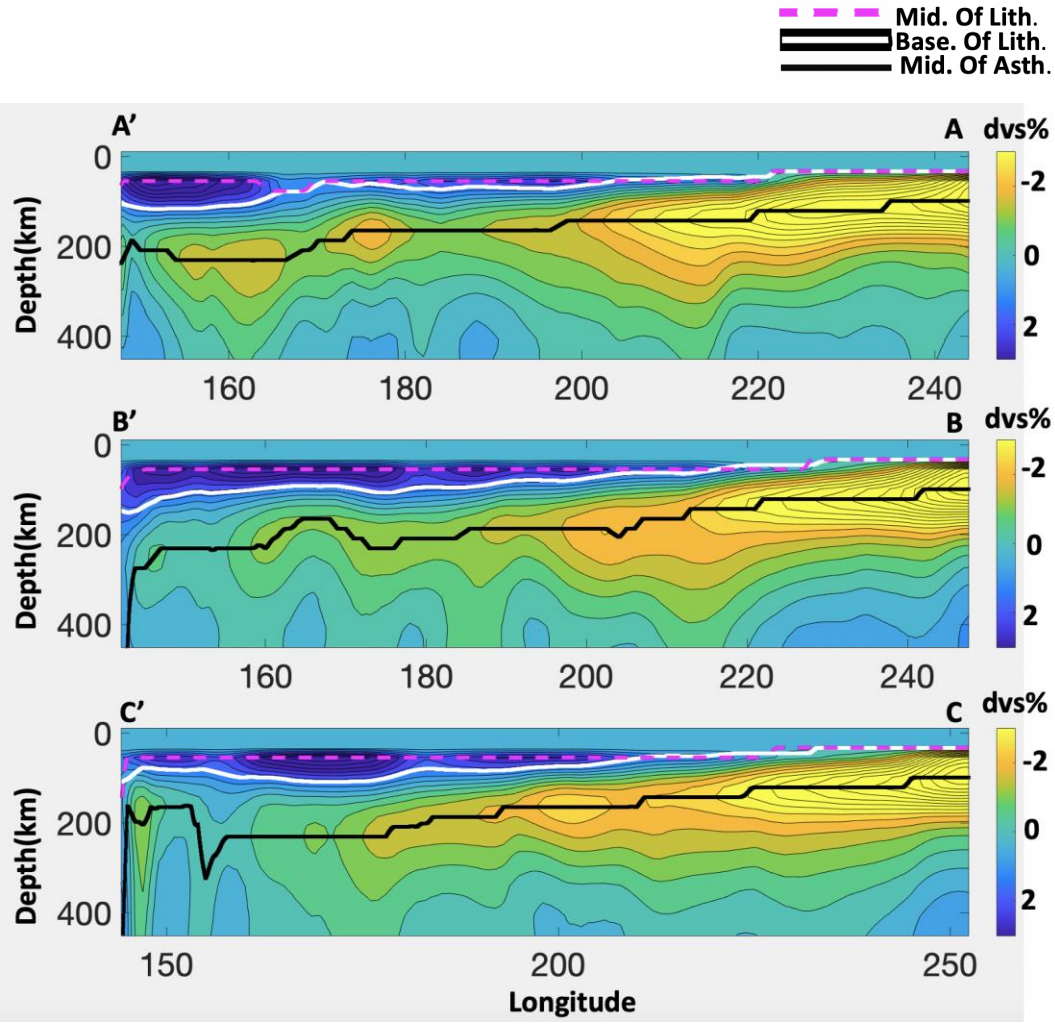


Figure 33 : Depth cross section along the trajectories represented in Figures 30, 31 and 32 for the SAVANI tomography model (Auer et al., 2014). The black line represents the middle of the asthenosphere, the white continuous line represents the base of the lithosphere obtained by tracking the dvs 1.5% isovalue and the dashed magenta line represents the middle of the lithosphere

In Figure 33 we observe the gradual increase in the depth to the base of the lithosphere (represented by the white continuous line) moving away from the mid-oceanic ridges (areas near A, B and C). A similar increase is observed in the depth to the middle of the asthenosphere (reported by the black continuous line).

### 4.2.2 S40RTS

The map showing the middle of the lithosphere obtained by considering the dvs provided by the S40RTS tomography model (Ritsema et al., 2011) is displayed in Figures 34. There are no clear anomalies.

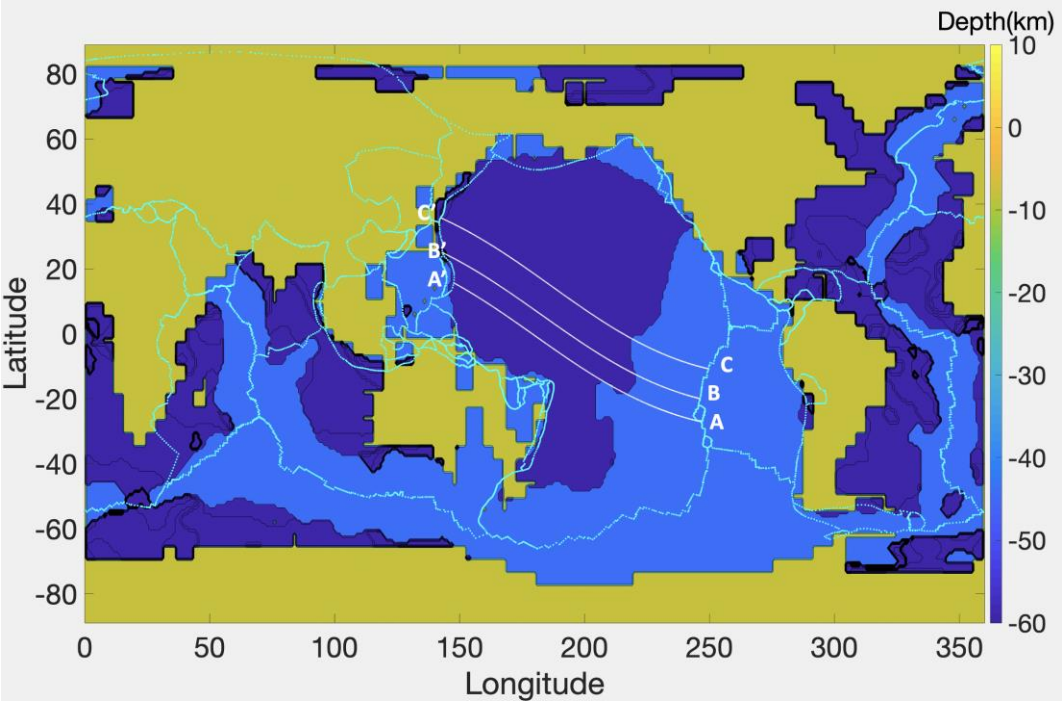


Figure 34 : Map of the middle of the lithosphere based on S40RTS tomography model (Ritsema et al., 2011) obtained with approach previously described. The cyan lines represent plate boundaries (Bird, 2003), such as mid-oceanic ridges and trenches. The white lines (AA', BB' and CC') represent the trajectory of present-day plate motion direction (taken from Adam et al., 2015) along which depth cross sections are investigated

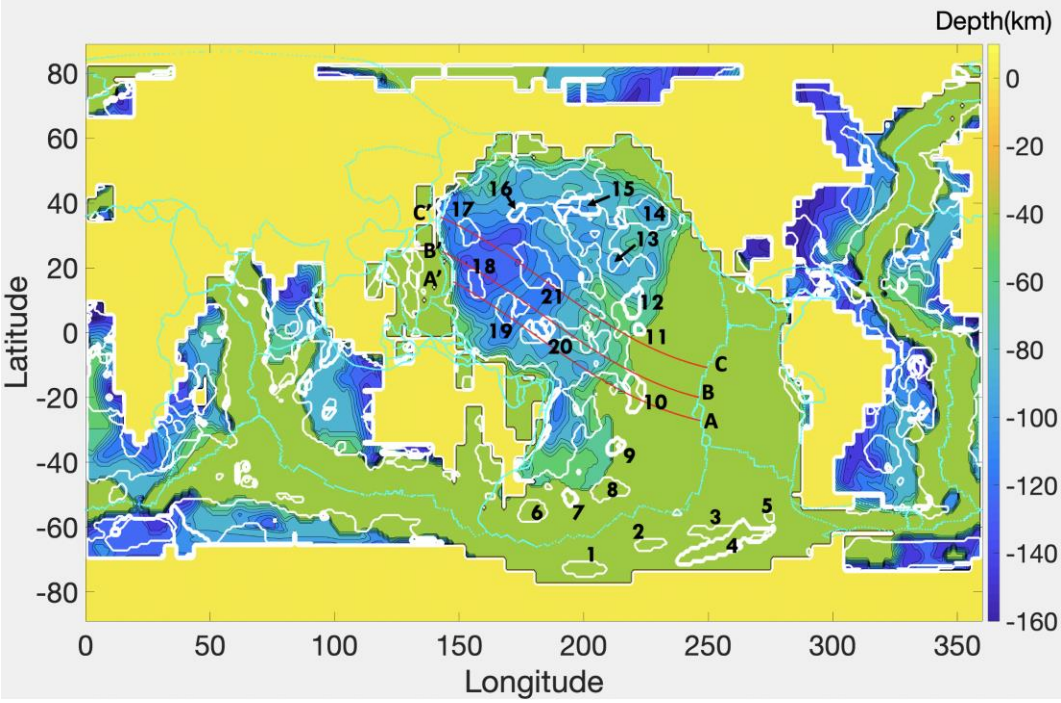


Figure 35 : Map of the base of the lithosphere based on S40RTS tomography model (Ritsema et al., 2011) and the contours of the lithospheric instabilities (obtained from the map of the middle of the lithosphere from SEMUCB-WM1 tomography model), in white. The white contours numbered 1 to 21 are regions with the anomalously deeper depth of the middle of the lithosphere than the surrounding regions. The cyan lines represent plate boundaries (Bird, 2003), such as mid-oceanic ridges and trenches. The red lines (AA', BB' and CC') represent the trajectory of present-day plate motion direction (taken from Adam et al., 2015) along which depth cross sections are investigated

The map showing the base of the lithosphere obtained by considering the dvs provided by S40RTS tomography model (Ritsema et al., 2011) is displayed in Figures 35. It has been obtained by applying same method as applied for SEMUCB-WM1 tomography model (French and Romanowicz, 2014) (see Appendix A for details). We can see several anomalies in the northwest of the Pacific plate. There is a no correlation however between the base of the lithosphere derived from the S40RTS model (color map in Figure 35) and the lithospheric anomalies derived from the SEMUCB-WM1 tomography model (white contours in Figure 35). The contours 14,17, 18, 19 and 21 are located over the deeper anomalies, but the patterns are not similar. It almost seems like the S40RTS model is the product of a low-pass filter applied to the SEMUCB-WM1 tomography model. This is consistent with the fact that the S40RTS model is an older and less resolved model. However, the rough locations of the lithospheric anomalies on the northwestern part of the Pacific plate are reproduced with the S40RTS tomography model.

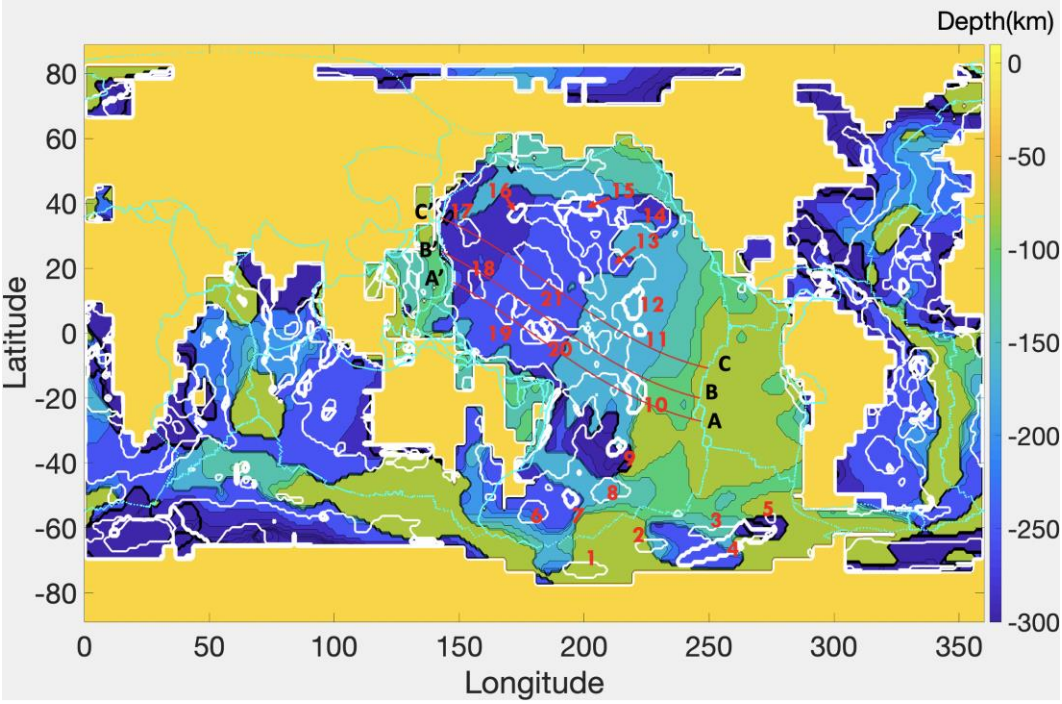


Figure 36 : Map of the middle of the asthenosphere based on S40RTS tomography model (Ritsema et al., 2011) and the contours of the lithospheric instabilities (obtained from the map of the middle of the lithosphere from SEMUCB-WM1 tomography model), in white. The white contours numbered 1 to 21 are regions with the anomalously deeper depth of the middle of the lithosphere than the surrounding regions. The cyan lines represent plate boundaries (Bird, 2003), such as mid-oceanic ridges and trenches. The red lines (AA', BB' and CC') represent the trajectory of present-day plate motion direction (taken from Adam et al., 2015) along which depth cross sections are investigated

The map showing the middle of the asthenosphere is displayed in Figures 36. We see a smooth increase of this depth in the northwestern part of the Pacific plate, and some anomalous regions in the middle of the Pacific plate between latitudes 20°S and 40°S. These anomalous regions did not appear in the other tomography models. There are some other anomalies on the Antarctic plate. In general, the observed anomalies do not correlate well with the contours derived from the SEMUCB-WM1 tomography. This can be explained by the fact that the S40RTS model is older and less resolved than the SEMUCB-WM1 and SAVANI models.

Depth cross sections of the S40RTS tomography model (Ritsema et al., 2011) along the trajectories represented in Figures 34, 35 and 36 are displayed in Figure 37. These depth cross sections show that our model recovers the particular points such as middle of the lithosphere, base of the lithosphere and the middle of the asthenosphere.

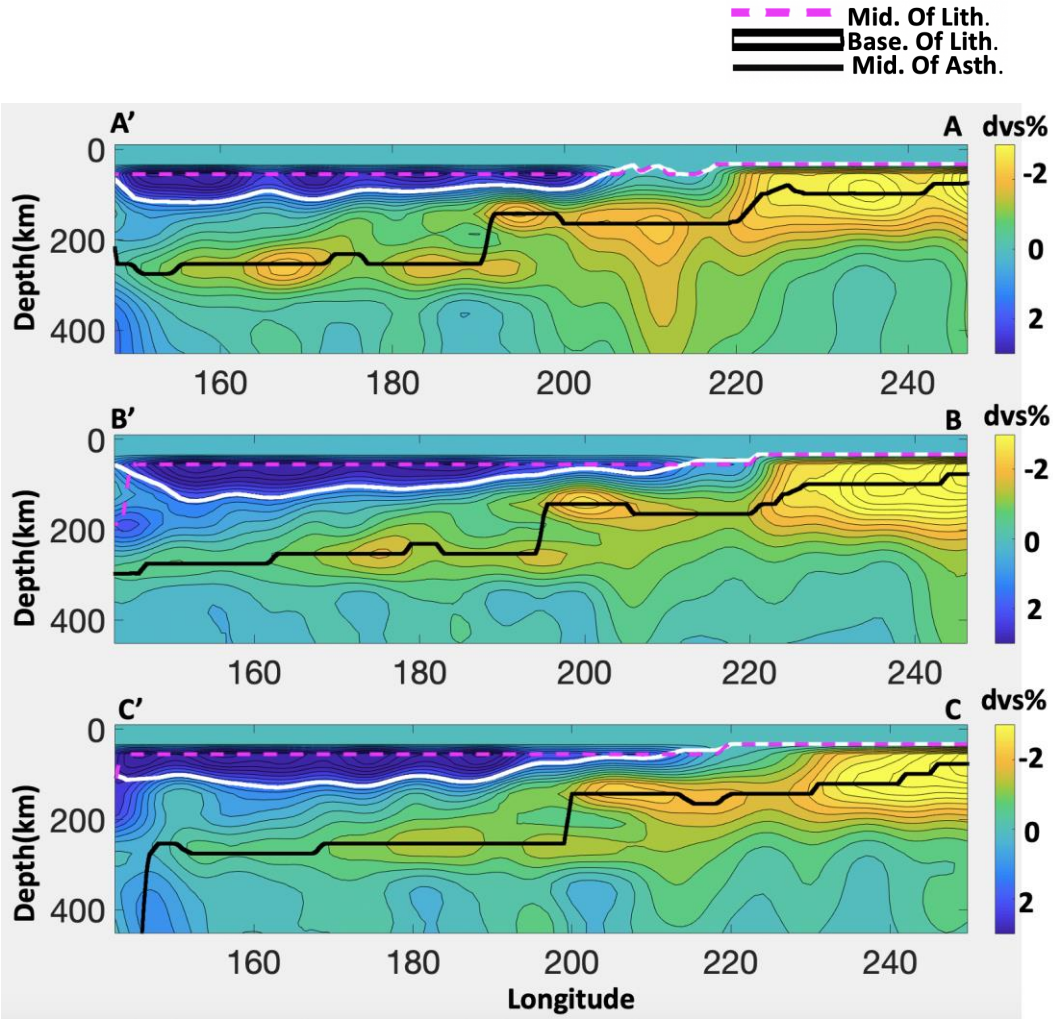


Figure 37 : Depth cross section along the trajectories represented in Figures 34, 35 and 36 for the S40RTS tomography model (Ritsema et al., 2011). The black line represents the middle of the asthenosphere, the white continuous line represents the base of the lithosphere obtained by tracking the dvs 1.5% isovalue and the dashed magenta line represents the middle of the lithosphere

In Figure 37, we observe the gradual increase in the depth of the base of the lithosphere (reported by the white continuous line) moving away from the mid-oceanic ridges (areas near A, B and C). A similar increase is observed for the depth of the middle of the asthenosphere (represented by black continuous line). But in this case, the variations of the base of the lithosphere are not accompanied by variations of the middle of the asthenosphere, as it was for the other tomography models.

To summarize, we use the highly resolved SEMUCB-WM1 tomography model (French and Romanowicz, 2014) to determine regions associated with lithospheric anomalies, i.e. regions associated with a thicker lithosphere when compared to the regions around them. The SEMUCB-WM1 tomography model has been chosen as a reference model, because of the innovative method implemented for the seismic data inversion. Even if the SAVANI tomography model (Auer et al., 2014) is more recent, the scientific community recognize SEMUCB-WM1 as one of the best tomography models. We compared the lithospheric instabilities derived from SEMUCB-WM1 tomography with the lithospheric instabilities derived from the SAVANI (Auer et al., 2014) and S40RTS (Ritsema et al., 2011) tomography models. The correlation between the results obtained from the SEMUCB-WM1 and SAVANI models is good. This in encouraging, considering that these models use different data sets and inversion methods. This means that our characterization of the lithospheric anomalies is robust. The correlation is less good when considering the S40RTS tomography. This is not surprising considering that S40RTS model is an older and less resolved model. In the following, we compare the lithospheric anomalies derived from the SEMUCB-WM1 tomography with other geophysical data and model.

## 4.3 Comparison of lithospheric anomalies and geoid anomalies

To investigate the correlation between geoid and lithospheric anomalies, we have filtered the geoid for different order and degree ranges. One of the difficulties in this process is to know which are the orders representative of the physical phenomenon we aim to investigate. However, the morphology of the lithospheric anomalies from the tomography models can provide some constraints on this. The lithospheric anomalies identified by the tomography models are roughly 5,000 km long and 1,000 km wide. Considering that the circumference of the Earth is 40,075 km, these wavelengths correspond to ~degrees 8 (~40,075/5,000) and 40 (~40,075/1,000).

We have then investigated how the geoid anomalies, obtained by filtering the geoid for order and degrees ranges around the l=8-40 correlate with the lithospheric anomalies we have identified from the SEMUCB-WM1 tomography model.

The EGM2008 geoid (Pavlis et al., 2012) has been used in this study. In Figure 38, we display the geoid anomalies filtered for several order and degree ranges: l= 2-31, 6-40 and l=8-40. The white lines are the contours of the lithospheric anomalies obtained from the SEMUCB-WM1 tomography model (French and Romanowicz, 2014). The l=2-31 geoid anomaly, encompassing the signals of most of the geodynamical processes, is also reported for comparison.

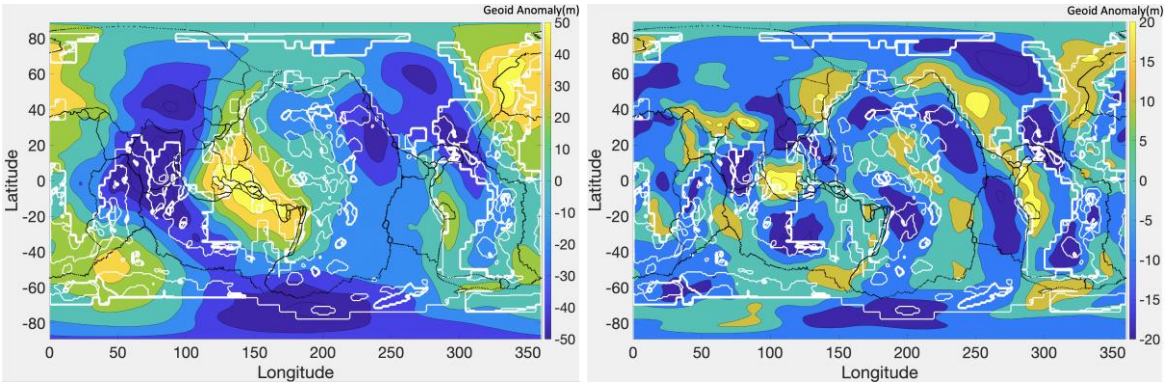


(a) (b)

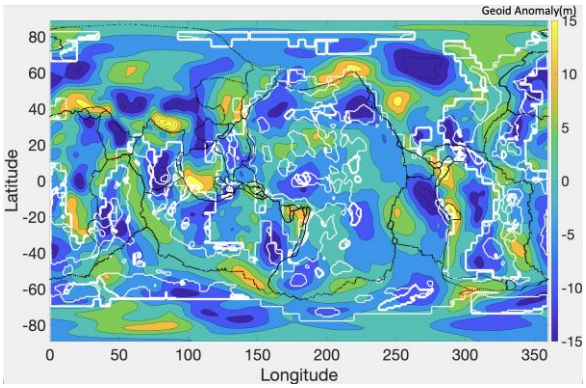


(c)

Figure 38 : Observed geoid for (a) l=2-31, (b) l=6-40 and (c) l=8-40 from the EGM2008 model (Pavlis et al., 2012) and the contours of the lithospheric anomalies obtained from the SEMUCB-WM1 tomography model (French and Romanowicz, 2014), in white. The black lines represent plate boundaries (Bird, 2003), such as mid-oceanic ridges and trenches

The lithospheric anomalies characterized from the tomography models do not correlate with the l=2-31, and l=6-40 geoid anomalies. The l=8-40 degrees range has been constrained from the morphology of the lithospheric anomalies. For this degree range, the lithospheric anomalies

are correlated with negative geoid anomalies. This is true almost everywhere, at the exception of the region near Hawaii, near longitude 200°E, and latitude 20°N. In this region, the geoid probably includes the signature of the deep Hawaii plume.

The geoid anomaly at the surface can be computed through equation 2 (Hager and Clayton, 1989).

$$\delta N^{nm} = \sum_{n=n_{min}}^{n_{max}} \sum_{m=0}^{n} \left\{ \frac{4\pi G}{g(2n+1)} \left[ \int_{r_c}^{r_s} \delta\rho^{nm}(r)\, r \left(\frac{r}{r_s}\right)^{n+1} dr + \Delta\rho_s \delta h_s^{nm}\, r_s + \Delta\rho_s\, \delta h_c^{nm}\, r_c \left(\frac{r_c}{r_s}\right)^{n+1} \right] \right\}$$

(equation 2)

where G is the gravitational constant, $r_s$ is the Earth's radius, $r_c$ is the core radius, n and m are the spherical harmonic degree and order, and $n_{min}$ and $n_{max}$ are the minimum and maximum degrees. The geoid anomaly is computed through the spherical harmonic expansions, by integrating the density anomalies from the core to the surface ($r_c \leq r \leq r_s$) (first term), and considering the geoid anomalies produced by the dynamic topographies at the top surface and at the CMB (second and third terms).

Internal density anomalies would create a positive geoid anomaly, as in regions of lithospheric anomalies appear to have extra mass. As discussed below, we interpret the extra mass as lithospheric drips. These lithospheric drips create a downwelling flow, associated with a negative dynamic topography at the surface. The effect of the CMB dynamic topography is generally negligible.

## 4.4 Comparison between the lithosphere anomalies identified from tomography and other geophysical data

### 4.4.1 Investigation of the correlation between the lithosphere anomalies and plate kinematics

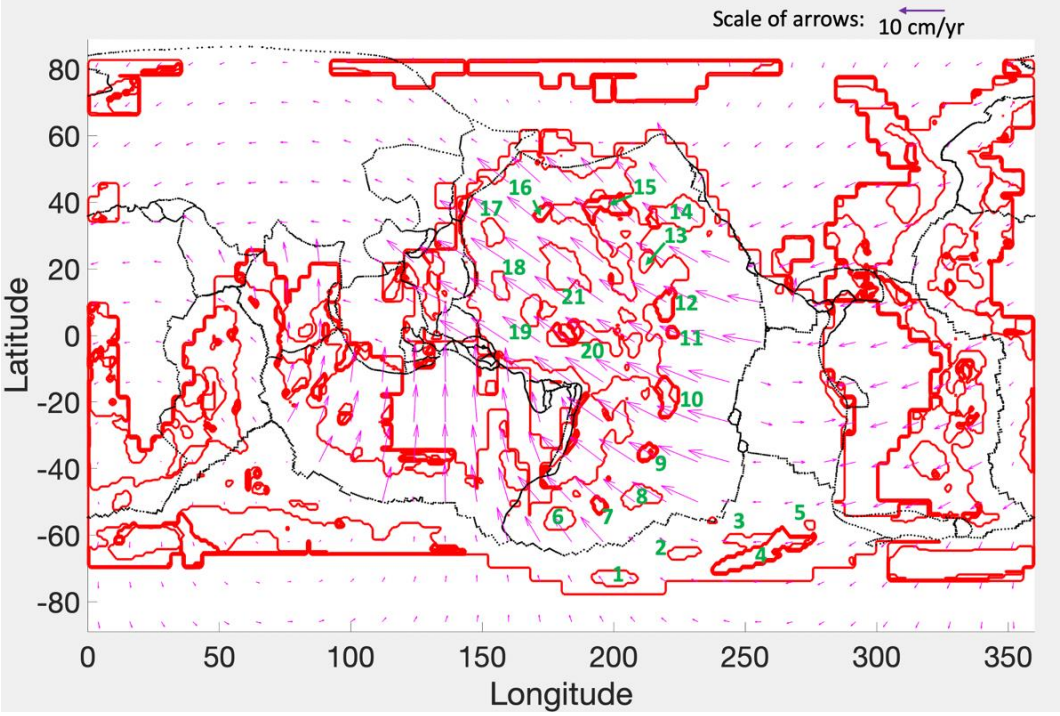


Figure 39 : Map showing the kinematic velocities of the plate and the contours of lithospheric instabilities (denoted by 1 to 21) obtained from the SEMUCB-WM1 tomography model (French and Romanowicz, 2014), reported by the red lines. The black lines represent plate boundaries (Bird, 2003), such as mid-oceanic ridges and trenches. The magenta arrows represent the kinematic velocities of the lithospheric plates computed from the Nuvel1A model, in the HS3 reference frame (Gripp and Gordon, 2002)

The kinematic velocities and the contours of lithospheric anomalies, described in the previous section and obtained from the SEMUCB-WM1 tomography model (French and Romanowicz, 2014), are shown in Figure 39. The kinematic velocities have been computed from the Nuvel1A model, in the HS3 reference frame (Gripp and Gordon, 2002). Lithospheric anomalies could not be determined near the mid-oceanic ridges, where the tomography models show a broad seismically slow region. West of the mid-oceanic ridges, almost in the middle of the Pacific plate, anomalous regions where the thickness of the lithosphere is about 80 km appear. They

form almost a continuous band, perpendicular to the motion of the Pacific plate (anomalies 6 to 14). Farther north-west, longer discontinuous lithospheric anomalies, nearly parallel to the plate motion direction can be observed. Near the Pacific-Antarctic Ridge (PAR), four-anomalies (numbered 1, 2, 6, and 8) are almost symmetrically distributed relatively to the PAR. Two of them (anomalies 6 and 8) are on the Pacific plate and two others (anomalies 1 and 2) on the Antarctic plate. As these anomalies are almost circular, it is difficult to correlate them with the kinematic velocities.

### 4.4.2 Investigation of the correlation between the lithosphere anomalies and seafloor age

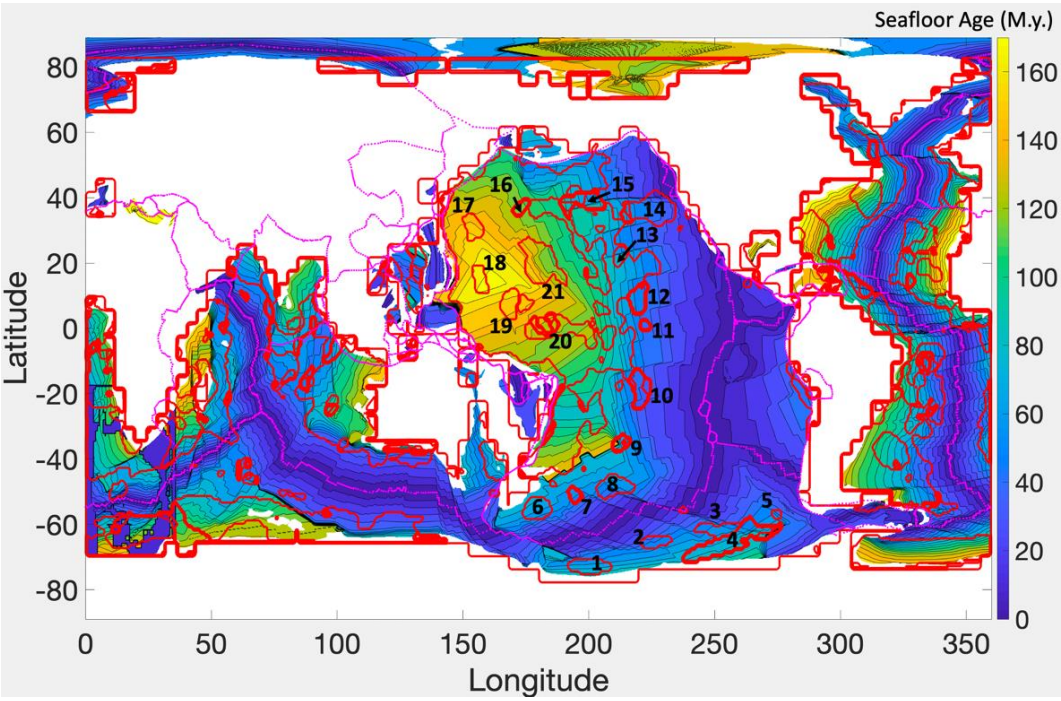


Figure 40 : Maps showing the age of the seafloor age (data from Müller et al., 1997) and the contours outlining lithospheric anomalies (denoted by 1 to 21) obtained from the SEMUCB-WM1 tomography model (French and Romanowicz, 2014) reported by the red lines. The magenta lines represent plate boundaries (Bird, 2003), such as mid-oceanic ridges and trenches

The age of the seafloor (data from Müller et al., 1997) and contours of lithospheric anomalies are displayed in Figure 40. Lithospheric anomalies appearing near the mid-oceanic ridges are numbered from 1-14. The age of the seafloor along which some of these anomalies are

emplaced is reported in Table 1. This indicates that the onset of lithospheric discontinuities occurs on seafloor with ages varying between 30 to 40 M.y., or at least this is when they can be first identified from the tomography data. Farther northwest, longer discontinuous lithospheric anomalies, elongate parallel to the plate motion direction, are observed. These longer lithospheric anomalies appear on seafloor with ages between 105 and 112 M.y., but they are observed all along the oldest seafloor.

Table 1 : Table showing the anomalies presented in the study and their corresponding age of seafloor (minimum and maximum)

| Anomalies | Age of Seafloor (M.y.) | |
|---|---|---|
| | Minimum | Maximum |
| 1 | 34.95 | 87.79 |
| 2 | 30.68 | 62.51 |
| 6 | 38.6 | 79.61 |
| 8 | 30.02 | 72.6 |
| 10 | 31.76 | 51.77 |
| 11 | 41.52 | 52.89 |
| 12 | 45.69 | 67.15 |
| 14 | 26 | 71.26 |

### 4.4.3 Investigation of the correlation between the lithosphere anomalies and the theoretical thickness of the lithosphere

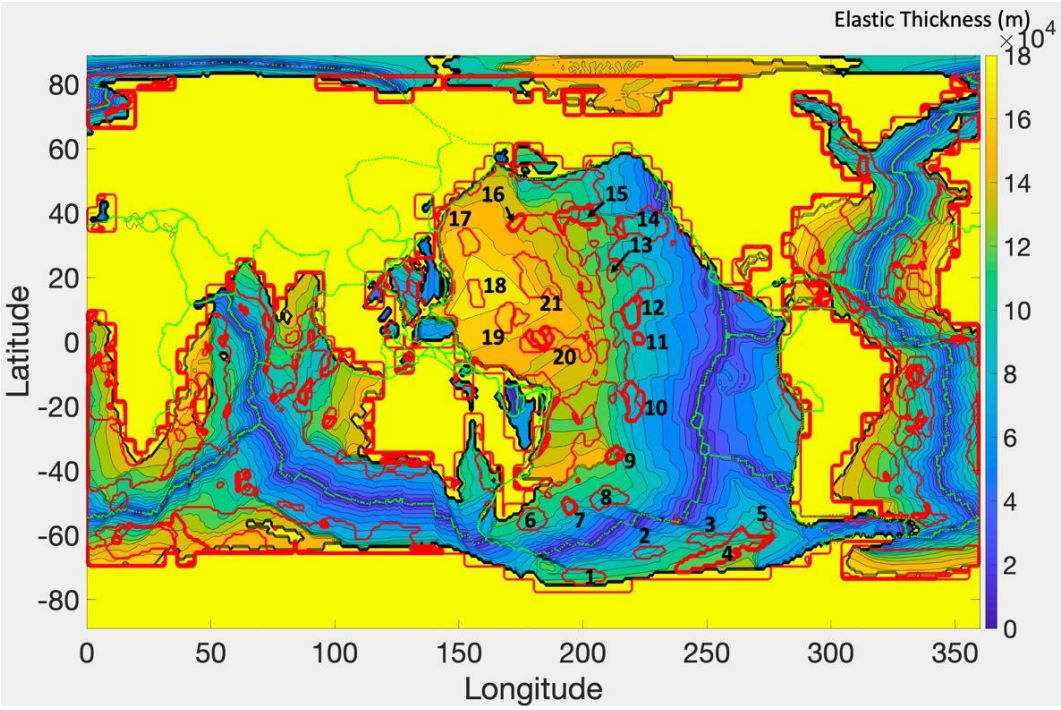


Figure 41 : Maps showing the elastic thickness of the lithosphere, computed from the GDH1 model of Stein and Stein (1992) by C. Adam and the contours of the lithospheric anomalies (denoted by 1 to 21), in red. The green lines represent plate boundaries (Bird, 2003), such as mid-oceanic ridges and trenches

The elastic thickness of the lithosphere, computed from the GDH1 model (Stein and Stein, 1992) by supervisor Adam is displayed in Figure 41, along with the contours of the lithospheric anomalies. Lithospheric anomalies near the mid-oceanic ridges are numbered 1 to 14. The ranges of elastic thicknesses of the lithosphere associated with some of these lithospheric anomalies are listed in Table 2. The onset of lithospheric anomalies seems to occur on seafloor with lithospheric thickness of 75-90 km. The lowest elastic thicknesses of the lithosphere along which longer lithospheric anomalies appear are in the range 138 - 142 km. These longer anomalies exist on seafloor with an elastic thickness varying between 138 and 180 km.

Table 2 : Table showing the anomalies presented in the study and their corresponding elastic thickness (minimum and maximum) of the lithosphere where they occur

| Anomalies | Elastic Thickness of Lithosphere(km) | |
|---|---|---|
| | Minimum | Maximum |
| 1 | 78 | 124.5 |
| 2 | 74.3 | 105.1 |
| 6 | 83.99 | 119.6 |
| 8 | 74.2 | 113.4 |
| 10 | 75.4 | 96.4 |
| 11 | 85.9 | 97.4 |
| 12 | 92.2 | 109 |
| 14 | 36.3 | 110 |

### 4.4.4 Investigation of the correlation between the lithosphere anomalies and the distance from mid-oceanic ridges, considering the present-day mantle dynamics

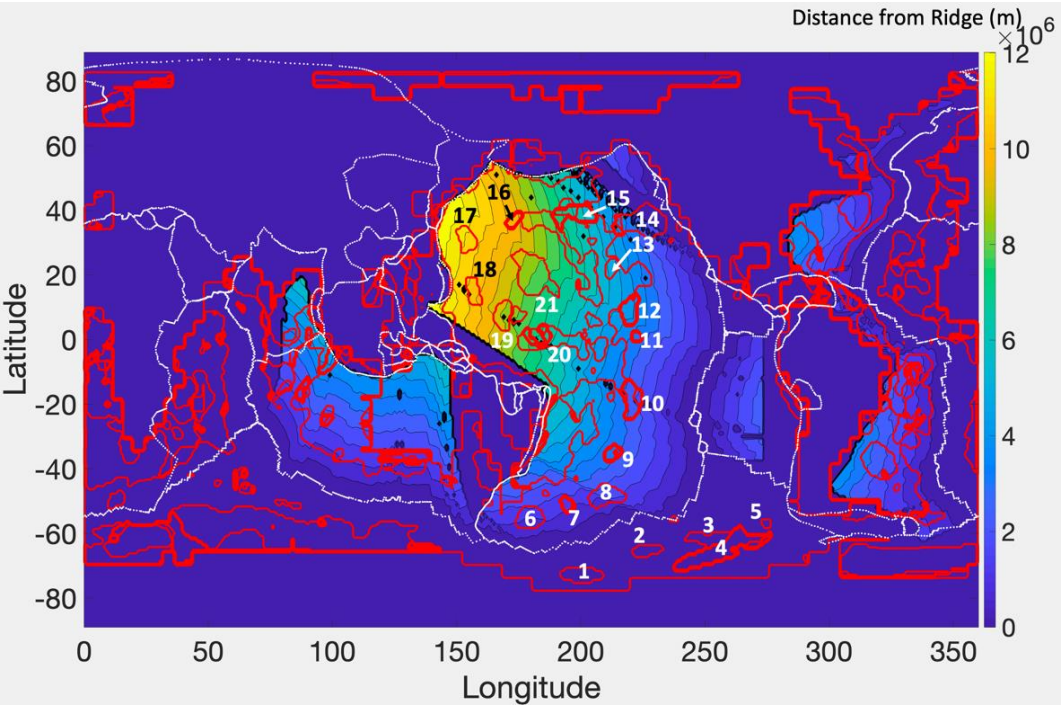


Figure 42 : Distance from the mid-oceanic ridges and contours of the lithospheric anomalies (denoted by numbers from 1 to 21), reported in red. The white lines represent plate boundaries (Bird, 2003), such as mid-oceanic ridges and trenches

The distance from the mid-ocean ridge (Figure 42) is computed by considering the present-day motion of the lithospheric plates. It has been obtained by my supervisor, C. Adam, using the Nuvel1A model, in the HS3 reference frame (Gripp and Gordon, 2002). Lithospheric anomalies near the mid-oceanic ridges are numbered 1 to 14. The range of distances between the mid-oceanic ridge and some of these lithospheric anomalies are displayed in table 3, and vary from 656 km to 3,778 km. The distances between the ridge and longer lithospheric anomalies 21 and 20 are 6730 km and 4976 km, respectively. There seems to be no direct correlation between the locations of lithospheric anomalies and distance from the mid-oceanic ridge.

Table 3 : Table showing the anomalies presented in the study and their corresponding distance (minimum and maximum) from the ridge

| Anomalies | Distance From Mid-Oceanic Ridges(km) | |
|---|---|---|
| | Minimum | Maximum |
| 1 | N/A | N/A |
| 2 | N/A | N/A |
| 6 | 893.2 | 2078 |
| 8 | 656.8 | 2692 |
| 10 | 2099 | 3061 |
| 11 | 3133 | 3733 |
| 12 | 3778 | 4829 |
| 14 | N/A | 4655 |

### 4.4.5 Investigation of the correlation between the lithosphere anomalies and bathymetric features, such as hotspots or oceanic plateaus

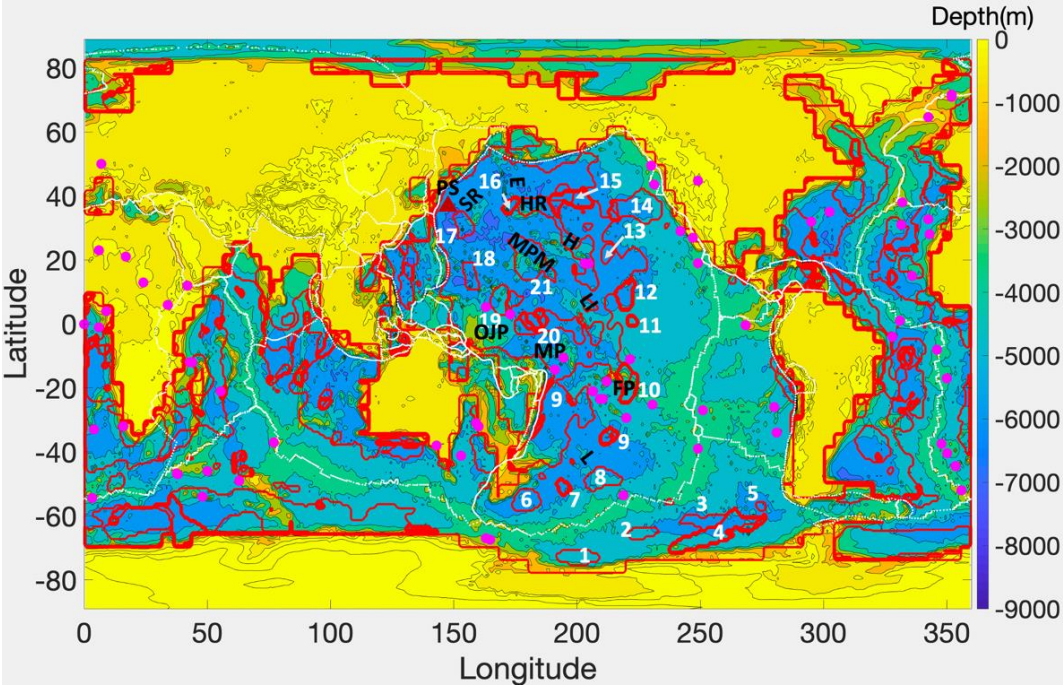


Figure 43 : Map showing the bathymetry and topography (data from Becker et al., 2009) and volcanic features (Ito and van Keken, 2007; King and Adam, 2014). The contours of lithospheric anomalies (denoted by 1 to 21) obtained from SEMUCB-WM1 (French and Romanowicz, 2014) are reported by the red lines. The white lines represent plate boundaries (Bird, 2003), such as mid-oceanic ridges and trenches. The magenta dots are the locations of hotspots (King and Adam, 2014). Acronyms for the volcanic features: PS – Petit Spot Volcanism (Machida et al., 2015), LI – Line Islands, L – Louisville, MP – Manihiki Plateau, OJP – Ontong Java Plateau, MPM - Mid-Pacific Mountains, H – Hawaii, HR – Hess Rise, E – Emperor and SR – Shatsky Rise

Figure 43 shows the bathymetry (data from Becker et al., 2009) and the names of the main volcanic features, such as oceanic plateaus and hotspots, on the Pacific plate (Ito and van Keken, 2007; King and Adam, 2014). The contours outlining the locations of lithospheric anomalies are reported in red. Some lithospheric anomalies are associated with oceanic plateaus and active hotspots. For example, feature 10 is located in French Polynesia, and is therefore associated with active volcanism. The feature 19 is associated with the Ontong Java Plateau. Feature 21 is associated with Mid-Pacific Mountains. Several features are adjacent to active hotspots, such as features 8, 10, 19 and 20. Feature 17 is adjacent to petit spot volcanism. However, most of the lithospheric instabilities are located in regions not associated

with active or old volcanism. There seems to be no clear correlation between the locations of lithosphere anomalies and volcanic features.

# Chapter 5 - Discussion

Secondary convection, or small-scale convection, is the convection that occurs at a smaller scale than the whole-mantle convection that drives plate tectonics. In the mantle, secondary convection is thought to take place at the base of the lithosphere, in the low-viscosity layer called the “asthenosphere” in geodynamic models. In theory, secondary convection would occur as sub-lithospheric longitudinal rolls, induced by the shear associated with the lithospheric plate motion, or as helices, formed when sinking cold plumes, falling from the base of the lithosphere are sheared away by the large-scale flow. There have been several numerical, analytical and experimental studies focusing on secondary convection and the induced lithosphere destabilization (Richter, 1973; Yuen and Fleitout, 1985; Korenaga and Jordan, 2003; Vidal, 2004). However, there are still open questions. For example, there is no consensus regarding the pattern of secondary convection, such as the wavelength, orientation, depth of occurrence, or the age of the lithospheric plate below which it occurs. Studying secondary convection from geophysical data and models could help constrain the characteristics of secondary convection. We have used tomography models, geoid anomalies, kinematic models and seafloor ages to provide evidence for small scale convection and to constrain the destabilization of lower portions of the Pacific lithospheric plate.

Global seismic tomography models provide a snapshot of the 3D structure of the Earth's mantle. This structure is provided in terms of lateral seismic velocity anomalies in percent (dvs%) for each point of the globe, i.e. for each longitude, latitude and depth (Figure 13). The seismic velocity anomalies (dvs%) are the departures from reference models, such as PREM (Dziewonski and Anderson, 1981), which provide the depth dependency of physical variables such as seismic velocities or density. We designed a Matlab code to automatically select particular points, such as the middle and the base of the lithosphere and asthenosphere, from the tomography models. The depth corresponding to the minimum dvs encountered along the profiles is selected as the

middle of the asthenosphere. The depth corresponding to the maximum dvs between depths 0 and the depth corresponding to the middle of the asthenosphere is selected as the middle of the lithosphere. The depth which corresponds to a change of slope of the dvs vs. depth profile, for depths greater than the middle of the asthenosphere is selected as the base of the asthenosphere. The base of the lithosphere is determined by selecting an isovalue of the seismic velocity anomaly.

We identified several anomalous regions, associated with thicker lithosphere when compared to surrounding regions (Figures 16, 22 and 24). We interpret these regions are lithospheric instabilities, or lithospheric drips. Some small wavelength circular anomalies are observed almost in the middle of the Pacific plate. If we connect these anomalies, we obtain a pattern that is perpendicular to the motion of the Pacific plate, and parallel to the mid-oceanic ridges. Farther north-west, longer elongated patterns, nearly parallel to the plate motion direction are observed. The lithospheric discontinuities are seen at depths we interpret as the middle (Figure 16) and base of the lithosphere (Figure 22).

The depth to the middle of the lithosphere (Figure 16) varies from about 35 km near the MOR to about 100 km far away from the MOR. A few regions are associated with anomalous depths of about 165 km to 250 km. The map of the base of the lithosphere (Figure 22) shows that the thickness of the lithosphere varies from 40km near the MOR to 180 km far from the MOR. The depth of middle of the asthenosphere (Figure 23) varies from about 100 km near the mid-oceanic ridges to about 450 km far from the mid-oceanic ridges. The anomalies observed in the map of the middle of the asthenosphere correlate well with the lithospheric anomalies discussed above (Figure 29). The base of the asthenosphere could not be recovered.

The lithosphere instabilities evidenced from the SEMUCB-WM1 tomography correlate relatively well with the lithosphere instabilities evidenced from the SAVANI tomography model, while considering the base of the lithosphere and the middle of the asthenosphere (Figures 31 and 32 respectively). This shows that the lithospheric instabilities are well recovered when new, highly resolved tomography models are considered. The correlation with the S40RTS tomography

model is less good (Figures 35 and 36). This is not surprising considering that the S40RTS tomography model is older and less well resolved.

We investigate the correlation between geoid anomalies and lithospheric instabilities, by filtering the EGM2008 geoid (Pavlis et al., 2012) for several order and degree ranges. We find that the lithospheric instabilities are correlated with negative geoid anomalies for degrees and orders 8-40 (Figure 38c). The correlation is probably created by mantle flow associated with the downwelling of the cold instabilities.

The correlation between lithospheric instabilities and geophysical data and models, such as plate kinematics, seafloor age, theoretical thickness of the lithosphere, the distance from the mid-oceanic ridges and bathymetric features has been studied. The lithospheric instabilities form an almost continuous anomalies in the middle of the Pacific plate, west of the mid-oceanic ridges (Figure 39). These anomalous features are perpendicular to the kinematic velocities (Figure 39). The longer discontinuous elongated patterns of lithospheric instabilities observed farther north-west are nearly parallel to the plate motion direction (Figure 39). The onset of lithospheric discontinuities is occurring on a seafloor with ages varying between 30 and 40 M.y. (Figure 40). The longer discontinuous lithospheric instabilities, nearly parallel to the plate motion, appear on 105 M.y. old seafloor (Figure 40). The onset of lithospheric instabilities occurs on lithosphere that is 75-90 km thick, according to the GDH1 thermal model (Figure 41). The longer lithospheric instabilities, parallel to the plate motion direction, appear on lithosphere that is 138 km thick (Figure 41). There is no clear correlation between the lithospheric instabilities and the distance from the mid-oceanic ridges (Figure 42). Although some lithospheric instabilities are associated with oceanic plateaus and active hotspots, such as Ontong Java, Mid-Pacific Mountains, or French Polynesia, there is no systematic correlation between lithospheric instabilities and volcanism (Figure 43). This demonstrates that the intraplate volcanism and the secondary convection are independent phenomena.

As stated before, there have been several analogical and numerical studies focusing on secondary convection occurring at the base of the lithosphere (Richter, 1973; Yuen and

Fleitout,1985; Korenaga and Jordan, 2003; Vidal, 2004). However, it is difficult to extrapolate the results of such studies to the real Earth. For example, there is ongoing debate about the critical age, i.e. the age where lithospheric instabilities would initiate.

The experimental study of the influence of the viscosity on the development of convective instabilities in a viscous fluid cooled from above by Jaupart and Parsons (1985) shows that small-scale instabilities develop only at the base of lithosphere older than 70 M.y. Davaille and Jaupart (1994) conducted laboratory experiments in temperature-dependent viscous fluids and suggest that small scale convective instabilities develop only after the lithosphere reaches ages of 40-65 M.y. Our results show that lithospheric destabilization initiated beneath seafloor that is 30-40 M.y. old, which is closer to the results of Davaille and Jaupart (1994). We find, however, that lithospheric instabilities can initiate on even younger lithosphere (~26 M.y.).

The morphology of lithospheric instabilities is also debated. Vidal (2004) studied experimentally the interaction between the shear flow and dripping convective instabilities that develop under a cold thermal boundary layer. Her results show that small-scale convection organizes mainly into two different morphologies, when sheared by the large-scale flow. For low Rayleigh number, or a low velocity ratio $V_{instability}/V_{shear}$, sub-lithospheric instabilities organize into Richter rolls (Figure 8), the axes of which align in the direction of plate motion. For higher Rayleigh numbers, or a high aspect ratio, instabilities take the shape of sinking cold plumes, falling from the base of the lithosphere and are then sheared away by the large-scale flow (Figure 10). Therefore, according to Vidal (2004), the key parameters that define the organization of small-scale convection features are 1) the velocity ratio ($V_{instability}/V_{shear}$) between two velocities, i.e. (i) velocity of the instability falling downwards and (ii) velocity of the horizontal shear flow; and 2) the Rayleigh number $Ra_{lat}$. Considering the Rayleigh number ($Ra_{lat}$) for the mantle of the Earth is $\sim 10^6$, the down falling instabilities will organize in the form of helical plumes sheared away by the large-scale flow if $V_{shear} < 10\ V_{instability}$ (Vidal, 2004). The different regimes of the structure of the small-scale convection patterns observed in the Vidal (2004) experiments are shown in the diagram in Figure 44.

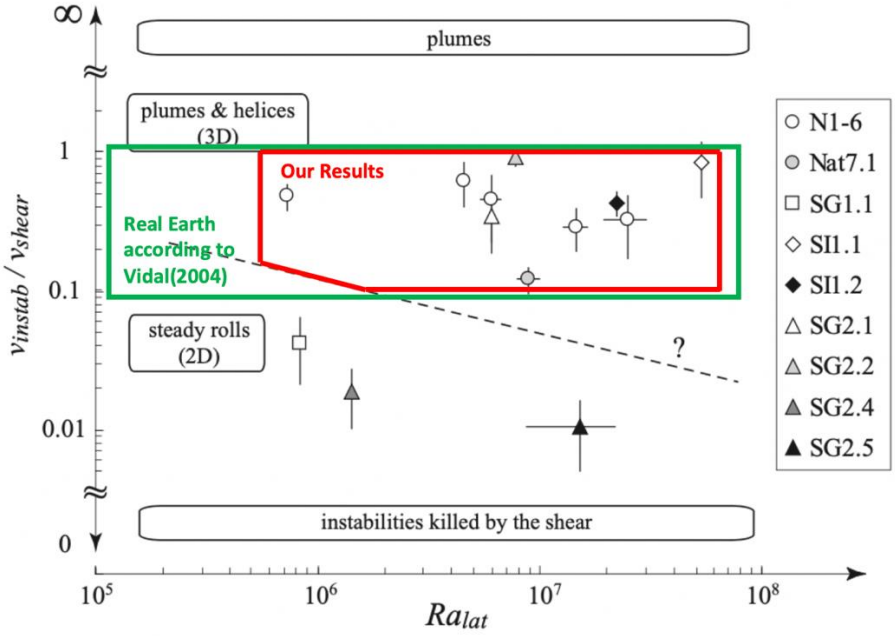


Figure 44 : Diagram showing the different regimes for different structures of small-scale convection patterns defined by the ratio ($V_{instability}/V_{shear}$) between two velocities, i.e. (i) velocity of the instability falling downwards and (ii) velocity of the horizontal shear flow; and the Rayleigh number $Ra_{lat}$. Different symbols represent the different experimental points. The zone inside the green box represents the regimes representative of "real Earth", defined by Vidal (2004). The zone inside the red box represents our result showing where the Pacific plate is situated in the 3D plumes and helices regime. Figure modified from Vidal (2004)

The lithospheric drips are clearly seen in Figure 24 profile AA', BB' and CC' (dashed magenta line and white continuous line). Our study provides new insights into secondary convection patterns inside the real Earth. Indeed, the pattern of lithospheric instabilities determined from the tomography show discontinuous elongated patterns, parallel to the Pacific plate motion (Figure 39). This implies that the secondary convection would occur as sinking cold plumes, falling from the base of the lithosphere and sheared away by the large-scale flow (Figure 10), as opposed to the Richter rolls (Figure 8).

Our results obtained for the Pacific plate confirm the prediction of the convective regimes obtained experimentally by Vidal (2004). Indeed, in Figure 44 the green box represents the regimes representative of "real Earth", defined by Vidal (2004), by examining which ranges of Rayleigh numbers and the $V_{instability}/V_{shear}$ ratios are representative of the "real Earth". The

extrapolation of laboratory experiments is generally difficult and associated with big uncertainties. Our results for the Pacific plate show that the secondary convection and the induced lithosphere destabilization occurs as “discontinuous rolls”, called “helices” by Vidal (2004) (see red box in Figure 44). Similar results are then found through two independent approaches: analogical studies and processing of geophysical data.

# Chapter 6 - Conclusion

The characteristics of secondary convection and the induced lithosphere destabilization have been constrained from the analysis of geophysical data and models, such as seismic tomography models and geoid anomalies. We determined the morphology of lithospheric discontinuities from tomography models. The lithospheric drips appear beneath seafloor that is 30-40 M.y. old but are organized as discontinuous elongated patterns parallel to the Pacific plate motion along a lithosphere that is at least 105 M.y. old. The thickness of the lithosphere along which the lithosphere destabilization initiates is 75-90 km. Longer discontinuous elongated patterns are observed on lithosphere of thickness greater than 138 km. These lithosphere instabilities are associated with negative geoid anomalies for order and degrees 8-40. The negative geoid anomalies are probably created by the downwelling flows associated with the lithosphere drips. There is no clear correlation between lithospheric destabilization and volcanism. Our results seem to indicate that in the real Earth, secondary convection appears as sinking cold plumes, falling from the base of the lithosphere and sheared away by large-scale flow (Figure 10), as opposed to Richter rolls (Figure 8). This confirms the regime diagram obtained experimentally by Vidal (2004).

# References


Adam, C., King, S., Vidal, V., Rabinowicz, M., Jalobeanu, A., and Yoshida, M. (2015), Variation of the subsidence parameters, effective thermal conductivity, and mantle dynamics, Earth and Planetary Science Letters, 426, 10.1016/j.epsl.2015.06.025

An, M., Wiens, D., Zhao, Y., Feng, m., Nyblade, A., Kanao, M., Li, Y., Maggi, A., and Lévêque, J. (2015), Temperature, lithosphere-asthenosphere boundary, and heat flux beneath the Antarctic Plate inferred from seismic velocities, Journal of Geophysical Research: Solid Earth, 120, 8720–8742, 10.1002/2015JB011917

Anderson, R. N., McKenzie, D. P., and Sclater, J. G. (1973), Gravity, bathymetry and convection within the earth Earth Planet. Sci. Lett., 18, 391–407

Auer, L., Boschi, L., Becker, T.W., Nissen-Meyer, T., and Giardini, D. (2014), Savani: A variable resolution whole-mantle model of anisotropic shear velocity variations based on multiple data sets. Journal of Geophysical Research: Solid Earth, 119, 3006– 3034, 10.1002/2013JB010773

Barletta, A. (2019), Rayleigh–Bénard Convection, 135-175, 10.1007/978-3-030-06194-4_7

Barry, T., Davies, J., Wolstencroft, M., Millar, I., Zhao, Z., Jian, P., Safonova, I., and Price, M. (2017), Whole-mantle convection with tectonic plates preserves long-term global patterns of upper mantle geochemistry, Scientific Reports, 7, 1870, 10.1038/s41598-017-01816-y

Becker, J.J., Sandwell D.T., Smith W.H.F., Braud J., Binder B., Depner J., Fabre D., Factor J., Ingalls S., Kim S.H., Ladner R., Marks K., Nelson S., Pharaoh A., Trimmer R., Von Rosenberg J., Wallace G., and Weatherall, P. (2009), Global bathymetry and elevation data at 30 arc seconds resolution: Srtm30_plus, Marine Geodesy, 32, 355–371, 10.1080/01490410903297766

Bénard, H. (1901), Les tourbillons cellulaires dans une nappe liquide propageant de la chaleur par convection en régime permanent thèse de doctorat, Gauthier–Villars, Paris

Bird, P. (2003), An updated digital model of plate boundaries, Geochem. Geophys. Geosyst, 4, 1027, 10.1029/2001GC000252

Bodine, J.H., Steckler, M.S., and Watts, A.B. (1981), Observations of flexure and the rheology of oceanic lithosphere, Journal of Geophysical Research, 86, 3695-3707, 10.1029/JB086iB05p03695

Condie, K.C. (2016), Earth as an Evolving Planetary System (Third Edition), 2016

Conrad, C. P., and Behn, M. D. (2010), Constraints on lithosphere net rotation and asthenospheric viscosity from global mantle flow models and seismic anisotropy, Geochemistry, Geophysics, Geosystems, 11, Q05W05, 10.1029/2009GC002970

Davaille, A., and Jaupart, C. (1994), Onset of thermal convection in fluids with temperature-dependent viscosity: application to the oceanic mantle, J. Geophys. Res., 99 (B10), 19853-19866, 10.1029/94JB01405

Dumoulin, C., Doin, M.P., and Fleitout, L. (2001), Numerical simulation of the cooling of an oceanic lithosphere above a convective mantle, Phys. Earth Planet Int., 125, 45-64

Dzeiwonski, A.M., and Anderson, D. L. (1981), Preliminary Reference Earth Model, Phys. Earth planet Inter., 25, 297-356

French, S. W., Lekic, V., and Romanowicz, B. (2013), Waveform tomography reveals channeled flow at the base of the oceanic asthenosphere, Science, 342, 227–230, 10.1126/science.1241514

French S. W., and Romanowicz, B.A. (2014), Whole-mantle radially anisotropic shear velocity structure from spectral-element waveform tomography, Geophysical Journal International, 199(3), 1303–1327, 10.1093/gji/ggu334

Gripp, A., and Gordon, R. G. (2002), Young tracks of hotspots and current plate velocities, Geophysical Journal International, 150, 10.1046/j.1365-246X.2002.01627.x

Hager, B.H., and Clayton, R.W. (1989), Constraints on the structure of mantle convection using seismic observations, flow models, and the geoid, Mantle Convection: Plate Tectonics and Global Dynamics, (ed. Peltier W.R., Gordon and Breach, New York), 657–763

Hager, B.H., and Richards, M.A. (1989), Long-wavelength variations in Earth's geoid: physical models and dynamical implications, Philos. Trans. R. Soc., London, A 328, 309–327, 10.1098/rsta.1989.0038

Haxby, W. F., and Weissel, J. K. (1986), Evidence for small-scale mantle convection from SEASAT Altimeter data, Journal of Geophysical Research, 91(B3), 3507– 3520, 10.1029/JB091iB03p03507

Hofmeister, A., and Criss, R. (2005), Heatflow and mantle convection in the triaxial Earth, 388, 289-302, 10.1130/0-8137-2388-4.289

Howard, L. N. (1966), Convection at high Rayleigh numbers, In Proc. 11th Int. Congr. Appl. Mech. Munich, 1964 (ed. H. Görtler), p. 1109.Springer

Ito, G., and Vankeken, P. (2007), Hot Spots and Melting Anomalies, Mantle Dynamics, 7, 371-435, 10.1016/B978-044452748-6/00123-1

Jaupart, C., and Parsons, B. (1985), Convective instabilities in a variable viscosity fluid cooled from above, Phys. Earth Planet. Inter., 39, 14-32, 10.1016/0031-9201(85)90112-8

Key, K., Constable, S., Liu, L., and Pommier, A. (2013), Electrical image of passive mantle upwelling beneath the northern East Pacific Rise, Nature, 495, 499-502, 10.1038/nature11932

King, S.D., and Adam, C. (2014), Hotspots swells revisitied, Phys. Earth Planet. Inter., 235, 66-83, 10.1016/j.pepi.2014.07.006

Korenaga, J. & Jordan, T. (2003), Linear stability analysis of Richter rolls, Geophysical Research Letters, 30, 10.1029/2003GL018337

Machida, S., Hirano, N., Sumino, H., Hirata, T., Yoneda, S., Kato, Y. (2015), Petit-spot geology reveals melts in upper-most asthenosphere dragged by lithosphere, Earth and Planetary Science Letters, 426, 267-279, 10.1016/j.epsl.2015.06.018

Morgan, W.J. (1971), Convection plumes in the lower mantle, Nature, 230, 42-43, 10.1038/230042a0

Müller, R. D., Roest, W. R., Royer, J.-Y., Gahagan, L. M., and Sclater, J. G. (1997), Digital isochrons of the world's ocean floor, J. Geophys. Res., 102, 3211– 3214, 10.1029/96JB01781

Pavlis, N.K., Holmes, S.A., Kenyon, S.C. and Factor, J.K. (2012), The development and evaluation of the Earth Gravitational Model 2008 (EGM2008), J. Geophys. Res., 117, 10.1029/2011JB008916

Rayleigh, L. (1916), On convection currents in a horizontal layer of fluid, when the higher temperature is on the underside, London Edinb. Dubl., Phil. Mag. J. Sci., 32, 529–546

Richter, F.M. (1973), Convection and the large-scale circulation of the mantle, J. Geophys. Res., 78 (35), 8735– 8745

Richter, F. M., and Parsons, B. (1975), On the interaction of two scales of convection in the mantle, J. Geophys. Res., 80, 2529– 2541

Ritsema, J., Deuss, A., Heijst, H.J., Woodhouse, J.H. (2011), S40RTS: a degree-40 shear-velocity model for the mantle from new Rayleigh wave dispersion, tele- seismic traveltime and normal-mode splitting function measurements, Geophysical Journal International, 184, 1223-1236, 10.1111/j.1365-246X.2010.04884.x

Schubert, G., Turcotte, D.L., and Olson, P. (2001), Mantle Convection in the Earth and Planets, Cambridge: Cambridge University Press, 10.1017/CB09780511612879

Sleep, N. (2008), Channeling at the base of the lithosphere during the lateral flow of plume material beneath flow line hot spots, Geochemistry Geophysics Geosystems, 9, 10.1029/2008GC002090

Spiegelman, M., and McKenzie, D. P. (1987), Simple 2-D models for melt extraction at mid-ocean ridges and island arcs, Earth Planet. Sci. Lett., 83, 137– 152, 10.1016/0012-821X(87)90057-4

Stein, C. A., and Stein, S. (1992), A model for the global variation in oceanic depth and heat flow with lithospheric age, Nature, 359, 123–129, 10.1038/359123a0

Turcotte, D.L., and Schubert, G. (2002), Geodynamics, 2nd edition, Cambridge Univ. Press

Vidal, V. (2004), Interaction des differentes´ echelles de convection dans le manteau terrestre (Thèse de doctorat de l'Institut de Physique du Globe de Paris)

Weatherley, S. M., and Katz, R. F. (2010), Plate-driven mantle dynamics and global patterns of mid-ocean ridge bathymetry, Geochemistry, Geophysics, Geosystems, 11 (10), 10.1029/2010GC003192

Wen, L., and Anderson, D.L. (1997), Layered mantle convection: a model for geoid and topography, Earth Planet. Sci. Lett., 146, 367-377, 10.1016/S0012-821X(96)00238-5

Yuen, D.A., and Fleitout L. (1985), Thinning of the lithosphere by small-scale convective destabilization, Nature, 313, 125-128, 10.1038/313125a0

Ziegler, P.A. (1993), Plate-moving mechanisms: their relative importance: William Smith Lecture 1992, Journal of The Geological Society, 150, 927-940, 10.1144/gsjgs.150.5.0927

# Appendix A

# Determination of the Base of the Lithosphere from SAVANI and S40RTS tomography models

## Determination of the base of the lithosphere from the SAVANI tomography model (Auer et al., 2014)

The maps showing the base of the lithosphere obtained with dvs=1%, dvs=1.5% and dvs=2% are displayed in Figure 45 a, b and c respectively. They have been obtained by considering the seismic velocity anomalies, dvs, provided by the SAVANI (Auer et al., 2014), and the approach previously described in section 3, 'Methods'.

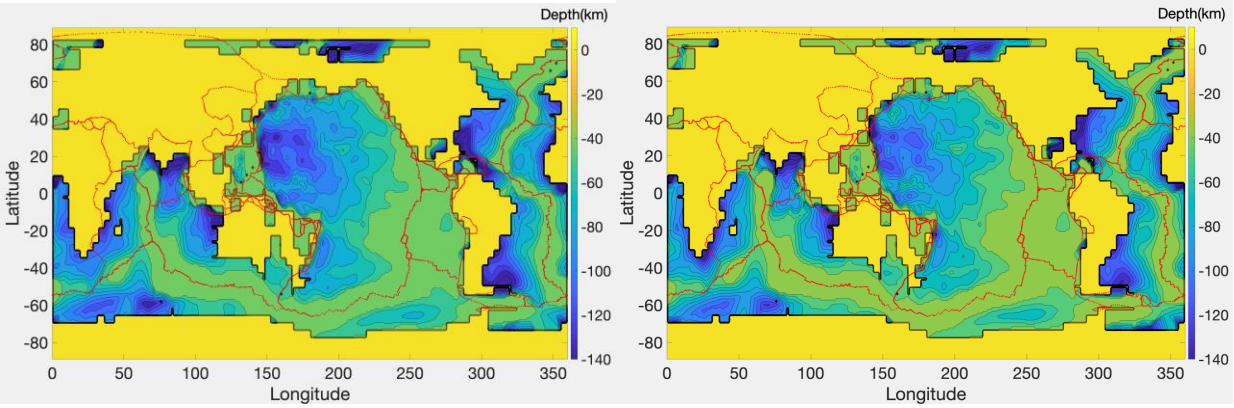


(a) (b)

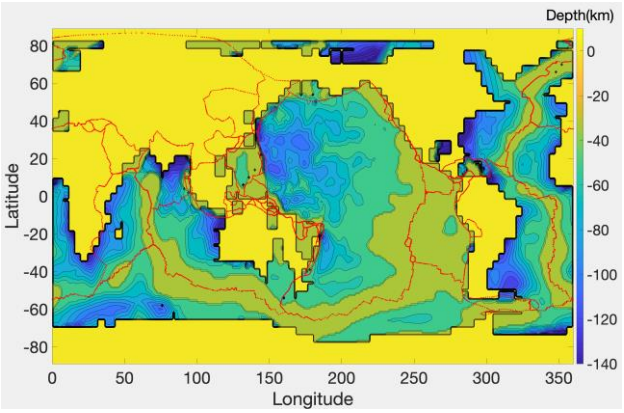


(c)

Figure 45 : Map of the base of the lithosphere based on SAVANI tomography model (Auer et al., 2014). The base of the lithosphere is by different isovalues. a) dvs=1%; b) dvs=1.5% c) dvs=2%. The red lines represent plate boundaries (Bird, 2003), such as mid-oceanic ridges and trenches

The depths to the dvs = 1%, 1.5% and 2% isovalues show very similar patterns (Figure 45). Figure 46 shows the map obtained by plotting the depth to the base of the lithosphere determined with dvs=2% minus the depth to the base of the lithosphere determined by dvs=1%.

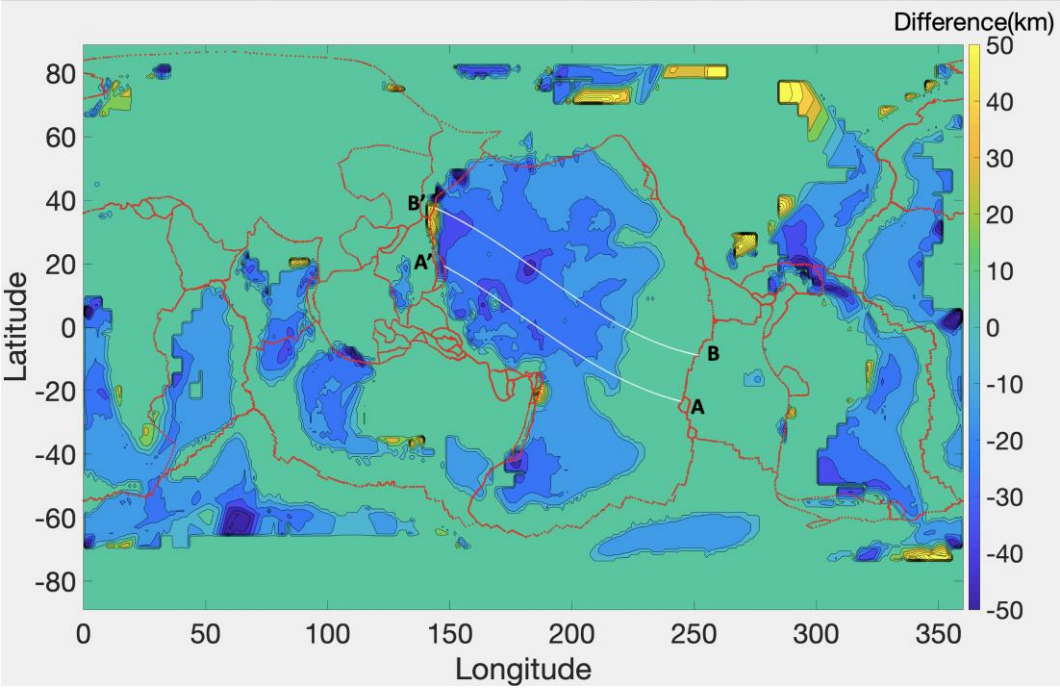


Figure 46 : Map of the difference in the depth to the base of the lithosphere determined with dvs=2% and the depth to the base of the lithosphere determined by dvs =1%, based on the SAVANI tomography model (Auer et al., 2014). The red lines represent plate boundaries (Bird, 2003), such as mid-oceanic ridges and trenches. The white lines (AA' and BB') are trajectories representative of the present-day plate motion (taken from Adam et al., 2015) along which the depth cross sections are investigated

The difference between these two models ranges between +50 and -50 km, but it varies mainly between 0 and 20 km except in a few regions like around longitude 155°E and latitude 30°N, longitude 175°E and latitude 10°N and around longitude 190°E and latitude 20°N where it is about -30 to -50 km.

Figure 47 represents the uncertainty in percentage, obtained from the data displayed in Figure 46, by dividing the difference in depths (between the dvs=2% and dvs=2% isosurfaces) by the mean value of the depths determined by the three isovalues dvs=1%, 1.5% and 2%.

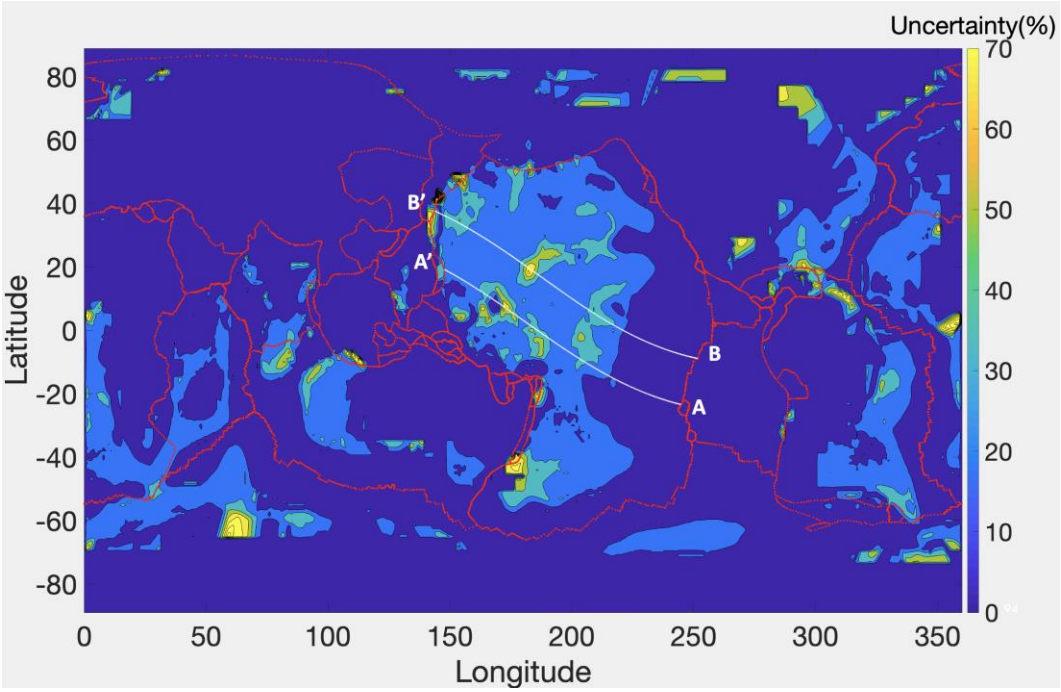


Figure 47 : Map of the uncertainty in percentage obtained from the data displayed in Figure 46, by dividing the difference in the depths ( between the dvs=2% and dvs=1% isosurfaces) by the mean value of the depths determined by the three isovalues dvs=1%, 1.5% and 2%. These results have been obtained with the SAVANI tomography model (Auer et al., 2014). The red lines represent plate boundaries (Bird, 2003), such as mid-oceanic ridges and trenches. The white lines (AA' and BB') are trajectories representative of the present-day plate motion (taken from Adam et al., 2015) along which the depth cross sections are investigated

The uncertainty represented in Figure 47 varies from 0 to 70%. Most regions are associated with a 0-20% uncertainty. Larger uncertainties, reaching sometimes 70% are found locally, around longitude 170°E and latitude 5°N for example, or at longitude 180°E and latitude 20°N.

The yellow regions in Figure 48 represent areas where the uncertainty in percentage, displayed in Figure 47, is greater than 30%. The blue regions represent areas where the uncertainty is less than or equal to 30%. Most of the regions in the Pacific Ocean are associated with an uncertainty smaller than 30%.

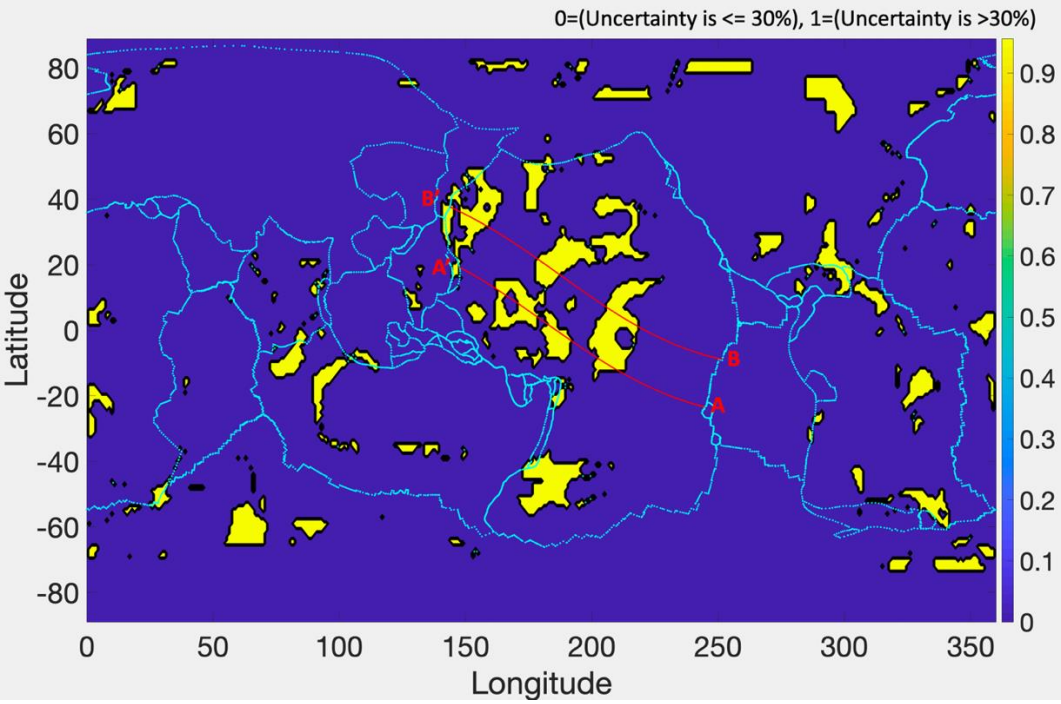


Figure 48 : Map of the regions where the uncertainty in percentage displayed in Figure 47 is greater than 30%, in yellow, and less than or equal to 30%, in blue. These results have been obtained with the SAVANI tomography model (Auer et al., 2014). The cyan lines represent plate boundaries (Bird, 2003), such as mid-oceanic ridges and trenches. The red lines (AA' and BB') are trajectories representative of the present-day plate motion (taken from Adam et al., 2015) along which the depth cross sections are investigated

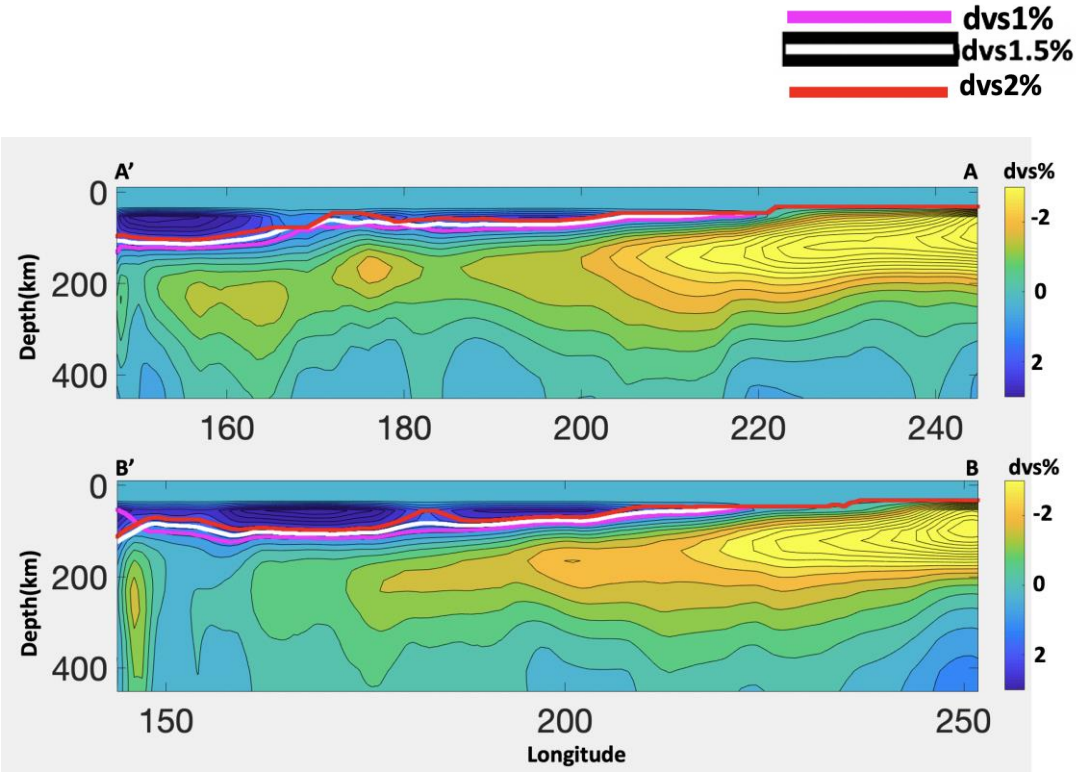


Figure 49 : Depth cross section along the trajectories represented in the Figure 46, 47 and 48 for tomography model SAVANI (Auer et al., 2014). The magenta, white and red lines represent the base of lithosphere determined by dvs=1%, 1.5% and 2%, respectively

Figure 49 shows depth cross sections along the profiles AA' and BB' represented in Figures 46 47 and 48. We can see that the depths represented by three lines give similar results in most of the regions. Local departures are observed around longitude 170$^{o}$E in AA' profile, or at longitude 180$^{o}$E in BB' profile. Our final determination of the base of the lithosphere uses the depth computed with dvs=1.5% (chosen arbitrarily), when the uncertainty displayed in Figure 47 is smaller than 30 % (regions displayed in blue in Figure 48). For regions where this uncertainty is bigger than 30 % (regions displayed in yellow in Figure 48), the mean of the depths computed with the three values (dvs1%, dvs1.5% and dvs2%) is imposed. The final map is displayed in Figure 50. It is representative of the base of the lithosphere obtained for SAVANI tomography model (Auer et al., 2014), and will be discussed in the main text.

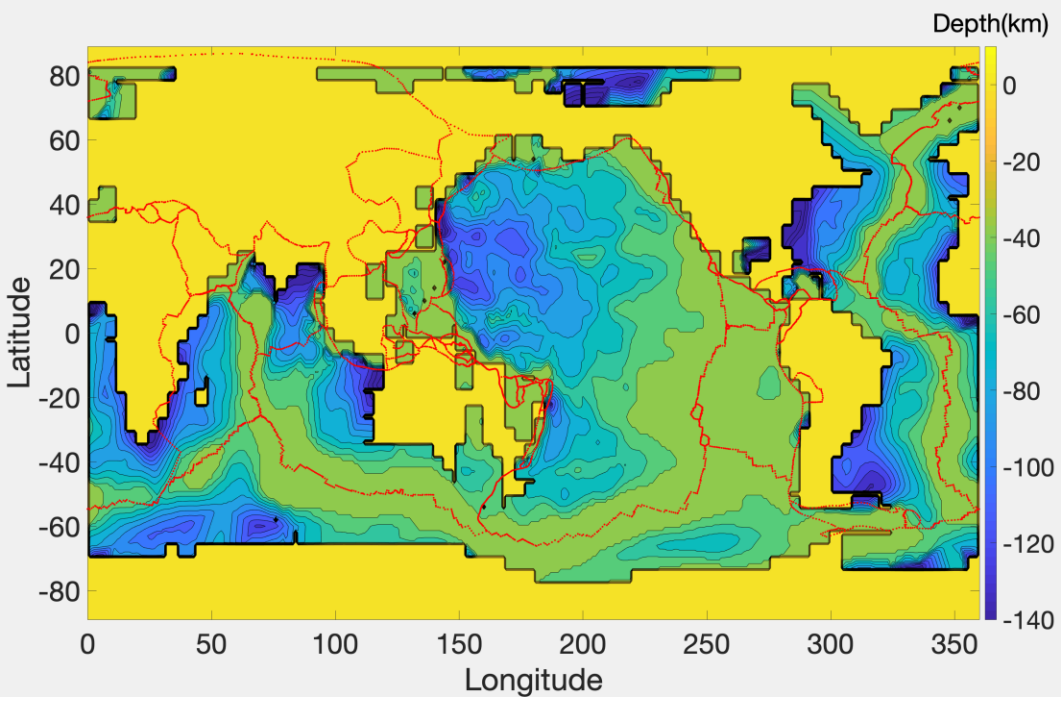


Figure 50 : Map of the base of the lithosphere based on SAVANI tomography model (Auer et al., 2014) obtained by considering the depths to the dvs=1.5% isosurface when the uncertainty (Figure 47) is less than 30% (regions displayed in blue in Figure 48). When the uncertainty is greater than 30%, we impose the mean values of the depths determined by the dvs=2%, dvs=1.5% and dvs=1% isovalues. The red lines represent plate boundaries (Bird, 2003), such as mid-oceanic ridges and trenches

## Determination of the base of the lithosphere from the S40RTS tomography model (Ritsema et al., 2011)

The maps showing the base of the lithosphere obtained with dvs=1%, dvs=1.5% and dvs=2% are displayed in Figure 51 a, b and c respectively. They have been obtained by considering the seismic velocity anomalies, dvs, provided by the S40RTS tomography model (Ritsema et al., 2011) and the approach previously described in section 3, 'Methods'.

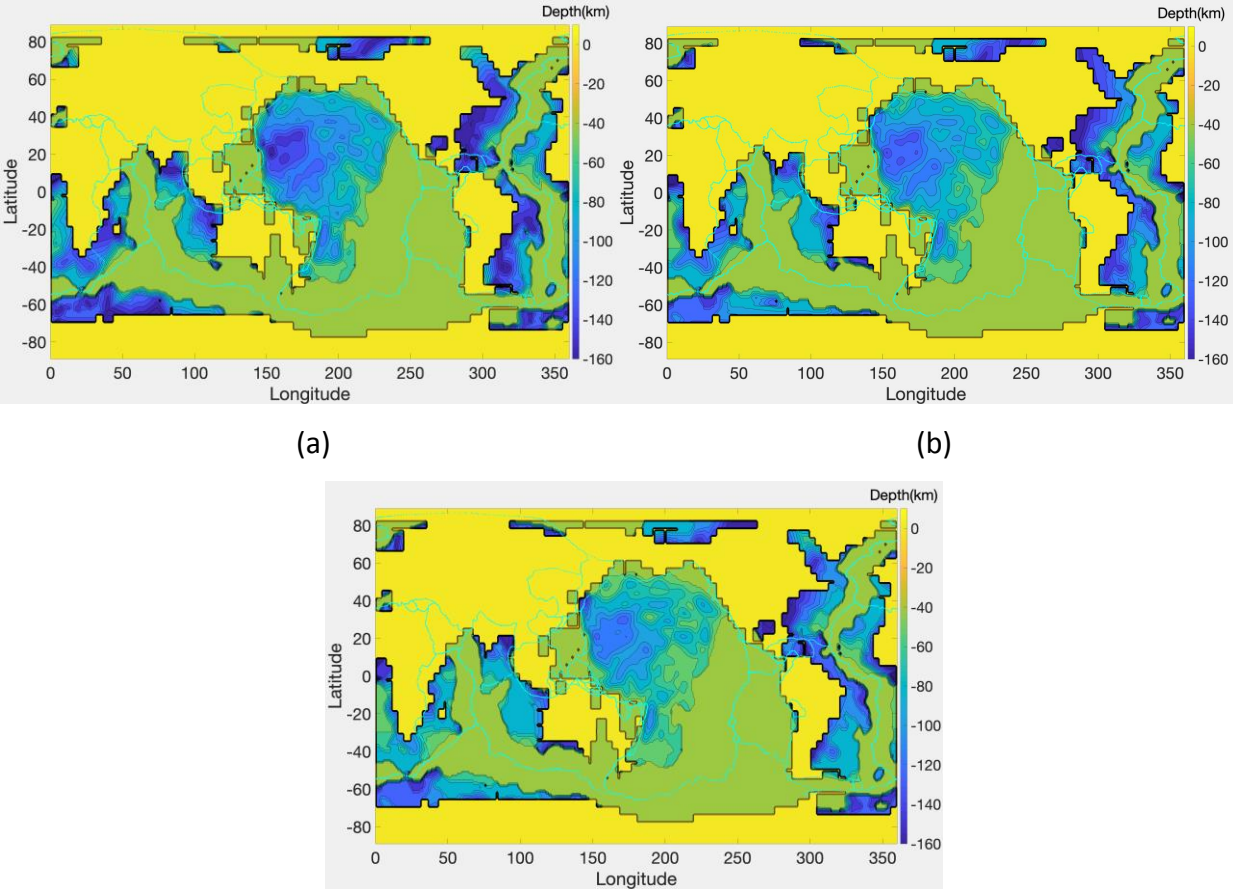


Figure 51 : Map of the base of the lithosphere based on S40RTS tomography model (Ritsema et al., 2011). The base of the lithosphere is by different isovalues. a) dvs=1%; b) dvs=1.5% c) dvs=2%. The cyan lines represent plate boundaries (Bird, 2003), such as mid-oceanic ridges and trenches

The depths to the dvs = 1%, 1.5% and 2% isovalues show very similar patterns (Figure 51). Figure 52 shows the map obtained by plotting the depth to the base of the lithosphere determined with dvs=2% minus the depth to the base of the lithosphere determined by dvs=1%.

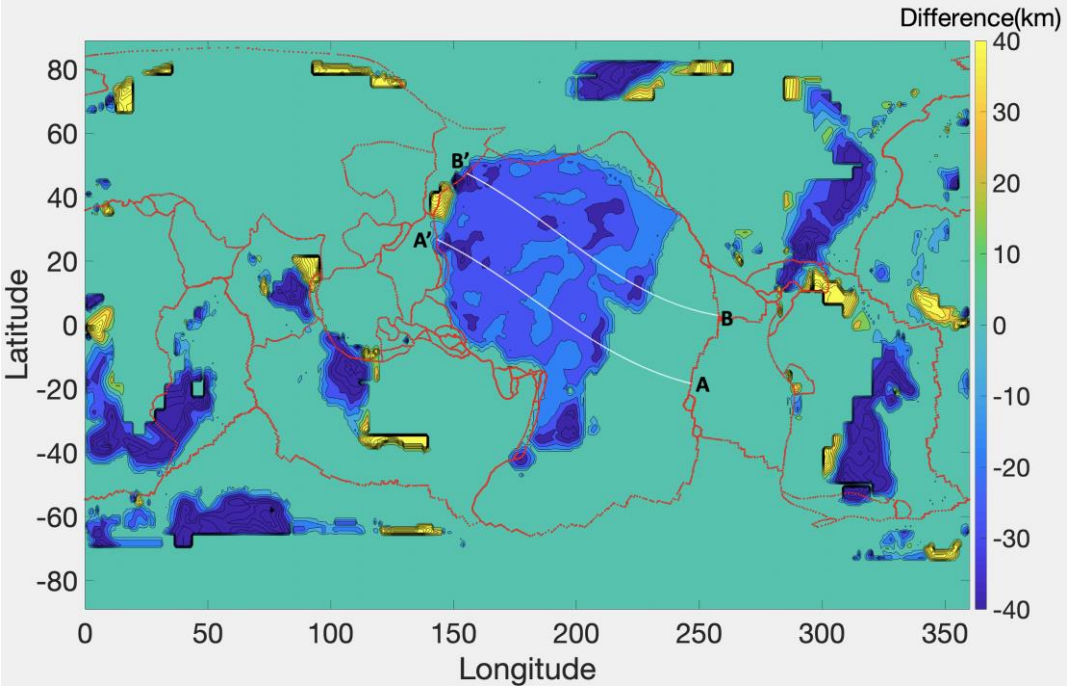


Figure 52 : Map of the difference in the depth to the base of the lithosphere determined with dvs=2% and the depth to the base of the lithosphere determined by dvs =1%, based on the S40RTS tomography model (Ritsema et al., 2011). The red lines represent plate boundaries (Bird, 2003), such as mid-oceanic ridges and trenches. The white lines (AA' and BB') are trajectories representative of the present-day plate motion (taken from Adam et al., 2015) along which the depth cross sections are investigated

The difference between these two models ranges between +40 and -40 km, but it varies mainly between 0 and -20 km, except in a few regions like around longitude 155°E and latitude 20°N, or at longitude 190°E and latitude 35°N, where it is about -40 km.

Figure 53 represents the uncertainty in percentage obtained from the data displayed in Figure 52 by dividing the difference in depths (between the dvs=2% and dvs=1% isosurfaces) by the mean value of the depths determined by the three isovalues dvs=1%, 1.5% and 2%.

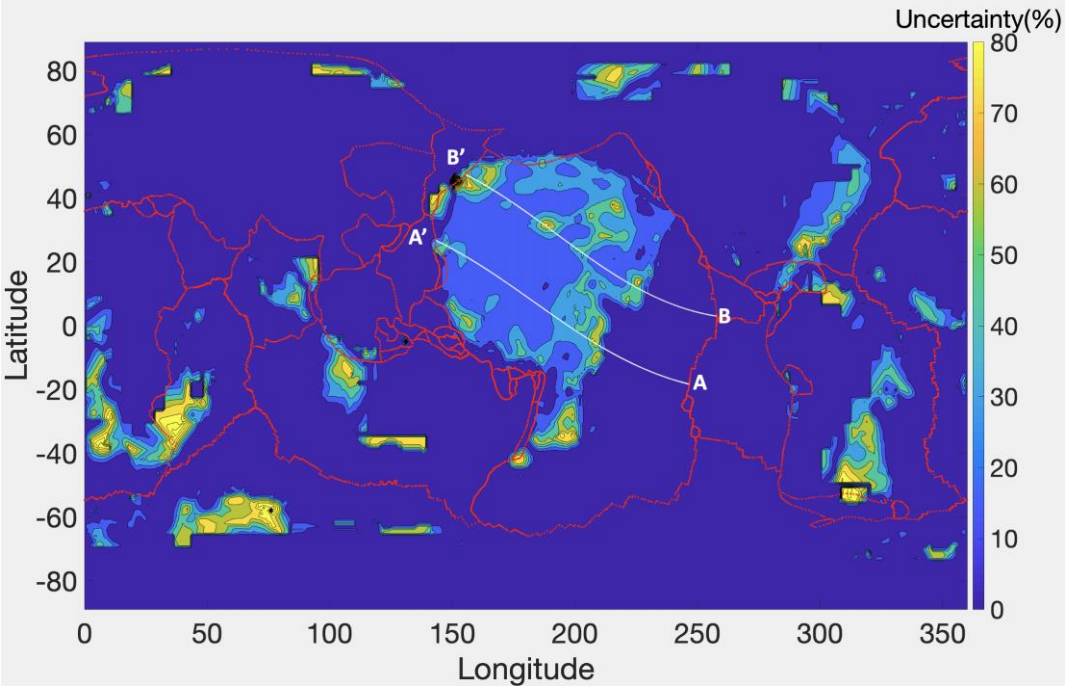


Figure 53 : Map of the uncertainty in percentage obtained from the data displayed in Figure 52, by dividing the difference in the depths ( between the dvs=2% and dvs=1% isosurfaces) by the mean value of the depths determined by the three isovalues dvs=1%, 1.5% and 2%. These results have been obtained with the S40RTS tomography model (Ritsema et al., 2011). The red lines represent plate boundaries (Bird, 2003), such as mid-oceanic ridges and trenches. The white lines (AA' and BB') are trajectories representative of the present-day plate motion (taken from Adam et al., 2015) along which the depth cross sections are investigated

The uncertainty represented in Figure 53 varies from 0 to 80%. Most regions are associated with a 0-20% uncertainty. Larger uncertainties, reaching sometimes 80% are found locally, around longitude 155°E and latitude 20°N for example, or at longitude 190°E and latitude 35°N.

The yellow regions in Figure 54 represent areas where the uncertainty in percentage, displayed in Figure 53, is greater than 30%. The blue regions represent areas where the uncertainty is less than or equal to 30%. Most of the regions in the Pacific Ocean are associated with an uncertainty smaller than 30%.

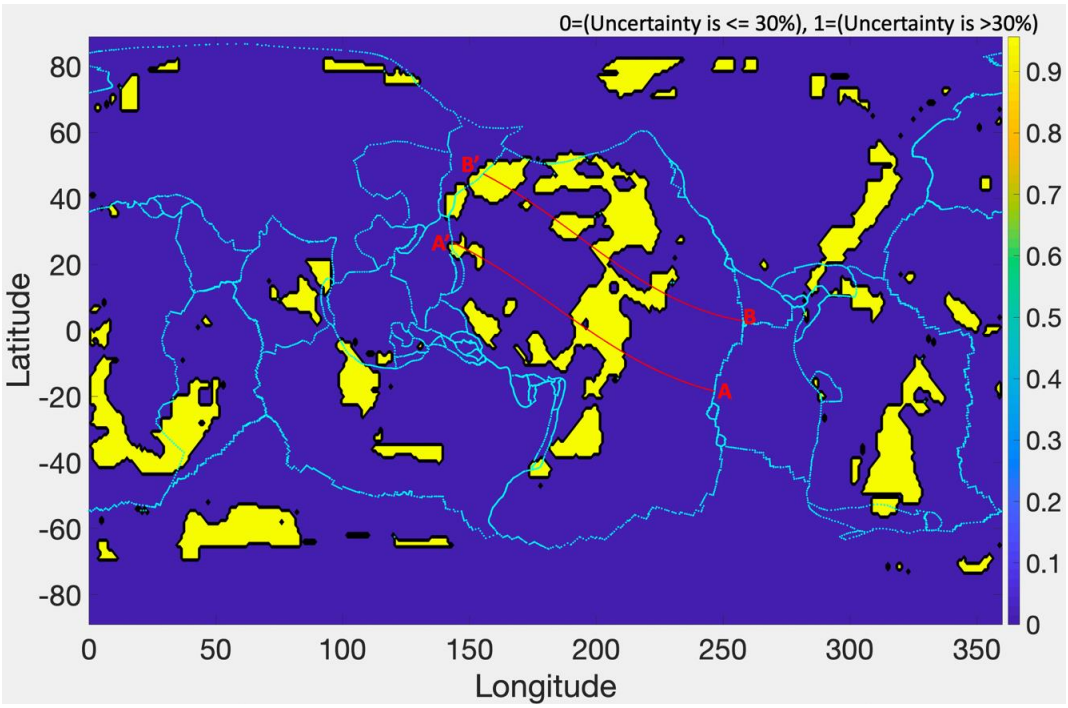


Figure 54 : Map of the regions where the uncertainty in percentage displayed in Figure 53 is greater than 30%, in yellow, and less than or equal to 30%, in blue. These results have been obtained with the S40RTS tomography model (Ritsema et al., 2011). The cyan lines represent plate boundaries (Bird, 2003), such as mid-oceanic ridges and trenches. The red lines (AA' and BB') are trajectories representative of the present-day plate motion (taken from Adam et al., 2015) along which the depth cross sections are investigated

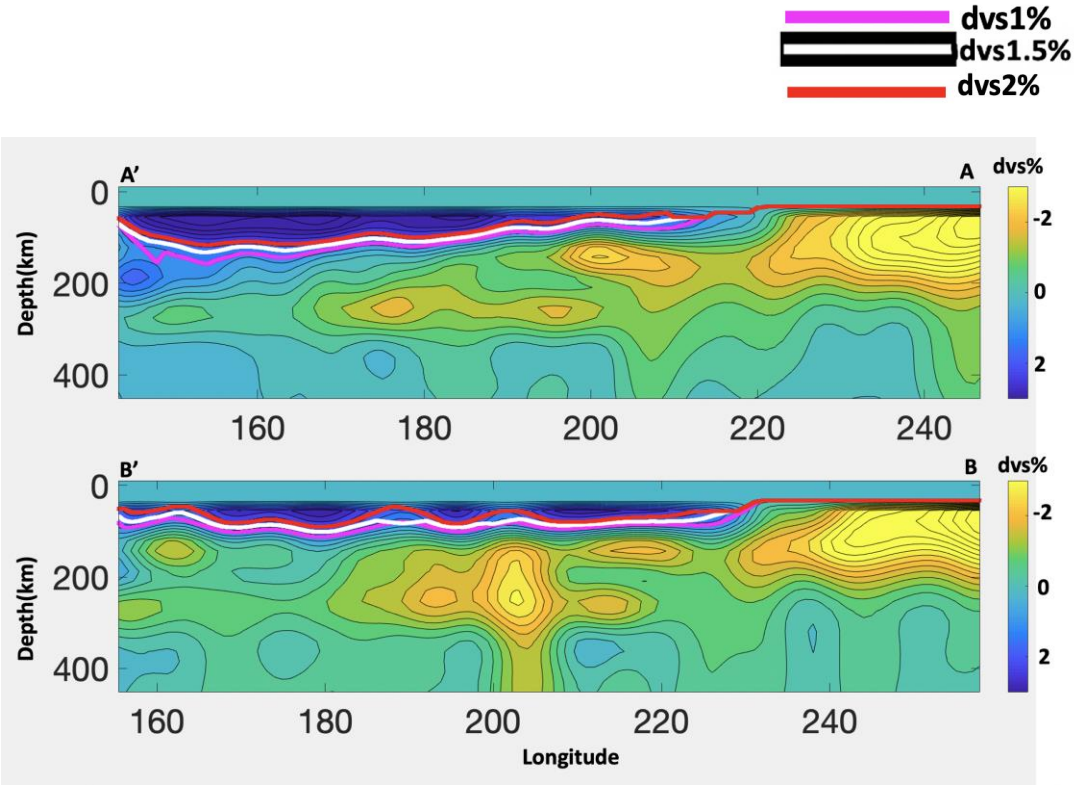


Figure 55 : Depth cross section along the trajectories represented in the Figure 52, 53 and 54 for S40RTS tomography model (Ritsema et al., 2011). The magenta, white and red lines represent the base of lithosphere determined by dvs=1%, 1.5% and 2%, respectively

Figure 55 shows depth cross sections along the profiles AA' and BB' represented in Figure 52, 53 and 54. We can see that the depths represented by three lines give similar results in most of the regions. Local departures are observed around longitude 155°E in AA' profile, or at longitude 190°E in BB' profile. Our final determination of the base of the lithosphere uses the depth computed with dvs=1.5% (chosen arbitrarily), when the uncertainty displayed in Figure 53 is smaller than 30% (regions displayed in blue in Figure 54). For regions where this uncertainty is bigger than 30% (regions displayed in yellow in Figure 54), the mean of the depths computed with the three values (dvs1%, dvs1.5% and dvs2%) is imposed. The final map is displayed in Figure 56. It is representative of the base of the lithosphere obtained for S40RTS tomography model (Ritsema et al., 2011), and will be discussed in the main text.

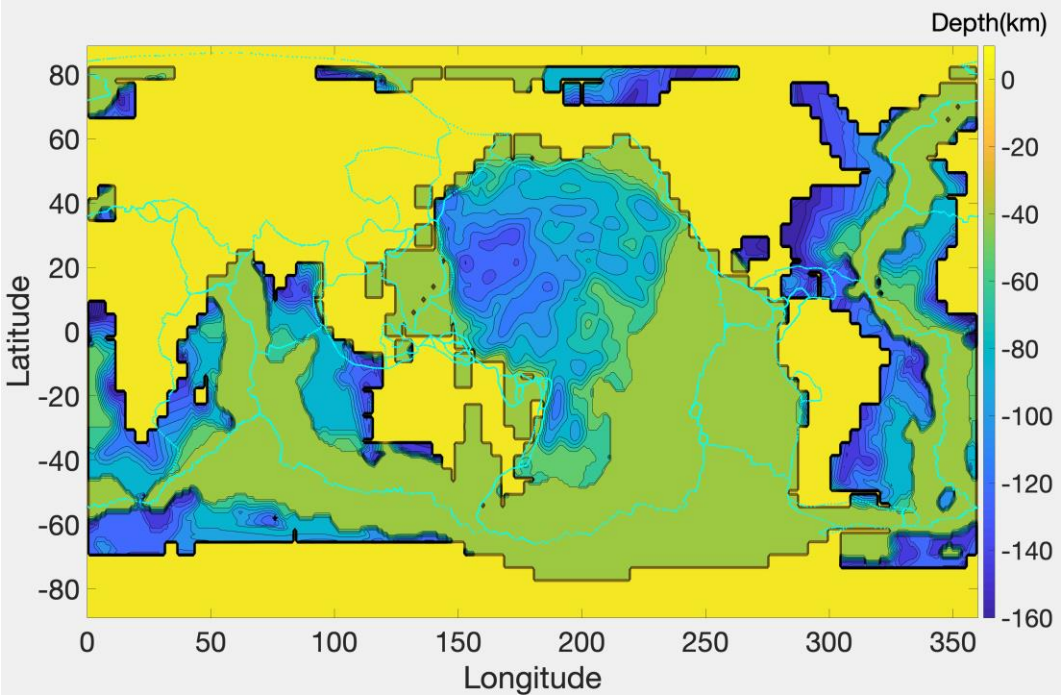


Figure 56 : Map of the base of the lithosphere based on S40RTS tomography model (Ritsema et al., 2011) obtained by considering the depths to the dvs=1.5% isosurface when the uncertainty (Figure 53) is less than 30% (regions displayed in blue in Figure 54). When the uncertainty is greater than 30%, we impose the mean values of the depths determined by the dvs=2%, dvs=1.5% and dvs=1% isovalues. The cyan lines represent plate boundaries (Bird, 2003), such as mid-oceanic ridges and trenches